UNIVERSIDADE FEDERAL DE PERNAMBUCO
CENTRO DE CIÊNCIAS EXATAS E DA NATUREZA
DEPARTAMENTO DE FÍSICA
PROGRAMA DE PÓS-GRADUAÇÃO EM FÍSICA

HELENA CHRISTINA PIUVEZAM DE ALBUQUERQUE BASTOS

Unconventional Criticality in The Stochastic Wilson-Cowan Model

Recife

2023

HELENA CHRISTINA PIUVEZAM DE ALBUQUERQUE BASTOS

Unconventional Criticality in The Stochastic Wilson-Cowan Model

Tese apresentada ao Programa de PósGraduação em Física da Universidade Federal de Pernambuco, como requisito parcial para obtenção do título de doutora em Física.

Área de Concentração: Dinâmica Não-linear, Caos e Sistemas Complexos

Orientador: Mauro Copelli Lopes da Silva

Recife

2023

Catalogação na fonte
Bibliotecária Nataly Soares Leite Moro, CRB4-1722

B327u Bastos, Helena Christina Piuvezam de Albuquerque
Unconventional criticality in the stochastic Wilson-Cowan model / Helena Christina Piuvezam de Albuquerque Bastos. – 2023.
116 f.: il., fig., tab.

Orientador: Mauro Copelli Lopes da Silva.
Tese (Doutorado) – Universidade Federal de Pernambuco. CCEN, Física, Recife, 2023.
Inclui referências e apêndices.

1. Física teórica e computacional. 2. Modelo de Wilson-Cowan. 3. Avalanches neuronais. I. Silva, Mauro Copelli Lopes da (orientador). II. Título.

530.1 CDD (23. ed.) UFPE- CCEN 2024 - 26

Helena Christina Piuvezam de Albuquerque Bastos

Unconventional Criticality in The Stochastic Wilson-Cowan Model

Tese apresentada ao Programa de Pós-Graduação em Física da Universidade Federal de Pernambuco, como requisito parcial para a obtenção do título de Doutora em Física.

Aprovada em: 15/12/2023.

BANCA EXAMINADORA

_____

Prof. Dr. Mauro Copelli Lopes da Silva
Orientador
Universidade Federal de Pernambuco

_____

Prof. Dr. Ernesto Carneiro Pessoa Raposo
Examinador Interno
Universidade Federal de Pernambuco

_____

Prof. Dr. Paulo Roberto de Araujo Campos
Examinador Interno
Universidade Federal de Pernambuco

_____

Prof. Dr. Ronald Dickman
Examinador Externo
Universidade Federal de Minas Gerais

_____

Prof. Dr. Silvio da Costa Ferreira Junior
Examinador Externo
Universidade Federal de Viçosa

ACKNOWLEDGEMENTS

First of all, I would like to thank my advisor Mauro Copelli, who has been the force behind this work. I have learned a great deal from him. His zest for teaching – which not only he seems to have a natural talent for but is very passionate about – and his very precise writing style are truly inspiring. I would also like to give special thanks to our main contributors: Miguel A. Muñoz, who was decisive in understanding all the new phenomena presented here, was wonderful as an advisor and person during my stay at Granada and from whom I was able to perceive a different type of teaching and lab conducting; And, Boris Marin, who not only helped us since the beginning of this project but also was very supportive and available, pushing me to learn beyond what I was presently doing and all the theories around it.

These years would not have been possible without the financial support of Capes and CnPQ. Specifically Capes with my regular sponsorship and PrInT grant 88887.581360/2020-00.

My biggest emotional support was my family. In particular, my mom and dad have stood by me throughout the long process, since long before I wanted to graduate in Physics. My mom would not let me give up at any step of the way and my dad made it so I would not by telling me that I could if I wanted to. My sister has also been a great supporter through all this, she always got me to try harder by always being proud of every little step I took, thank you all.

I would also like to thank my best friend, Joel, who is not in academia and did not contribute with knowledge. He is also very far away so he was not physically beside me through it all. However, he gave me more support than I could ever ask for by listening to me talking about academic and non-academic problems, being always present (through messages) whenever I needed to vent, and just keeping me sane. In the same category is Lindembergue, who is a person that I would trust my life to, he has always been there through thick and thin, thank you very much. My friends Jessica, Juliana, and Thatyane for always being there for me since we were kids, you guys always pick me up when I'm down.

To the people in the Lab at UFPE, I hope I do not forget anyone, but in general, I want to acknowledge them all, the ones at the Department and the ones at the LFTC. The first I want to acknowledge is Jheniffer, you have been an incredible friend, apart from having learned a lot from you I also got to spend happy times with you, so thank you for it all. Nathan, I'm sorry I forced you into friendship, but thank you for giving me some of it. Leandro, for being

the bundle of joy that you are. Tawan, for being a great help a lot of times and giving the best hugs ever. Felipe, thank you for waiting a couple of minutes to have lunch with me, and I'm sorry. Thais, thank you for being so kind and helpful. I would also like to thank Daniel, Italo, Pedro, and Nivaldo for everything: rich talks, help with problems, and overall just plain support.

To the people in Granada, it is really hard to be a foreigner, and if you do not fully speak the language to boot. However, it did not feel like I was out of the country, you made me feel at home, so thank you very much. Paloma, for caring for me, taking me out of the apartment whenever I was not working, and truly being a friend. Adri, for listening to me every morning and helping me figure out the problems I would face with my calculations and my life at times. Alvaro, for getting me to speak some Spanish and getting me to appreciate Spain. Jorge, for being a little Spanish angel (sorry I was ridiculous not letting you have lunch at times) and helping me through so much. Mateo, for the very weird conversations we would get to. Roberto, for being there whenever I needed a hug, understanding the chaos that was in my head sometimes, and working through this crazy model's shenanigans. Ruben, for understanding, when just a little wasn't that at all, for having very interesting talks where I feel like I learned so much, and for also taking me out of the apartment when I needed to take some air.

A special thank you to the people who kept me healthy, Debora Soares and Dr. Rafaela Gonçalves.

Last but not least, I would like to thank all Brazilians for their contributions through taxes, without which I could not have achieved half of what I did on the road to my Ph.D.

ABSTRACT

The Wilson-Cowan model serves as a classic framework for comprehending the collective neuronal dynamics within networks comprising both excitatory and inhibitory units. Extensively employed in literature, it facilitates the analysis of collective phases in neural networks at a mean-field level, i.e., when considering large fully connected networks. To study fluctuation-induced phenomena, the dynamical model alone is insufficient; to address this issue, we need to work with a stochastic rate model that is reduced to the Wilson-Cowan equations in a mean-field approach. Throughout this thesis, we analyze the resulting phase diagram of the stochastic Wilson-Cowan model near the active to quiescent phase transitions. We unveil eight possible types of transitions that depend on the relative strengths of excitatory and inhibitory couplings. Among these transitions are second-order and first-order types, as expected, as well as three transitions with a surprising mixture of behaviors. The three bona fide second-order phase transitions belong to the well-known directed percolation universality class, the tricritical directed percolation universality class, and a novel universality class called “Hopf tricritical directed percolation", which presents an unconventional behavior with the breakdown of some scaling relations. The discontinuous transitions behave as expected and the hybrid transitions have different anomalies in scaling across them. Our results broaden our knowledge and characterize the types of critical behavior in excitatory and inhibitory networks and help us understand avalanche dynamics in neuronal recordings. From a more general perspective, these results contribute to extending the theory of non-equilibrium phase transitions into quiescent or absorbing states.

Keywords: criticality; neuronal avalanches; Wilson-Cowan model; universality classes; directed percolation; scaling relation breakdown.

RESUMO

O modelo Wilson-Cowan é um modelo clássico para a compreenção da dinâmica coletiva de redes neurais com unidades excitatórias e inibitórias. Esse modelo foi extensivamente estudado na literatura, especialmente na análise de fases de redes neurais em uma aproximação de campo médio, ou seja, em grandes redes completamente conectada. Para estudar fenômenos induzidos por flutuações, o modelo dinâmico é insuficiente. Portanto, é importante introduzirmos um modelo estocástico de taxas que se reduz às equações de Wilson-Cowan na aproximação de campo médio. Nesta tese, analisamos o diagrama de fases do modelo estocástico de Wilson-Cowan acerca das transições ativo-quiescente. Desvendamos oito possíveis tipos de transições dependentes do valor relativo do acoplamento entre unidades excitatorias e inibitórias. Entre essas transições estão transições de segunda e primeira ordem, e adicionalmente encontramos três tipos de transições que possuem uma mistura de comportamento ou hibridas. As três transições verdadeiramente críticas pertencem às classes de percolação direcionada, percolação direcionada tricrítica e uma classe nova que chamamos de "percolação direcionada Hopf tricrítica", que apresenta um comportamento não convencional com quebras de relações de escala. As transições descontínuas se comportam como esperado e as híbridas apresentam diferentes anomalias entres elas. Nossos resultados ampliam o conhecimento sobre e caracterizam os tipos de comportamento crítico em redes excitatórias e inibitórias, alén de ajudar a compreender a dinâmica de avalanches em registros neuronais experimentais. De uma perspectiva mais geral, estes resultados contribuem para estender a teoria de transições de fase de não-equilíbrio entre estados quiescentes e absorventes.

Palavras-chave: criticalidade; avalanches neuronais; modelo de Wilson-Cowan; classes de universalidade; percolação direcionada; quebra de relações de escala.

LIST OF FIGURES

LIST OF TABLES

CONTENTS

1 CRITICALITY IN NEUROSCIENCE

Over the course of human history, all societies showed a significant curiosity about comprehending the mechanisms influencing human and animal physiology and behavior. The evolution of the central nervous system, which consists of the brain and spinal cord, has played a crucial role in the development and adaptation of organisms over time. This complex structure provides organisms with a range of adaptive advantages, such as sensory processing, i.e., detecting and responding to stimuli from the environment; motor control, essential for survival; and cognitive and social functions, allowing for the creation of societies and problem-solving depending on the complexity of the organism. An increasingly complex nervous system enhances the chances of survival and reproduction in dynamic ecological environments (GLICKSTEIN, 2017).

In this first chapter, we aim to motivate the reader to study the brain under the scope of statistical physics and, above all, under the framework of criticality. The first section summarizes the emergence of Neuroscience, followed by experimental results that support the critical brain hypothesis (BEGGS, 2007).

1.1 A BRIEF HISTORY: NEUROSCIENCE

The Edwin Smith surgical papyrus (1700 BCE) has the first written mention of the cortex or any part of the brain and is a copy of a much older document believed to be from Egypt's old kingdom and around 3000 BCE. Religion and spirituality were very prominent in prehistoric and early historic societies, making the Edwin Smith papyrus more interesting. Since the papyrus displays empirical descriptions of forty-eight patients starting at their heads down through their bodies, it constitutes evidence of scientific studies, departing from the common practices of the time. In ancient Egypt, as well as in other ancient civilizations, the heart was considered the source of senses and intellect (GROSS, 1999). In the Book of the Dead, for example, "the heart was the key to the afterlife" (see Fig. 1); when the subject reached the gates of the afterlife, the *weighing of the heart* ritual would begin. Anubis would weigh the subject's heart against the feather of Maat and quantify its worthiness (CARELLI, 2011; CASTELLANO, 2019). In Ancient China, medicine was not as focused on the heart, their healers had a more complex system that involved the heart as part of but not at the center. The brain only appears in Chinese scripts in the Jesuit Matteo Ricci's treatise. Alcmaeon of Croton (Greece, 5th century

Figure 1 – The weighing of the heart. Depicted in this figure is the Ani Papyrus, the most complete version of the Book of the Dead (78 feet from 1275 BCE). Ani was the royal scribe of Thebes. It shows the moment Anubis, the jackal god of mummification, weighs the Ani's heart. The Ani Papyrus is still held by the British Museum.

Source: (CASTELLANO, 2019)

BCE) pioneered in writing the idea that the brain is at the center of the senses, particularly vision (GROSS, 1999).

In ancient Rome, the Romans had a rudimentary knowledge of anatomy, and their medical understanding was heavily influenced by Greek traditions. Galen of Pergamon, the Greek physician who lived during the second century BCE, brought his medical knowledge to the Roman Empire. Although, he conducted dissections of animals the Roman approach to medicine was more theoretical and based on philosophical ideas rather than empirical observation and experimentation. The Roman contributions to neuroscience were more rooted in recording observations and descriptions rather than in-depth scientific inquiry. With the advent of the Renaissance and the revival of scientific inquiry, that neuroscience and the understanding of the brain began to evolve significantly (GROSS, 1999).

In illustrating the importance of research on the brain, let us explore some of the Nobel prizes in the area in the 20th century. Golgi and Ramón y Cajal were jointly awarded the Nobel Prize in 1906 for their complementary contributions revolutionizing our understanding of the structure of the nervous system. Edgar Douglas Adrian's works on single neurons and their electrophysiological function along with the first recording in an electroencephalogram awarded Sir Charles Scott Sherrington and him a Nobel prize in 1932 (GROSS, 1999). In 1944, Joseph Erlanger and Herbert Spencer Gasser were awarded the Nobel Prize in Physiology or Medicine

for their work on the functions of different types of nerve fibers, identifying and characterizing sensory and motor nerve fibers. Following up the study of single neurons, Hodgkin and Huxley impaled a giant axon of the squid, which has a cross-sectional area a hundred times bigger than that of a mammalian. They won the Nobel prize in 1963 alongside John Eccles for their analysis of the physical and chemical basis for electrical activity and the discovery of the action potential (GLICKSTEIN, 2017). Haldan Keffer Hartline introduced the concept of a visual receptive field sharing the Nobel prize with George Wald and Ragnar Granit in 1967. For the Nobel prize in 1981, David Hubel, Torsten Wiesel, and Roger Sperry revealed the functional architecture of the striate cortex, which promised a better understanding of perception and became a model for visual neurons (GROSS, 1999). At the turn of the milenium (2000), Eric R. Kandel, Arvid Carlsson, and Paul Greengard shared the Nobel Prize for discoveries concerning signal transduction in the nervous system. Although, Kandel's work had a focus on molecular mechanisms underlying learning and memory. For completion, this century John O'Keefe, May-Britt Moser and Edvard I. Moser were awarded the 2014 Nobel Prize because of their work on neuronal cells that provide a complex representation of spatial location (GLICKSTEIN, 2017).

Advances in molecular biology and genetics revolutionized neuroscience. New experimental techniques like optogenetics, functional magnetic resonance imaging (fMRI), and CRISPR ("Clustered Regularly Interspaced Short Palindromic Repeats", which allows scientists to make changes to the DNA of living beings) gene editing increase the ability to do research in animals and humans also *in vivo*. This advance in technology helps observe molecular and cellular mechanisms underlying neural function, synaptic transmission, and the genetic basis for the purposes of understanding regular subjects and neurological disorders. Current neuroscience research focuses on areas such as neuroplasticity, neuronal circuits, and the molecular basis of cognition and behavior, aiming to create advances in medicine and psychology using tools from many disciplines (GLICKSTEIN, 2017).

1.2 CRITICALITY IN THE BRAIN

A wide assortment of life phenomena emerge from big systems that consist of many interacting elements. When we think about amino acids in a protein, nucleotides in the double helix of the DNA, hepatic cells forming the liver, and neurons in the brain, there are two usual approaches to them: researchers either look at individual elements or clump them together in different sizes to see collective behavior and function. The latter type of approach is familiar to

physicists and is treated under the lens of statistical physics. Considering that the stationary states of a biological system are in between chaotic and well-ordered, it is postulated that many of these systems operate around a critical point, which would be reached through what came to be called self-organized criticality (BAK, 2013). The theory of self-organized criticality originates from models of sand piles (BAK; TANG; WIESENFELD, 1987). These models show periods of quiescence interrupted by *avalanches*, which follow a power law distribution of sizes and durations (MORA; BIALEK, 2011).

An interesting feature across many natural systems is continuous phase transitions between active and quiescent phases. Many experiments like crystal liquids, vortices in superconductors, turbulent regimes in Coutte cells, and so on display this behavior. However, epidemics are a great example of this feature: with the arrival of vaccines humanity was able to banish diseases because if there are no infected subjects the disease cannot spread; however, in the presence of one ill individual, the disease is able to travel to many vulnerable ones (MARRO; DICKMAN, 1999a; HINRICHSEN, 2000). Often, systems with this nature exhibit critical behavior belonging to the directed percolation universality class, as originally conjectured by Janssen and Grassberger (JANSSEN, 1981; GRASSBERGER, 1981).

Directed percolation stands out as one of the most robust classes of universal critical behavior operating beyond thermal equilibrium. This class describes many possible transitions into a quiescent phase, even when considering multiple fields (GRINSTEIN; LAI; BROWNE, 1989a). Furthermore, models belonging to this class, the branching process and the contact process (HARRIS, 2002; LIGGETT, 2004), were studied in a variety of contexts, standing in as toy models in materials science, turbulence, epidemics, theoretical ecology, social sciences,

Figure 2 – Experimental setup and Spontaneous correlated neuronal activity in cultures. A) Organotypic coronal cortex culture on an 8×8 multielectrode array, where *WM* represents white matter. B) Spontaneous LFP from 60 electrodes with periods of correlated activity.

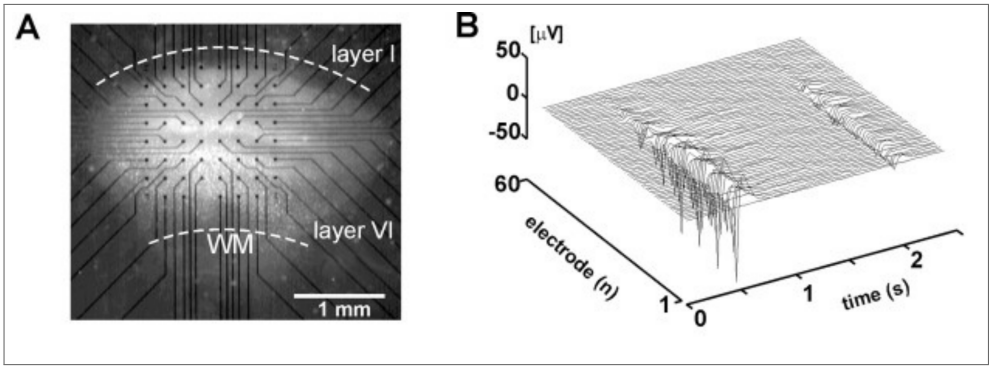

Source: Adapted from (BEGGS; PLENZ, 2003)

and neuroscience (BINNEY et al., 1993; OLAMI; FEDER; CHRISTENSEN, 1992; MARRO; DICKMAN, 1999a; HINRICHSEN, 2000; GRINSTEIN; MUÑOZ, 1996; HENKEL; HINRICHSEN; LÜBECK, 2008; ÓDOR, 2008; COTA; FERREIRA; ÓDOR, 2016).

In the context of neuronal systems, BEGGS; PLENZ (2003) published the first experimental evidence of the critical brain hypothesis (BEGGS, 2007) by studying organotypic cultures from coronal slices of rat somatosensory cortex with multi-electrode matrices with 60 channels (see

Figure 3 – Avalanche analysis. The top shows the raster of spontaneous activity and in the middle and bottom, this raster is separated into Δt windows ($\Delta t = 4$ ms). The duration of avalanches is counted from one empty window to the next and the size is the number of spikes occurring throughout this duration. The highlighted portion of the raster shows an avalanche of size $S = 39$ and duration $T = 12$ ms.

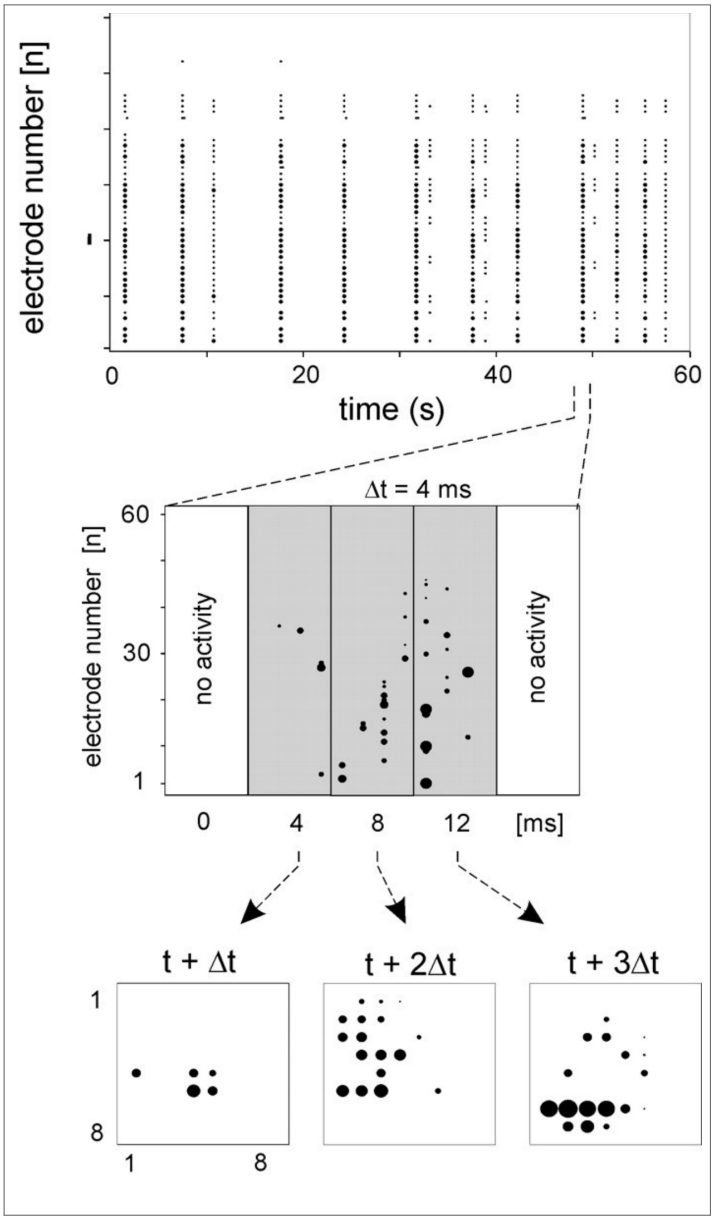

Source: Adapted from (BEGGS; PLENZ, 2003)

Fig. 2A). The matrix recorded the local field potential (LFP) – i.e., the voltage on an electrode relative to some other electrode taken as reference — and its deflections throughout the 60 channels showed the collective activity of the neurons (see Fig. 2B). BEGGS; PLENZ (2003) reported the existence of *neuronal avalanches*. These outbursts of neuronal activity between quiescent periods were computed by firstly separating the time into Δt-sized windows; an avalanche is defined by the sequence activity between two empty windows (silences). Secondly, they count the amount of activity, i.e., a signal above the determined threshold, in the associated electrode (see the top graph in Fig. 3).

The avalanches exhibited highly variable sizes (S) and durations (T), which were power-law

Figure 4 – Avalanche distribution for sizes and duration. A) Avalanche size distribution for different bin widths Δt with a cutoff at the maximal number of electrodes ($n = 60$). [inset] Dependence of the exponent ($\alpha \equiv \tau$) with the bin width Δt. B) Avalanche size distribution for different bin widths Δt for the summed LFP. (inset) Single culture distribution for $\Delta t = 1$ for all seven cultures. C) Duration distribution for different bin widths Δt. D) Normalized duration distribution ($t/\Delta t$).

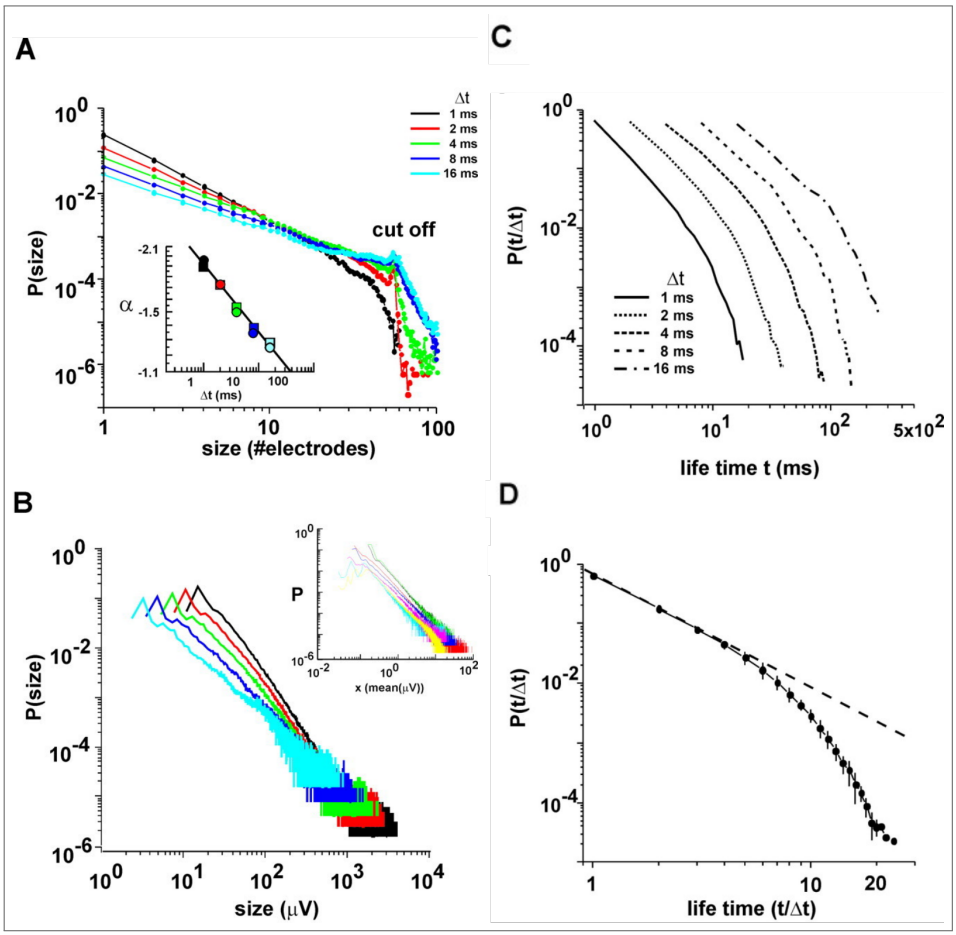

Source: (BEGGS; PLENZ, 2003)

distributed, i.e,

$$P(S) \propto S^{-\tau} \ , \tag{1.1}$$

$$P(T) \propto T^{-\tau_t} \ . \tag{1.2}$$

The size is defined as the number of electrodes active for the duration of the number of occupied windows after the binning (i.e., separating the time in Δt windows or bins). Concerning the duration distribution (Fig. 4C), less than a decade of the distribution follows a power law with $\tau_t \sim 2$, consistently with the mean-field directed percolation exponents. And the curves in Fig. 4D represent the data in Fig. 4C with the normalization $T \to T/\Delta t$. The avalanche sizes were distributed in a power law with exponent τ (in Fig. 4A represented by α), which also follows a power law $\tau(\Delta t) \sim \Delta^{-0.16\pm0.01}$. Additionally, in a different approach, they also found power law behavior for the distribution of the summed LFPs in a window of Δt, which also corresponds with the size of the avalanches (Fig. 4B). In order to test consistency, BEGGS; PLENZ (2003) also calculated the branching ratio as the ratio of descendant $(t+\Delta t)$ electrodes to ancestor (t) electrodes. The branching ratio was plotted against the avalanche size distribution exponent and they observed that there was an overlap of $\sigma = 1$ and $\tau = 1.5$ (values consistent with the mean-field DP universality class) at a bin size of $\Delta = 4$ msec, which is close to the averaged interevent interval ($IEI_{avg} = 4.2$ msec), the optimal calculated bin for their setup. These results suggest that brain dynamics is poised at a phase transition, i.e., it supports the critical brain hypothesis (BEGGS, 2007), and that the phase transition belongs to the well-known directed percolation universality class (BEGGS; PLENZ, 2003). Further research on LFP found similar results, in particular with anesthetized rats *in vivo* and awake monkeys, reinforcing the hypothesis (GIREESH; PLENZ, 2008; PETERMANN et al., 2009; CHIALVO, 2010; FRIEDMAN et al., 2012; CHIALVO, 2018; PLENZ et al., 2021; O'BYRNE; JERBI, 2022).

1.3 DIVERGING FROM DIRECTED PERCOLATION

Though very robust in representing many quiescent to active transitions, the directed percolation universality class is not unique, the presence of anomalous dimensions or symmetries changes the exponents. Other experimental setups have reported evidence of some scaling exponents that deviate from directed percolation (FRIEDMAN et al., 2012; RIBEIRO; RIBEIRO; COPELLI, 2016; PONCE-ALVAREZ et al., 2018a; FONTENELE et al., 2019). Therefore, the interpretation of the scaling behavior and the universality classes remains an open question.

An additional and important hallmark of criticality is the relationship between the scaling behavior of the avalanche distributions, which we will go through in detail in the next chapter. The mean size of an avalanche for a duration T is related to the conditional probability, $P(S|T)$, a probability of an avalanche of size S with duration T. This quantity should scale with the duration of said avalanche as $\langle S \rangle \sim T^{\gamma}$, where γ, in its turn, is related to the exponents of the size and duration distributions as $\gamma = (\tau_t - 1)/(\tau - 1)$ (the so-called crackling noise scaling relation) (MUÑOZ et al., 1999; SETHNA; DAHMEN; MYERS, 2001). Considering the aforementioned avalanche distribution exponents for the mean-field directed percolation universality class, the crackling noise exponent is expected to be $\gamma = (2-1)/(3/2-1) = 2$. FRIEDMAN et al. (2012) found $\tau \sim 1.7$, $\tau_t \sim 1.9$ and $\gamma \sim 1.3$ in cultured cortical slices (*in vitro*), whereas PONCE-ALVAREZ et al. (2018a) found $\tau \sim 2.9$, $\tau_t \sim 2.0$ and $\gamma \sim 1.9$ in whole-brain *in vivo* Zebrafish, confirming the signatures of criticality but with a different scaling behavior.

Furthermore, BEGGS; PLENZ (2003) worked on *in vitro* setups, while RIBEIRO; RIBEIRO; COPELLI (2016) found avalanche behavior in freely-behaving rats, which showed different patterns of distribution for different states of neural processing. Recently, FONTENELE et al. (2019) analyzed spike data from the primary visual cortex of urethane-anesthetized rats. In this paper, the spiking activity oscillated between different levels of synchrony, characterized in terms of the population rate coefficient of variation (CV), which was used as a proxy to represent different cortical states. The CV is a measure of relative variability and is the ratio of the standard deviation to the mean of a set of data, $CV = \text{std. deviation}/\text{mean}$. The coefficient of variation compares the relative variability of different data sets, especially when the means of the sets are different. A lower CV indicates lower relative variability, while a higher CV indicates higher relative variability.

Those states showed scaling behavior throughout the range of CVs (see Fig. 5a); however, it only fit the crackling noise scaling relation between τ, τ_t, and γ at a range of intermediate values of CV (see Fig. 5b). Though respecting the relationship between exponents, the exponents themselves did not fall into the mean-field directed percolation universality class, FONTENELE et al. (2019) found $\tau = 1.52 \pm 0.09$, $\tau_t = 1.7 \pm 0.1$, and $\gamma = 1.28 \pm 0.03$ in the intermediate CV range. Strikingly, when comparing to many other experimental results across the literature, they observed that there is a tendency of $\gamma \sim 1.3$ for different experimental setups, indicating a different universality class. This apparent departure from directed percolation could be a result of a myriad of processes since the brain is very complex. However, CARVALHO et al.

(2021) showed a viable candidate for this reason is subsampling, in the paper the authors compare the subsampling of a model belonging to the directed percolation universality class to the experimental results in FONTENELE et al. (2019).

These indications of a different universality class from directed percolation associated with the evidence of discontinuous transitions in the brain dynamics (MILLMAN et al., 2010; CORTES et al., 2013; MARTINELLO et al., 2017) rekindle the search for alternative types of critical behavior, including multicritical behavior. Observe that directed percolation behavior is easily achieved by models presenting with only one relevant field; therefore, the role of an extra population, as an example an inhibition population, on the overall critical behavior

Figure 5 – (a) Crackling noise relation of spike avalanches across different levels of CVs. In green is a high CV, in red is an intermediate CV, and in purple is a low CV. (b) Representation of the mean values of the fit exponents for different values of CV, in blue the crackling noise exponent and in grey the value of the scaling relation with the avalanche distribution exponents (τ and τ_t). The shadow around each curve is its standard deviation. The gray vertical stripe represents the range of CV values where the crackling noise relationship is obeyed considering the standard deviations, i.e., around $\langle CV \rangle^* = 1.4 \pm 0.2$. (c) Linear tendency of critical exponents across animals and experimental setups. In black, FONTENELE et al. (2019) marked their value for mean-field directed percolation.

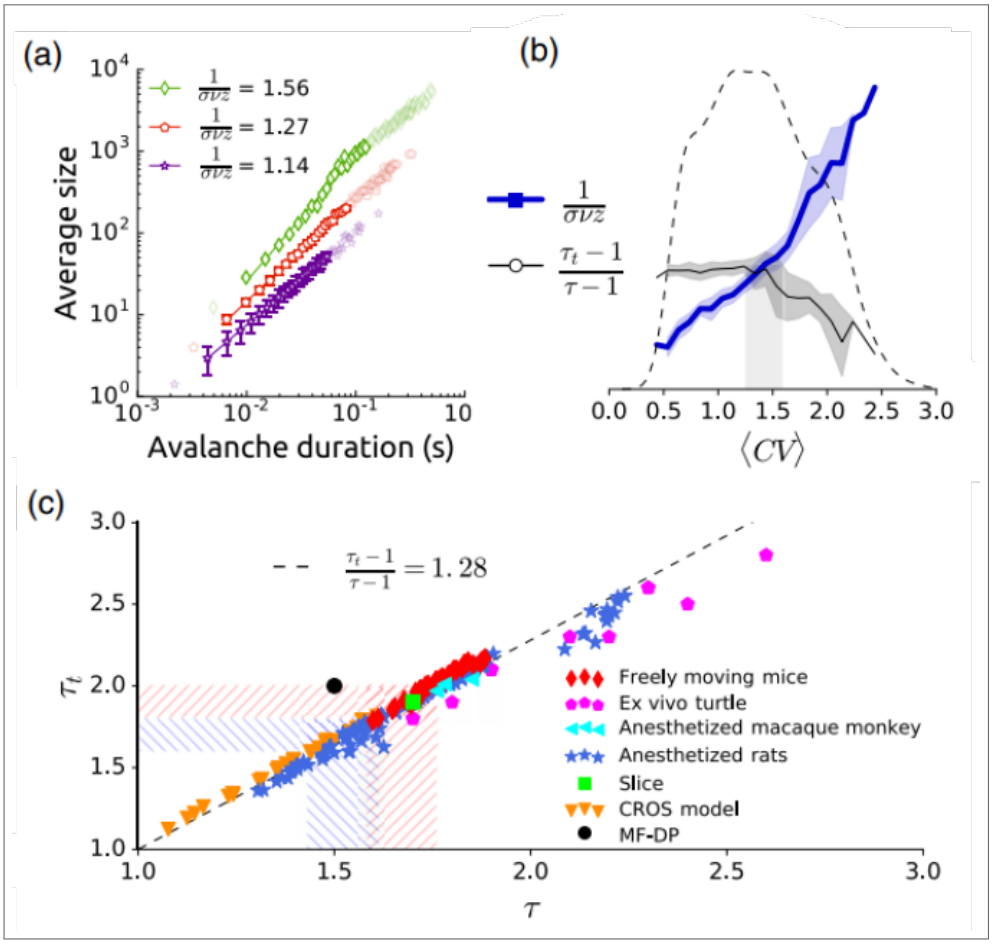

Source: (FONTENELE et al., 2019)

has actively been explored (BENAYOUN et al., 2010; ASSIS; COPELLI, 2009; KINOUCHI; COPELLI, 2006; GIRARDI-SCHAPPO et al., 2021; GIRARDI-SCHAPPO et al., 2020; APICELLA et al., 2022; LÓPEZ; BUENDÍA; MUÑOZ, 2022).

Considering these questions, throughout this thesis, we will focus on the Wilson-Cowan model in its dynamic and stochastic forms. The second chapter shows an overview of three quiescent to active universality classes: directed percolation, tricritical directed percolation, and asymmetrically coupled directed percolation. The third chapter introduces both forms of the Wilson-Cowan model, the dynamic equations and the stochastic counterpart. The fourth chapter scrutinizes the eight possible types of transitions we have found in the Wilson-Cowan stochastic model. And, finally, the fifth chapter summarizes our conclusions and describes the questions that remain open.

2 UNIVERSALITY CLASSES: QUIESCENT TO ACTIVE

A universality class classifies different systems with similar behavior near a critical point or phase transition, despite having diverse microscopic features.

Systems in the same universality class share common qualitative properties at critical points, such as critical phenomena or emergent behaviors. These similarities are independent of the specific details of the system, like its microscopic structure, the precise nature of interactions, or the specific components involved.

The concept of universality classes is significant because it allows researchers to categorize and understand a broad range of systems based on their collective behavior, rather than focusing on the individual details of each system. It helps simplify the understanding of complex physical phenomena and allows for applying shared principles or models to diverse systems that exhibit similar behavior near critical points.

In this chapter, we are going to explore quiescent to active transitions that belong to three known universality classes. The first section explains a bit the idea behind focussing on a mean-field approach to the transitions. The second shows a generalized calculation of the exponents depending on the Langevin equation. The third and forth sections dissect the direct percolation and tricritical directed percolation universality classes. The last section elucidates the asymmetrically coupled directed percolation and, as a special case, unidirectionally coupled directed percolation.

2.1 MEAN-FIELD THEORY

In this chapter, and throughout the thesis, we will focus on a mean-field approach to the transitions.

One of the reasons to work with mean-field exponents is the exponents found by BEGGS; PLENZ (2003), which were consistent with mean-field directed percolation (the avalanche exponents $\tau = 3/2$ and $\tau_t = 2$), as mentioned in Chapter 1. The proper dimensionality of the brain will depend on the choice of the order parameter, however, a simple model with an all-to-all connection is sufficient to describe the avalanche critical activity of a *in-vitro* slice of cortical tissue.

Mean-field theory is useful when studying large populations, particularly for this thesis,

of neurons. Mean-field theory simplifies the description of neural dynamics by considering the mean activity of a population rather than individual neurons. If we think in terms of thermodynamics and statistical physics, the mean-field theory brings us from a microscopic to a macroscopic or phenomenological point of view. The many advantages of using mean-field approaches include computational efficiency, reduced parameters, and analytical solutions, which we are going to derive in the next section.

As follows, we can describe a model in terms of a Langevin equation, which can be divided into mean-field terms, a noise term, and a spatial term. The mean-field term can be especially interesting when we treat it as a dynamic equation.

Observe that in the case of directed percolation, the mean-field part of the equation is a second-order equation ($-x^2 + ax$). At the transition ($a = 0$), it becomes a well, which means the only attractor is the origin. When the only solution is the origin, for any initial condition, the system will relax to zero, this is true at the transition, and when $a < 0$, the stable solution keeps on being the only attractor. Macroscopically, we can say that the overall activity of the system for $a \leq 0$ eventually dies out. Microscopically, the activity propagates for a bit of time and eventually ceases, where the few active sites do not propagate it. Dynamically, at the value $a = 0$, there is a transcritical bifurcation, therefore, this bifurcation is correlated to the transition. They share the characteristic of going from a configuration where the system only finds one stable configuration in no “activity" to a configuration where a stable “activity" arises.

Observe that the comparison is only possible at a mean-field approximation of the microscopic system. However, it indicates that the study of bifurcations in the mean-field equation might correlate to different types of transitions in the microscopic system.

Observe that we are not confirming that there is a one-to-one relationship with a bifurcation to a specific transition. Our results (Chap. 4) show several examples of this relationship, attributing some bifurcations to transitions, where a few of them are actually critical.

2.2 ANALYTICAL CALCULATIONS OF EXPONENTS

Whenever we think about universality classes as physicists, the first subject that comes to mind is scale-invariance, i.e., the scaling exponents. Numerous observables linked to these exponents are often challenging to compute analytically. Among these observables are the spreading quantities that exhibit scale invariance at the critical point: the number of active

sites at an instant (t), $N(t) \propto t^{\eta}$; the mean-squared radius in surviving runs, $R^2(t) \propto t^z$; and the survival probability, $P_s(t) \propto t^{-\delta}$ (MARRO; DICKMAN, 1999a).

Systems featuring quiescent states exhibit a minimum of two phases: active and quiescent phases. In the quiescent phase, any elicited activity relaxes to quiescence after a finite period of time. Starting from a single active seed, the activity decays to zero unequivocally. The probability of any activity persisting beyond zero at a given instant t is the survival probability, $P(t)$. In the quiescent phase, this probability decays exponentially, and in the active phase, the system displays self-sustained activity, causing the probability to maintain a positive value. Separating these phases is a critical point or a surface of critical points. At this point or surface, the survival probability decays according to a power law. The associated exponent is known to be exclusively calculated in a stochastic manner, $P_s(t) \propto t^{\delta}$. In this section, we are going to follow the procedures in MUÑOZ; GRINSTEIN; TU (1997) from a generalized Langevin equation and through scaling analysis find the exponents of active to quiescent critical behavior.

Generalizing a Langevin equation in terms of the field $\phi(\vec{x}, t)$ as the order parameter, which depends on position vector $\vec{x}$ in $\mathcal{R}^d$ and time t,

$$\dot{\phi}(\vec{x}, t) = a\ \phi(\vec{x}, t) - b\ \phi(\vec{x}, t)^{\alpha} + h(\vec{x}, t) + \nu\ \nabla^2\ \phi(\vec{x}, t) + \sqrt{\phi}\ \eta(\vec{x}, t)\ , \tag{2.1}$$

where the field ϕ is the measurement; the parameters a and b are called control parameters, and their values define the position of the system at a phase diagram. Connecting these quantities to the experiments mentioned in Chapter 1, the spikes are the proposed order parameter since they are the measured activity. The control parameter is a harder quantity to find, in many experiments, the input current is chosen, however, in trying to “control" spontaneous activity it is lacking. Therefore, FONTENELE et al. (2019) proposed the use of the CV as a control parameter since it was already used in the literature to denote cortical states.

Equation 2.1 is divided into two parts: the mean-field dynamics,

$$\dot{\phi}(\vec{x}, t) = a\ \phi(\vec{x}, t) - b\ \phi(\vec{x}, t)^{\alpha} + h(\vec{x}, t)\ , \tag{2.2}$$

where the external field also depends on the space and time, $h(\vec{x}, t)$, a is the distance to the critical point, $b > 0$, and α governs the decay to the quiescent state and it is generally $\alpha > 1$; the diffusion term is $\nu\ \nabla^2\ \phi(\vec{x}, t)$, where ν is constant and ∇^2 is the Laplace operator; and the noise term is $\sqrt{\phi}\ \eta(\vec{x}, t)$, where η is a Gaussian noise with the correlation

$$\langle \eta(\vec{x}_1, t_1)\eta(\vec{x}_2, t_2)\rangle = \mathcal{D}\delta(\vec{x}_1 - \vec{x}_2)\delta(t_1 - t_2)\ . \tag{2.3}$$

The most straightforward scale-invariant observables to calculate come from the mean-field equation. The stationary solution of the mean-field equation, Eq (2.2), yields static exponents. The first one, β, governs the growth of the order parameter as a function of the control parameter near criticality, $a \to 0^+$, $\phi(\vec{x}, t; h = 0) \propto a^{1/(\alpha-1)} \propto a^{\beta}$, yielding

$$\beta = \frac{1}{\alpha - 1} \, . \tag{2.4}$$

At the critical point, $a = 0$, and introducing a small external field, $h \to 0$, the stationary solution is scale-invariant and scales with exponent δ_h. From Eq. (2.2), $\phi(\vec{x}, t) \propto h^{1/\alpha} \propto h^{1/\delta_h}$, one obtains

$$\delta_h = \alpha \, . \tag{2.5}$$

Considering the entire Langevin equation, Eq. (2.1), the dimensions of each term have to match. Therefore, $[\dot{\phi}] = [\nu \ \nabla^2 \ \phi]$ results on the spreading exponent z ($R^2(t) \propto t^z$). Using dimensional analysis, $T^{-1} \ \propto \ L^{-2} \Rightarrow t \ \propto \ R^2 \ \propto \ t^z$, we find the scaling relation

$$z = 1 \, , \tag{2.6}$$

where T is a generalized time dimension and L, a space dimension, consistently with the known result for DP $\langle R^2 \rangle = 2Dt$.

The primary objective of the study by MUÑOZ; GRINSTEIN; TU (1997) was to investigate the survival probability. The initial approach involves examining the accumulation of the probability density around the absorbing state, i.e., the *piling probability*. Considering $P(c, t)$ the probability that $\int d^d x \ \phi > c$, the piling probability scales with time as $P(c, t) \propto t^{-\delta}$. Diverging from the paper itself, here we will study the noise probability.

Considering the noise as independent and Gaussian, with random variable η and standard deviation σ. The overall probability is, therefore, a product of their probability distribution $\left[P(\eta) = \exp\left(-\frac{\eta^2(\vec{x},t)}{2\sigma^2}\right)\right]$ over sites ($\vec{x}$) and discrete time steps (t), i.e., $(\prod_{\vec{x}} \prod_t)$. When we consider continuous space and time and the nature of the exponential function (product of powers, where if we have a product of two powers with the same base we can sum them), is represented by

$$P(\{\eta(\vec{x})\}_t) = \mathcal{Z} \prod_{\vec{x}} \prod_t \exp\left(-\frac{\eta^2(\vec{x}, t)}{2\sigma^2}\right) \tag{2.7}$$

$$= \mathcal{Z} \exp\left(-\int dt \int d^d x \ \frac{\eta^2(\vec{x}, t)}{2\sigma^2}\right) , \tag{2.8}$$

where $\mathcal{Z}$ represents a normalizing constant and $\sigma^2 = \mathcal{D}$ is the variance.

Rearranging Eq. (2.1), the noise term moves to the left-hand side of the equation and the derivative moves to the right-hand side,

$$\sqrt{\phi}\,\eta(\vec{x},t) = \dot{\phi}(\vec{x},t) - a\,\phi(\vec{x},t) + b\,\phi(\vec{x},t)^{\alpha} - h(\vec{x},t) - \nu\,\nabla^2\,\phi(\vec{x},t)\,. \tag{2.9}$$

Furthermore, we want to introduce a response field (Ψ) that accounts for the perturbation around the initial condition, i.e., $\vec{x}_0 = \vec{x}(t_0)$. To accomplish that, we will do a reverse completing the binomial, we are going to open up the binomial to find consistent terms. As a reminder, consider the transformation

$$\mathcal{N}\exp\left\{\frac{1}{2}A_{ij}Z_iZ_j\right\} = \int DY\exp\left\{-\frac{1}{2}A_{ij}Y_iY_j + Z_iY_i\right\}\,, \tag{2.10}$$

where $Z_i = \eta(\vec{x},t)$, $Y_i = \Psi$, and $A_{ij} = (\mathcal{D}/2)\,\phi$, which is the covariance matrix, describing the covariance relationships between different stochastic variables. The square matrix summarizes their variances and covariances. So the final expression for the probability, Eq. (2.8), is

$$\int D\phi\int D\Psi\;\mathcal{Z}\exp\left(-\int d^dx\int dt\left\{\left(\dot{\phi} - a\phi + b\phi^{\alpha} - h - \nu\nabla^2\phi\right)\Psi + \frac{\mathcal{D}}{2}\phi\Psi^2\sigma^2\right\}\right). \tag{2.11}$$

The upper critical dimension is the value of d above which the system displays mean-field behavior. Observe that the argument of the exponent should be dimensionless. The argument of the exponential is:

$$-\int d^dx\int dt\left\{\left(\dot{\phi} - a\phi + b\phi^{\alpha} - h - \nu\nabla^2\phi\right)\Psi + \frac{\mathcal{D}}{2}\phi\Psi^2\sigma^2\right\}\,. \tag{2.12}$$

On one hand, we need the space dimension in the integral because of the term $\nu\nabla^2\phi\Psi$ to cancel out with $[\phi\Psi]$, i.e., $L^{d_c}[\phi\Psi] = 1$. On the other hand, the terms of the integral also need to have the same dimension as one another and as L^{d_c}. Considering now the relationship between the dimension of $[b\phi^{\alpha}\Psi]$ and $[\mathcal{D}\phi\Psi^2\sigma^2]$, we find

$$[\phi^{\alpha}\Psi] = [\Psi^2\phi] \Rightarrow [\Psi\phi] = [\phi]^{\alpha} \Rightarrow [\phi]^{\alpha} = L^{-d_c}\,. \tag{2.13}$$

To find the dimensions of $[\phi]$, we need to consider the terms $a\phi$ and $\nu\nabla^2\phi$, which results in $[a] = L^{-2}$. Thus, the dimension of $[\phi]$ is $[\phi] = [a]^{\beta} = L^{-2/(\alpha-1)}$ (Substituting in 2.13), which concludes with the relation,

$$d_c = \frac{2\alpha}{\alpha - 1}\,. \tag{2.14}$$

The exponent that governs the time decay The dynamic exponent θ as a function of α can use the result of the upper critical dimension since we expect $\phi \propto t^{-\theta}$. Observe that $[\phi] = L^{-d_c/\alpha} = T^{-d_c/2\alpha}$ results in

$$\theta = \frac{d_c}{2\alpha} = \frac{1}{\alpha - 1}\,. \tag{2.15}$$

Finally, the spreading exponent for the survival probability δ is calculated considering the relations we have drawn up to this point, $[\Psi] = [\phi]^{\alpha-1}$ and that the piling probability scales like the response field we introduced before, i.e., $[P(c,t)] = [\Psi]$; therefore,

$$\delta = \frac{d}{2}\frac{\alpha-1}{\alpha} = \frac{\alpha}{\alpha-1}\,\frac{\alpha-1}{\alpha} = 1. \tag{2.16}$$

The same approach allows us to derive additional exponents and their scaling relations. An important set of exponents that are not explicitly worked out in this analysis is the set of correlation exponents. The correlation between units measures how synchronous their activity is in relation to time and space, the strength and direction of this observable is the correlation coefficient. In the supercritical regime ($\Delta > 0$), one expected the spatial and time correlations to decay exponentially as $C(\vec{x}) \propto e^{-|\vec{x}|/\xi}$ and $C_s(t) \propto e^{-t/\tau}$, respectively. Furthermore, the correlation length ξ and relaxation time τ diverge for $\Delta = 0$ according to $\xi \sim |\Delta|^{-\nu_\perp}$ and $\tau \sim |\Delta|^{-\nu_\parallel}$. Particularly, MARRO; DICKMAN (1999a) used a more analytical approach from the Langevin equation for the contact process but neglected the higher orders in ϕ to conclude that the correlation length exponent $\nu_\perp = 1/2$ and $\nu_\parallel = 1$, which should be valid for the generalized Langevin we wrote here since it is independent of α. As an extra scaling relation, GRASSBERGER (1981) calculates

$$z = \frac{2\nu_\perp}{\nu_\parallel} = 1\ , \tag{2.17}$$

which agrees with the values for these exponents perfectly.

In what follows, we apply these methods in the context of three different universality classes.

2.3 DIRECTED PERCOLATION

2.3.1 Contact Process

The contact process is a Markovian branching process that belongs to the directed percolation universality class (DP) and serves as a continuous toy model of an epidemic, widely applied in epidemic studies disregarding immunization. Known for its accurately identified critical values and essential attributes, it is often regarded as the Ising model equivalent for the DP universality class (MARRO; DICKMAN, 1999a).

In the contact process, the network is made out of individual sites, which are active or inactive. Each active site can either die out with probability $1/(\lambda+1)$ or propagate its activity

Figure 6 – Schematics of rates for the Contact Process model. Observe that these schematics are considering the system in a mean-field approach, i.e., the network is completely connected.

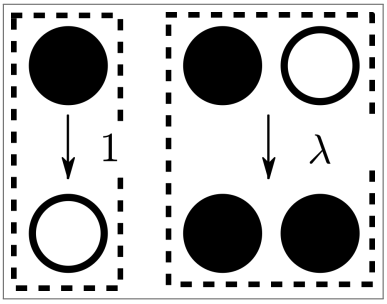

Source: The author (2023)

to a neighbor with probability $\lambda/(\lambda+1)$, i.e.,

$$\begin{aligned} A &\to 0 \quad \text{with probability} \quad 1/(\lambda+1) \\ A &\to AA \quad \text{with probability} \quad \lambda/(\lambda+1). \end{aligned}$$

Therefore, the transition rates are 1 for decay and λ for activation (see Fig. 6). As we evaluate the network's overall activity as $t \to \infty$, it is poised at a quiescent phase if the sum of activity converges to zero, or at an active phase if the sum of activity converges to a positive value, indicative of self-sustained activity. The transition between these phases is a bona fide critical point, meaning it is a second-order phase transition.

Considering a continuous time Markov model, we are able to build the dynamics of each site and gain some intuition on the behavior of the system through a mean-field analysis. In constructing the model, let us consider:

$$\sigma_x(t) \;=\; \begin{cases} 1 & \text{if } x \text{ is occupied} \\ 0 & \text{if } x \text{ is vacant,} \end{cases} \tag{2.18}$$

and $\text{Prob}(\sigma_x(t)=1) \equiv P(x,t)$. The dynamics of $P(x,t)$ takes the form

$$\frac{d}{dt}P(x,t) = -P(x,t) + \frac{\lambda}{q}\sum_y \text{Prob}(\sigma_x(t)=0, \sigma_y(t)=1), \tag{2.19}$$

where the first term on the right side is a negative term for annihilation; y is one of the neighbors of x; the activation term scales with the infecting rate, λ/q; and q is the lattice number or coordination number, i.e., the number of neighbors (MARRO; DICKMAN, 1999a).

2.3.2 Mean-field Equation

In the mean-field approximation, the states of activity are independent at each site, i.e., Prob$(\sigma_x(t) = 0, \sigma_y(t) = 1) =$ Prob$(\sigma_x(t) = 0)$Prob$(\sigma_y(t) = 1)$; all sites are connected to one another, a fully-connected and uncorrelated network; and the space is homogeneous, i.e, $P(x,t) = P(y,t)$. From Eq. (2.19),

$$\frac{d}{dt}P(x,t) = -P(x,t) + \frac{\lambda}{q}\sum_{y}\left[(1 - P(x,t))P(y,t)\right] , \tag{2.20}$$

$$= -P(x,t) + \lambda\left[(1 - P(x,t))P(x,t)\right] . \tag{2.21}$$

When we sum over all possible x, we find that, for a homogeneous fully-connected network, $\rho(t) \equiv (1/N)\sum_x P(x,t)$ — where N is the size of the network and $\rho(t)$ is the instantaneous density of active sites. And, by summing over the terms in Eq. (2.21),

$$\frac{d}{dt}\rho(t) = -\rho(t) + \lambda\left[(1 - \rho(t))\rho(t)\right] , \tag{2.22}$$

one can write the most commonly known mean-field equation for the contact process,

$$\frac{d}{dt}\rho = (\lambda - 1)\rho - \lambda\rho^2 . \tag{2.23}$$

From Eq. (2.23), the quiescent state, $\rho = 0$, is always a solution. However, an active state, i.e., $\rho^* \neq 0$, emerges depending on the control parameter, λ. Observe that the equation has

Figure 7 – Spread of the Contact Process in one dimension starting from a single active particle. From left to right: $\lambda = 3.0$ (subcritical regime), $\lambda = 3.2978$ (very close to the critical point), and $\lambda = 3.5$ (supercritical regime). The time evolves in a straight vertical downwards line.

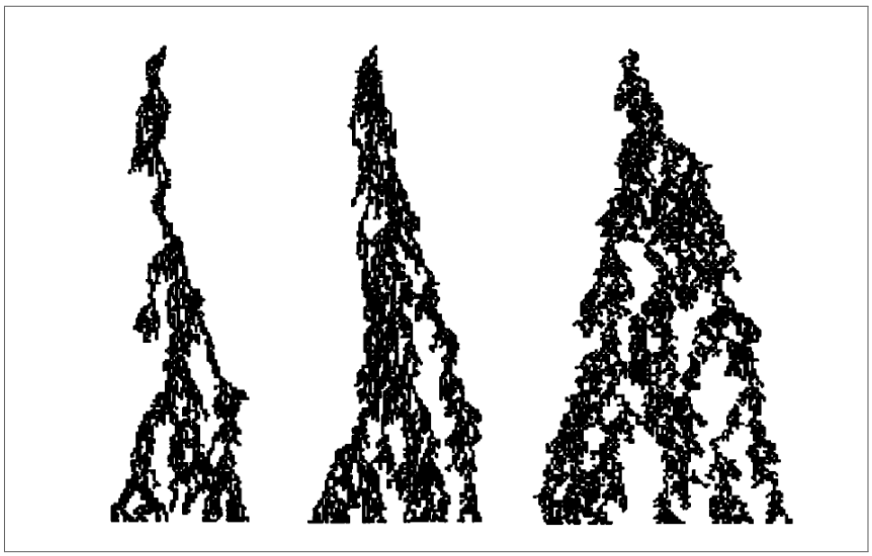

Source: (MARRO; DICKMAN, 1999a)

two possible fixed points:

$$\bar{\rho}_1 = 0 \tag{2.24}$$

$$\bar{\rho}_2 = \frac{\lambda - 1}{\lambda} = 1 - \frac{1}{\lambda}. \tag{2.25}$$

For $\lambda < 1$, the second solution is negative and, therefore, cannot represent a density and is an invalid solution to our system. However, for $\lambda > 1$, both solutions are valid. The system goes through a transcritical bifurcation, where the quiescent state retains the status of fixed point and it loses stability to an active state, which becomes the only attractor. These two phases are separated at the critical value of the control parameter, $\lambda_c = 1$, above which the mean-field equation allows a nontrivial stationary solution (MARRO; DICKMAN, 1999a).

2.3.3 Directed Percolation Universality Class

At the critical point, the anticipated scale-free behavior in the order parameter is characterized by power-law dynamics. Moreover, the specific exponents dictating such behavior are thoroughly documented for Directed Percolation (MUÑOZ; GRINSTEIN; TU, 1997; MARRO; DICKMAN, 1999a; MUÑOZ et al., 1999; MUÑOZ, 2018; FERREIRA; FERREIRA; PASTOR-SATORRAS, 2011).

The expansion of Eq. (2.25) yields the exponent that drives the static solution for $\lambda \geq \lambda_c$ as a function of $\Delta = |\lambda - \lambda_c|$, $\bar{\rho}(\Delta; h = 0) \propto \Delta^{\beta}$. Expanding $\bar{\rho}$, we find

$$\begin{aligned}
f(\lambda = \lambda_c) &= 1 - \frac{1}{\lambda_c} = 0 \,, \\
f'(\lambda = \lambda_c) &= \frac{1}{\lambda_c^2} = 1 \,, \\
f''(\lambda = \lambda_c) &= -\frac{2}{\lambda_c^3} = -2 \,, \\
\bar{\rho}\,(\Delta; h = 0) &\approx f(\lambda_c) + (\lambda - \lambda_c)\, f'(\lambda_c) + \frac{(\lambda - \lambda_c)^2}{2}\, f''(\lambda_c) + \mathcal{O}(\lambda^3) \qquad (2.26) \\
&\approx \Delta + \mathcal{O}(\Delta^2) \,, \qquad (2.27)
\end{aligned}$$

resulting in $\beta = 1$.

Including a spontaneous infection term, the absorbing state is no longer a fixed point. The mean-field equation becomes

$$\frac{d}{dt}\rho = (\lambda - 1)\rho - \lambda\rho^2 + h(1 - \rho) \,, \tag{2.28}$$

where the static solution is

$$\bar{\rho}\left(\Delta;h\right) = \frac{\Delta-h\pm\sqrt{(\Delta-h)^2+4(\Delta+\lambda_c)h}}{2(\Delta+\lambda_c)} \tag{2.29}$$

$$\bar{\rho}\left(\Delta=0;h\right) = \frac{-h\pm\sqrt{h^2+4h}}{2} \tag{2.30}$$

$$= \sqrt{h}\left[\frac{-\sqrt{h}\pm\sqrt{h+4}}{2}\right] . \tag{2.31}$$

Around $h=0$, the solution approximates to

$$\bar{\rho}\left(\Delta=0;h\right)\approx\sqrt{h}-\frac{h}{2}+\mathcal{O}(h^{3/2}) , \tag{2.32}$$

at the critical point. Thus, the second static solution scales as $\bar{\rho}\propto h^{1/2}$, as $h\to 0$, and the external field exponent, δ_h, defined by $\bar{\rho}(0;h)\propto h^{1/\delta_h}$, is 2.

Another hallmark of critical systems is a prolonged relaxation time, i.e., the time taken for the system to return to equilibrium after a disturbance, called critical slowing down. Critical slowing down occurs in physical systems near critical points or phase transitions. As a physical system approaches a critical point, such as a phase transition, the system becomes more sensitive to changes. This heightened sensitivity manifests in the system's response to perturbations, indicating an increase in relaxation times or the time needed for fluctuations to die out, which increases significantly as the system approaches criticality. Critical slowing down is often an indicator or precursor of an imminent phase transition. In the contact process, when $\lambda\neq\lambda_c$ and $h=0$, we expand Eq. (2.25) around $\rho=\bar{\rho}$,

$$\frac{d}{dt}\rho \approx \left[(\lambda-1)-2\lambda\bar{\rho}\right](\rho-\bar{\rho})+\mathcal{O}\left[(\rho-\bar{\rho})^2\right] \tag{2.33}$$

$$\approx -(1+\lambda)(\rho-\bar{\rho})+\mathcal{O}\left[(\rho-\bar{\rho})^2\right] . \tag{2.34}$$

Considering a change of variable $\rho\to\rho+\bar{\rho}$, where $\bar{\rho}$ is constant and $\frac{d}{dt}\rho=\frac{d}{dt}(\rho-\bar{\rho})$, the equations solves to:

$$\frac{d}{dt}(\rho-\bar{\rho}) \approx -(1+\lambda)(\rho-\bar{\rho})+\mathcal{O}\left[(\rho-\bar{\rho})^2\right] , \tag{2.35}$$

$$\rho-\bar{\rho} \propto \exp\left\{-|1-\lambda|\,t\right\} . \tag{2.36}$$

The previous analysis yields two conclusions: near the critical point, the relaxation time (τ) scales with $1/|1-\lambda|$, showing critical slowing down; and, at the critical point,

$$\frac{d}{dt}\rho = -\rho^2 , \tag{2.37}$$

$$\rho(\Delta=0,h=0;t) \propto t^{-1} , \tag{2.38}$$

defining $\theta = 1$ as the dynamical exponent ($\rho \propto t^{-\theta}$).

Only three of the exponents are actually independent, the others follow well-known scaling relations, which are summarized in MUÑOZ et al. (1999). Apart from the static and dynamic exponents mentioned above, critical systems display scale-free behavior for the spreading quantities $N(t)$, $R^2(t)$, and $P_s(t)$ — respectively: average total active sites, squared linear spread of active sites, and survival probability. At the critical point, these quantities decay with time driven by the exponents η, z, and δ, respectively.

Due to the diffusive nature of the system, correlations should behave like $C(\vec{x}; \Delta = 0) \propto e^{-|x|/\xi_\perp}$ and $C_s(t; \Delta = 0) \propto e^{-t/\xi_\parallel}$, where $\xi_\perp$ is the correlation length and $\xi_\parallel$, the relaxation time. The quantities $\xi_\perp$ and $\xi_\parallel$ diverge as Δ approaches zero with exponents $\nu_\perp$ and $\nu_\parallel$, respectively.

Considering that, for this system, $\alpha = 2$, when its configuration is above the upper critical dimension — i.e., $d_c = 4$ — we have already calculated β, δ_h, and θ. Additionally, from the calculations in Sec. 2.2, we also find $\eta = 0$, $z = 1$, $\delta = 1$, $\nu_\perp = 1/2$, and $\nu_\parallel = 1$.

Figure 8 – Avalanche mean-temporal profile from two experimental results in the most left and right panels and simulation of a DP model in the center panels. These shapes are produced by averaging the temporal profiles of all avalanches of a particular duration. Observe that for sample 6 (far right panels) there is neither collapse nor parabolic shapes, indicating that not all the experimental samples were critical.

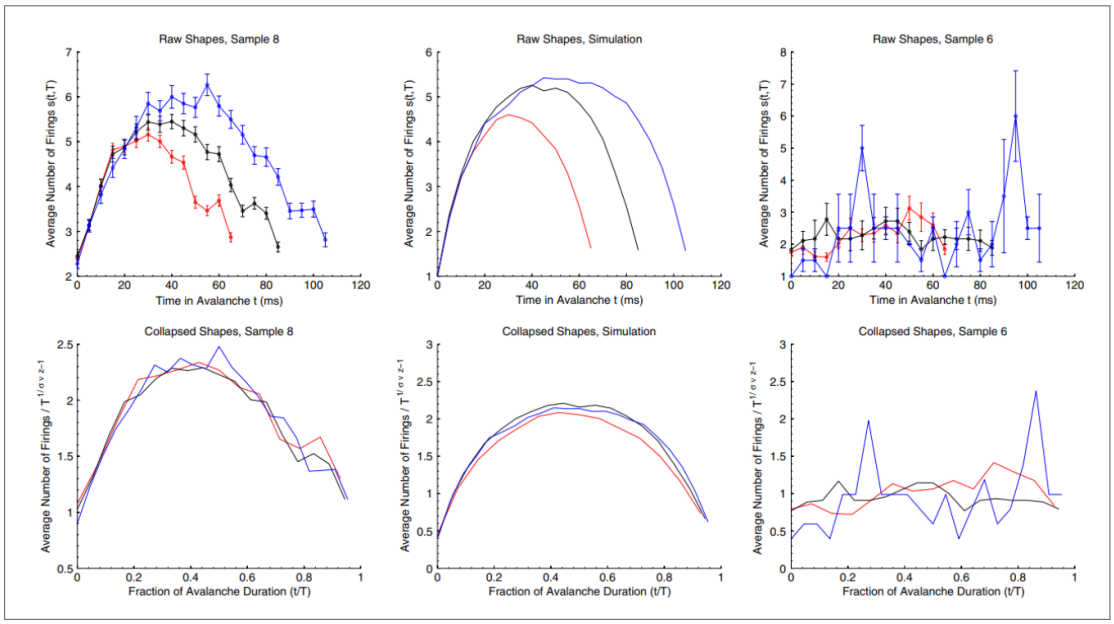

Source: (FRIEDMAN et al., 2012)

2.3.4 Avalanche Dynamics

Considering scaling relations, for MF-DP, the predicted exponents for the avalanches, $P(S) \propto S^{-\tau}$ and $P(T) \propto T^{-\tau_t}$, are:

$$\tau = \frac{1+\eta+2\delta}{1+\eta+\delta} = \frac{3}{2} \tag{2.39}$$

$$\tau_t = 1+\delta = 2. \tag{2.40}$$

Additionally, scaling in the context of avalanches dictates that the average size of avalanches (S) scales with the duration (T) to the power of $\gamma \equiv 1/(\sigma\nu z)$, i.e.,

$$\langle S \rangle \propto T^{\gamma} \, . \tag{2.41}$$

This theory also predicts a shape collapse onto a universal curve ($s(t;T)$; see Fig. 8), the mean temporal profile of the avalanches (FRIEDMAN et al., 2012):

$$s(t;T) \sim T^{\gamma-1}\mathcal{F}(t/T). \tag{2.42}$$

Furthermore, the scaling relation that predicts this exponent is (KUNTZ; SETHNA, 2000; SETHNA; DAHMEN; MYERS, 2001; TOUBOUL; DESTEXHE, 2017; PONCE-ALVAREZ et al., 2018b):

$$\gamma = \frac{\tau_t - 1}{\tau - 1} = 2. \tag{2.43}$$

2.4 TRICRITICAL DIRECTED PERCOLATION

2.4.1 Higher-order Contact Process Model

The modified version of the contact process introduces a higher-order interaction with a second parameter, such that two active sites have a probability q of activating a third site (OHTSUKI; KEYES, 1987),

$$\begin{aligned}
A \to 0 \quad & \text{with probability} \quad (1-q)\,(1-p) \\
0A \to 00 \quad & \text{with probability} \quad q\,(1-p) \\
0A \to AA \quad & \text{with probability} \quad p\,(1-q) \\
AA \to 0A \quad & \text{with probability} \quad (1-q)\,(1-p) \\
0AA \to AAA \quad & \text{with probability} \quad q.
\end{aligned}$$

Observe that the rates τ, g, and c are written as a function of these probabilities: $\tau = 2p - 1$, $g = p - (2 - p)\ q$, and $c = q$. This process is represented by the Langevin equation with a similar format to that of Eq. (2.1),

$$\frac{1}{\alpha}\frac{\partial}{\partial t}\rho = \tau\rho - g\rho^2 - c\rho^3 + \Gamma\nabla^2\rho + h + \eta\ , \tag{2.44}$$

where h represents the external field, ρ is the activity density, and η is a Gaussian noise.

2.4.2 Tricritical Directed Percolation Universality Class

In the mean-field approach, the noise and spatial terms disappear and the mean-field equation becomes,

$$\frac{1}{\alpha}\frac{d}{dt}\rho = \tau\rho - g\rho^2 - c\rho^3 + h\ . \tag{2.45}$$

Considering $h = 0$, the quiescent state is always a fixed point and a linear analysis shows that, for $\tau < 0$, it is unstable and, for $\tau > 0$, it is stable (see Fig. 9). The other static solutions are

$$\bar{\rho} = -\frac{g}{2c} \pm \sqrt{\frac{\tau}{c} + \left(\frac{g}{2c}\right)^2}\ , \tag{2.46}$$

Observe that the negative sign yields a nonphysical solution since ρ is a density. So the positive sign solution shows how the system's density scales with the control parameter τ.

Figure 9 – Mean-field phase diagrams of tricritical directed percolation. On the left, the phase diagram is sketched as a function of the coarse-grained parameters τ and g. On the right, the same phase diagram is sketched as a function of the probabilities p and q. The thick curve along $\tau = 0$ and $g > 0$ (left), or conversely below the tricritical point at $p = 0.5$, are second-order phase transitions belonging to DP. The shadowed areas represent bistability. And the thin dashed lines illustrate the cross-over to tricritical behavior.

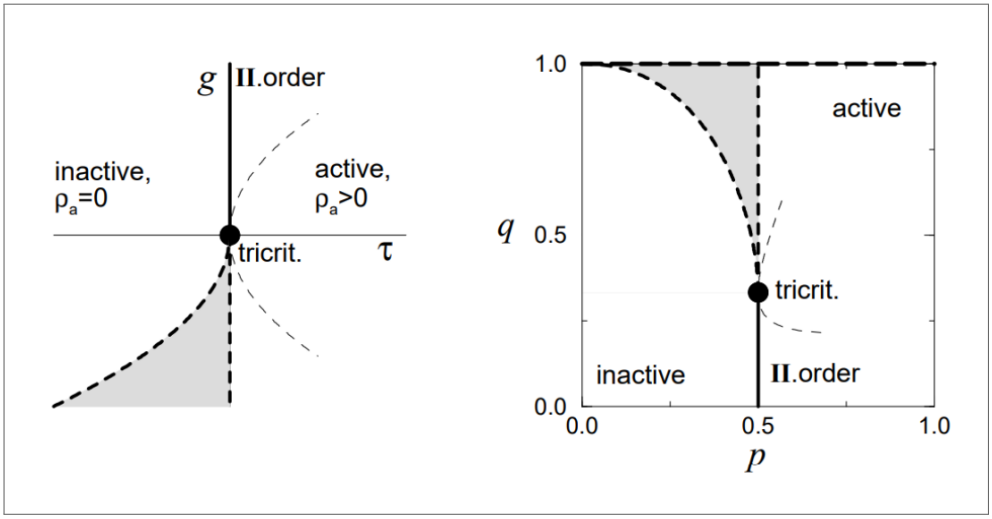

Source: (LÜBECK, 2006)

LÜBECK (2006) studied the model and the tricritical directed percolation in some detail. The tricritical point is a point in the phase diagram of a system where three different phases meet, for this section, this point separates a For the purposes of the search of the tricritical directed percolation, we will focus on $g = 0$, where the system displays tricritical behavior (see left panel of Fig. 9). The β exponent for this solution, $\bar{\rho} = \sqrt{\tau/c}$, is $1/2$. One can easily observe that at $\tau \to 0^+$, with $g > 0$ and $\tau \ll g^2/4c$, results in a DP transition as $\bar{\rho} = \tau/g + \mathcal{O}(\tau^2)$.

The system's behavior with respect to an external field is also extrapolated for $\tau = 0$ and $g = 0$. From Eq. (2.45), the static solution, $\bar{\rho} = (h/c)^{1/3}$, scales with exponent $1/3$, yielding $\delta_h = 3$.

Similarly to what we did with the DP, considering that for this system ($\alpha = 3$), we calculate, above the upper critical dimension ($d_c = 3$): $z = 1$, $\delta = 1$, $\nu_\perp = 1/2$, and $\nu_\parallel = 1$. Observe that the overall exponents are not the same as the directed percolation ones, which is reflected in the expected values for the avalanche distribution exponents, we are going to detail in Chapter 4.

In conclusion, though the tricritical directed percolation universality class has many exponents in common with the directed percolation one, each displays unique features.

2.5 ASYMMETRICALLY COUPLED DIRECTED PERCOLATION

The previous transitions consider one relevant field. However, to represent a broader range of phenomena, one must consider one or more fields coupled. Diving into the systems involving multiple significant fields, we uncover two universality classes that emerge from the coupling of two fields, leading to an absorbing phase: Unidirectionally Coupled Directed Percolation (UCDP) and Asymmetrically Coupled Directed Percolation (ACDP).

2.5.1 Model

NOH; PARK (2005a) uses a model that mimics an epidemic with immunization agents, introducing an “inhibitory" species to the contact process. This model features two coupled species, A and B, both falling within the Directed Percolation (DP) universality class. Species A and B deactivate spontaneously with probabilities p_A and p_B, respectively. Additionally, species A activates species B with probability $(1 - p_A)\lambda$, while it activates another A site with the complementary probability. Species B activates other instances of itself with a probability

of $(1-p_B)$ and deactivates species A with probability μ (See Fig 10). Notably, when $\mu = 0$, the "inhibitory" species B, loses its inhibitory abilities and the system falls into the Unidirectionally Coupled Directed Percolation (UCDP) universality class. These transitions are summarized as follows,

$$
\begin{aligned}
A/B \to 0 \quad & \text{with probability} \quad p_{A/B} \\
A \to AA \quad & \text{with probability} \quad (1-p_A)(1-\lambda) \\
B \to BB \quad & \text{with probability} \quad 1-p_B \\
A \to AB \quad & \text{with probability} \quad (1-p_A)\lambda \\
AB \to B \quad & \text{with probability} \quad \mu\ .
\end{aligned}
$$

Figure 10 – Schematics of rates of the ACDP model. The circles represent species A and are filled in when active and empty when inactive. The squares represent the B species.

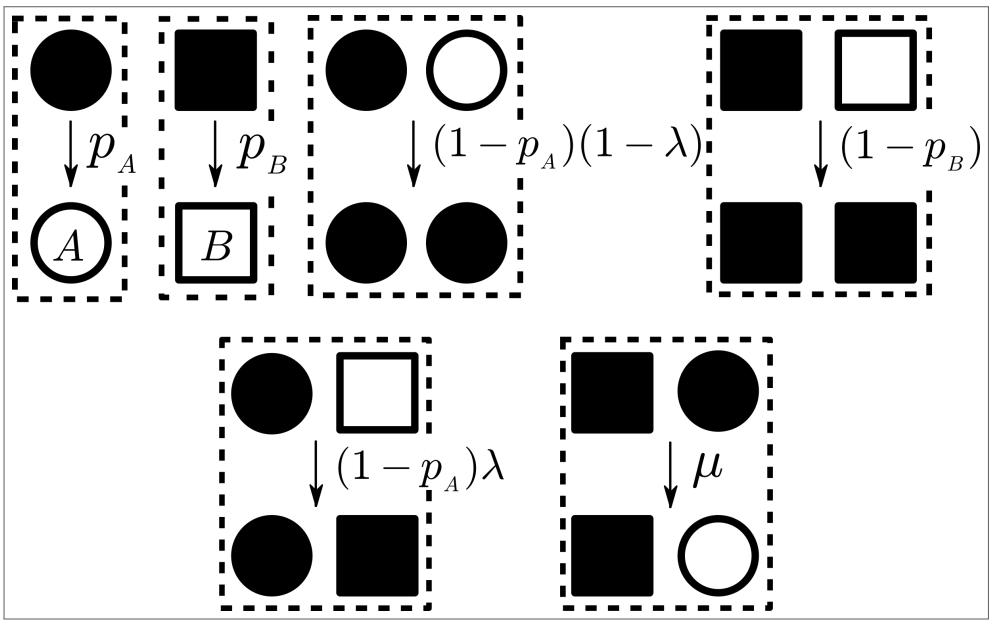

Source: The author (2023)

2.5.2 Mean-Field equations

For this model, one needs to build two mean-field equations, where the two species closely resemble the contact process with added terms to represent the coupling. The mean-field

equations are easily written as:

$$\begin{aligned}
\frac{d}{dt}\rho_A &= -p_A\rho_A - \mu\rho_A\rho_B + (1-p_A)(1-\lambda)\rho_A(1-\rho_A) \\
&= -p_A\rho_A - \mu\rho_A\rho_B + (1-p_A)(1-\lambda)(\rho_A - \rho_A^2) \\
&= \left[(1-p_A)(1-\lambda) - p_A\right]\rho_A - (1-p_A)(1-\lambda)\rho_A^2 - \mu\rho_A\rho_B \ , \qquad (2.47) \\
\frac{d}{dt}\rho_B &= -p_B\rho_B + \lambda(1-p_A)(1-\rho_B)\rho_A + (1-p_B)\rho_B(1-\rho_B) \\
&= (1-2p_B)\rho_B - (1-p_B)\rho_B^2 + \lambda(1-p_A)\rho_A \ , \qquad (2.48)
\end{aligned}$$

where ρ_i is the density of active sites of the species i. To make these equations more palatable, we can rename the parameters: the first equation can be rewritten only in terms of $\alpha_A = (1-p_A)(1-\lambda)$ and the second in terms of $\alpha_B = 1 - p_B$. The behavior of the system must remain unchanged, and the equations become:

$$\begin{aligned}
\frac{d}{d(\alpha_A t)}\rho_A &= a_A\rho_A - \rho_A^2 - \tilde{\mu}\rho_A\rho_B \ , \qquad (2.49) \\
\frac{d}{d(\alpha_B t)}\rho_B &= a_B\rho_B - \rho_B^2 + \tilde{\lambda}\rho_A \ , \qquad (2.50)
\end{aligned}$$

where $a_A = \left[(1-p_A)(1-\lambda) - p_A\right]/\alpha_A$, $\tilde{\mu} = \mu/\alpha_A$, $a_B = (1-2p_B)/\alpha_B$, and $\tilde{\lambda} = \lambda(1-p_A)/\alpha_B$. It is noteworthy that, for $\mu = 0$, the UCDP universality class, the only visible coupling is excitatory to species B.

2.5.3 Phase Space and Transitions

Similarly to the previous models, the quiescent state is always a fixed point of the mean-field equation. In this case, we can write the static solutions as:

$$\begin{aligned}
\bar{\rho}_A &= \frac{1}{\tilde{\lambda}}\left(\bar{\rho}_B^2 - a_B\bar{\rho}_B\right) \ , \qquad (2.51) \\
\frac{1}{\tilde{\lambda}\tilde{\mu}}\bar{\rho}_B^2 &+ \left(1 - \frac{a_B}{\tilde{\lambda}\tilde{\mu}}\right)\bar{\rho}_B - \frac{a_A}{\tilde{\mu}} = 0 \ , \qquad (2.52)
\end{aligned}$$

resulting in the same structure we have seen for DP and TDP. This indicates that, for a unique set of parameters, each species goes through a quiescent to active transition.

NOH; PARK (2005a) defined three phases: the I label represents a complete quiescent phase, where both species relax to quiescence; the II label represents a hybrid phase, where species A is quiescent and species B is active; and the III label represents a complete active phase, where both species are active. The transitions are shown in Fig. 11 in the form of line segments.

Figure 11 – Schematic phase diagram of the asymmetrically coupled directed percolation for fixed λ and μ.

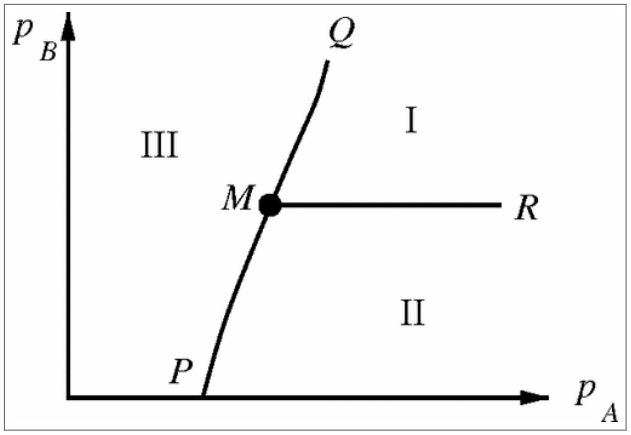

Source: (NOH; PARK, 2005a)

The segment $\bar{MR}$ shows a transition from phase I to II, a quiescent to active phase transition for species B (belonging to DP); $\bar{MQ}$ shows a transition from phase I to III, both species go through a quiescent to active transition (belonging to DP); $\bar{MP}$ shows a transition from phase II to III, species A goes through a quiescent to active transition (belonging to DP); and M is a multicritical Point.

2.5.4 Multicritical Point

The mean-field equations clearly indicate a shift in behavior when both $a_A = 0$ and $a_B = 0$. Now let us approach the multicritical point, considering Δ a distance to the critical point for A, we can write the condition to approach the tricritical point as $(a_A, a_B) = (\Delta, r\Delta)$. In the limit $\Delta \to 0$, the equations

$$(\Delta - \rho_A)\rho_a - \tilde{\mu}\rho_A\rho_B = 0 \tag{2.53}$$

$$(r\Delta - \rho_B)\rho_B + \tilde{\lambda}\rho_A = 0 \tag{2.54}$$

$$[\rho_A] \propto [\rho_B]^2 \propto \Delta^2 \quad \text{, if } \tilde{\mu} \neq 0 \tag{2.55}$$

$$[\rho_A] \propto [\rho_B]^2 \propto \Delta \quad \text{, otherwise;} \tag{2.56}$$

yield the exponents for the two species, $\beta_A = 2$ and $\beta_B = 1$; therefore, for the ACDP universality class, and $\beta_A = 1$ and $\beta_B = 1/2$, for the UCDP universality class.

Introducing spatial fluctuation in terms of $\nabla^2\rho_{A/B}$ (like in Sec 2.2), they also behave as powerlaws, with exponents $\nu_{A\perp} = \nu_{B\perp} = 1/2$ and the spreading exponents, $\delta = 0$ and $z = 1$.

The interesting feature of this universality class is the time decay. On the multicritical

Table 1 – Summary of mean-field exponents

	β	δ_h	θ	δ	$\nu_\parallel$	$\nu_\perp$	τ	τ_t	γ
DP	1	2	1	1	1	$1/2$	$3/2$	2	2
TDP	$1/2$	3	$1/2$	1	1	$1/2$	-	-	-
ACDP	1	2	$\max\{2, \tilde{\mu}\}$	1	1	$1/2$	-	-	-

Source: Compiled by the author (2023) from referenced data in (MUÑOZ et al., 1999), (LÜBECK, 2006), and (NOH; PARK, 2005a)

point, species B falls into the same scaling as DP with $\theta_B = 1$. However, the time decay scaling for species A depends on $\tilde{\mu}$. In order to calculate the time exponents, we use the ansatz, $\rho_A(t) = At^{\theta_A}$ and $\rho_B(t) = Bt^{\theta_B}$, and obtain

$$-\theta_A A t^{-\theta_A - 1} = -A^2 t^{-2\theta_A} - \tilde{\mu} AB t^{-\theta_A - \theta_B} , \tag{2.57}$$

$$-\theta_B B t^{-\theta_B - 1} = -B^2 t^{-2\theta_B} + \tilde{\lambda} A t^{-\theta_A} . \tag{2.58}$$

Isolating θ_A and θ_B on the left-hand side of the equations, respectively, and considering $\theta_A > 2$ yields $\theta_B = B = 1$; thus,

$$\theta_A = A t^{-\theta_A + 1} + \tilde{\mu} , \tag{2.59}$$

$$\theta_A|_{t\to\infty} = \tilde{\mu} . \tag{2.60}$$

Conversely, when $\tilde{\mu} < 2$, so that $\theta_A \leq 2$, θ_B remains unchanged and $\theta_A = 2$. In conclusion,

$$\theta_A = \max\{2, \tilde{\mu}\}, \tag{2.61}$$

albeit at $\tilde{\mu}$, we need logarithm corrections to better explain the behavior. These mean-field exponents are summarized in table 1.

3 WILSON-COWAN MODEL

The Wilson-Cowan model has been able to reproduce many phenomena observed in spontaneous brain activity including complex spatial-temporal patterns and avalanche dynamics (WALLACE et al., 2011; MARUYAMA; KAKIMOTO; ARAKI, 2014; COWAN; NEUMAN; DRONGELEN, 2016; CANDIA et al., 2021). Several papers and books describe the Wilson-Cowan equations, including a thorough analysis of the possible bifurcations. These equations are used in computational neuroscience to study how large groups of neurons interact and generate patterns of activity. Jack Cowan himself has produced a long list of papers studying the model in its "mean-field" dynamic form (WILSON; COWAN, 1972; WILSON; COWAN, 1973) and in its stochastic counterpart (BUICE; COWAN, 2007; BENAYOUN et al., 2010).

The analysis of avalanche distribution and their dynamics have gained growing popularity as a means of comparison with experimental data, where the distributions of avalanche size and duration follow power laws and are consistent with the branching process. In what follows, we will summarize the origin of the model, the possible bifurcations and phase plane analysis, and two interpretations of the mechanism underlining the avalanche behavior of its stochastic version.

3.1 WILSON-COWAN DYNAMICS (1972)

Wilson and Cowan introduced dynamical equations that, rather than modeling individual neurons, model a localized neural population composed of excitatory and inhibitory subpopulations (WILSON; COWAN, 1972; WILSON; COWAN, 1973). They readdressed the work on excitatory populations of neurons (BEURLE, 1956; HOOPEN, 1966) adding an inhibitory subpopulation. The model considered excitatory and inhibitory firing proportions in an instant t, $E(t)$, and $I(t)$, respectively.

Considering a set of N McCulloch-Pitts neurons (MCCULLOCH; PITTS, 1943) – a neural network model with a single layer – and a Poisson input (the timing and frequency of action potentials or spikes are described by a Poisson distribution), the authors formulate a dynamical process in the form of two differential equations. Pitts neurons take a weighted sum of binary inputs and produce binary outputs: when the sum of inputs is equal to or larger than a threshold (θ), the output is 1; otherwise, it is 0. Therefore, WILSON; COWAN (1972) now solve a first

Figure 12 – Typical sigmoid response function. (a) logistic function. (b) In principle, the response function could also stem from a bimodal distribution of threshold, which would take the following format. However, observe that the function keeps being monotonic and bounded by 0 and 1.

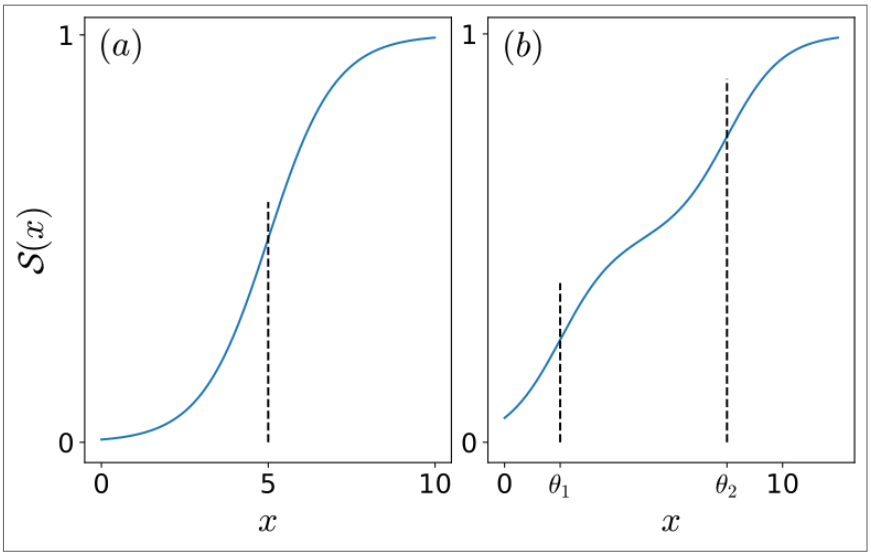

Source: Adapted from (WILSON; COWAN, 1972)

passage problem: how long, on average, does it take for each neuron to fire with a Poisson input?

The function that indicates the expected proportion of excitation given the state of the network is a *response function*. The authors considered two ways of studying this proportion function in a large-scale network that is well-connected: (1) First, all cells have a distribution of thresholds with the same number of afferent synapses; and (2) all cells have a distribution of afferent synapses with same threshold. To accommodate both assumptions, the response function was deemed monotonic with a lower bound of zero and an upper bound of 1. Therefore, the step function becomes an integral of the probability density function, which will look like a logistic function (COWAN, 1968) (see Fig 12a),

$$\mathcal{S}(x) = \{1 + \exp[-ax]\}^{-1}. \tag{3.1}$$

In 1972, Wilson and Cowan published the dynamics of these populations considering the activity of each subpopulation at time $(t+\tau)$ and time coarse-graining it. The authors proposed that the proportion of active neurons after a time step τ can be expressed by:

$$E(t+\tau) = \left[1 - \int_{t-\tau}^{t} E(t')dt'\right] \mathcal{S}\left\{\int_{-\infty}^{t} \alpha(t-t')[w'_{EE}E(t') - w'_{EI}I(t') + h_E(t')]dt'\right\}, \tag{3.2}$$

$$I(t+\tau) = \left[1 - \int_{t-\tau}^{t} I(t')dt'\right] \mathcal{S}\left\{\int_{-\infty}^{t} \alpha(t-t')[w'_{IE}E(t') - w'_{II}I(t') + h_I(t')]dt'\right\}, \tag{3.3}$$

where $E(t)$ and $I(t)$ are the proportion of active excitatory and inhibitory cells per unit time at instant t, respectively; τ is the membrane time constant; h_x, where $x \in \{E, I\}$, represents

the sum of external input; w_{xy} are the synaptic weights; and $\alpha(t)$ is the stimulation effect decay for a period of time. The first term of the multiplication represents the proportion of quiescent neurons in the subpopulation and, inside the response function on the second term, the average instantaneous excitation generated in a cell of each subpopulation. Observe that a portion of the quiescent neurons could be considered to be refractory and, therefore, not sensitive to firing. For the purposes of the article, the network is considered a *richly interconnected population of cells* (WILSON; COWAN, 1972).

Nonlinearities are expected in biological systems. And to sidestep the time integrals, WILSON; COWAN (1972) use an *average* variable to disregard rapid temporal variations. Furthermore, considering that $\alpha(t) \approx 1$ for $0 \geq t \geq r$, the integral $\int \alpha(t-t')E(t')dt'$ is proportional to an average of $E(t)$. Thus, the dynamics for a spatially homogenous population of excitatory and inhibitory neurons is (WILSON; COWAN, 1972):

$$\tau \frac{d}{dt}\bar{E}(t) = -\bar{E}(t) + [1 - r\ \bar{E}(t)]\ S\left[w_{EE}\ \bar{E}(t) - w_{EI}\ \bar{I}(t) + h_E(t)\right], \tag{3.4}$$

$$\tau \frac{d}{dt}\bar{I}(t) = -\bar{I}(t) + [1 - r\ \bar{I}(t)]\ S\left[w_{IE}\ \bar{E}(t) - w_{II}\ \bar{I}(t) + h_I(t)\right], \tag{3.5}$$

where r is the mean refractory period and $\bar{E}(t)$ and $\bar{I}(t)$ represent the average of each quantity.

The Wilson-Cowan model is a simplified representation of neural dynamics and provides insights into phenomena such as neural oscillations and the emergence of complex patterns of neural activity. The equations capture the balance between excitation and inhibition within the population and can exhibit various patterns of neural activity, including stable fixed points, limit cycles (oscillations), and chaotic behavior, depending on the parameters and initial conditions.

3.1.1 Bifurcations

The seminal work of Hoppensteadt and Izhikevich summarized the bifurcations using as parameters the value of the external fields – i.e., in Eq. 3.4, h_E and, in Eq. 3.5, h_I (IZHIKEVICH, 2007; HOPPENSTEADT; IZHIKEVICH, 1997). IZHIKEVICH (2007) considers the Wilson-Cowan dynamics in the case where the refractory period is zero ($r = 0$), i.e.,

$$\tau \frac{d}{dt}E(t) = -E(t) + S\left[w_{EE}\ E(t) - w_{EI}\ I(t) + h_E(t)\right], \tag{3.6}$$

$$\tau \frac{d}{dt}I(t) = -I(t) + S\left[w_{IE}\ E(t) - w_{II}\ I(t) + h_I(t)\right]. \tag{3.7}$$

Observe that from here on we will be suppressing the bar for the average quantities for simplicity.

The analysis of the equilibria should, at first, consider the existence of the inverse of $\mathcal{S}(x)$. When true, we can express the external fields at the solutions (E^*, I^*) for $dE/dt = 0$ and $dI/dt = 0$ as

$$h_E = w_{EI}I^* - w_{EE}E^* + \mathcal{S}^{-1}(E^*) , \tag{3.8}$$

$$h_I = w_{II}I^* - w_{IE}E^* + \mathcal{S}^{-1}(I^*) , \tag{3.9}$$

and the derivative of the response function follows $dS(x)/dx = S(1-S)$. The Eq. (3.1) fits these conditions and is the choice of response function throughout this section. Therefore, the Jacobian matrix takes the form:

$$J = \begin{pmatrix} -1 + w_{EE}\, E^*(1-E^*) & -w_{EI}\, E^*(1-E^*) \\ -w_{IE}\, I^*(1-I^*) & -1 - w_{II}\, I^*(1-I^*) \end{pmatrix} . \tag{3.10}$$

For the linear stability analysis, the eigenvalues can be expressed as

$$2\lambda = Tr(J) \pm \sqrt{[Tr(J)]^2 - 2Det(J)} , \tag{3.11}$$

where $Tr(J)$ is the trace of J and $Det(J)$ is the determinant of J. The equilibria are foci when the eigenvalues are complex, which are stable when the real part of the eigenvalue is

Figure 13 – Set of bifurcations of Wilson-Cowan neuron oscillator model for $w_{EE} = w_{IE} = w_{EI} = 10$ and $w_{II} = -2$. The Hopf bifurcations, Cusp, and Bogdanov-Takens are indicated; and the saddle-node bifurcation curves are represented by the thickest lines.

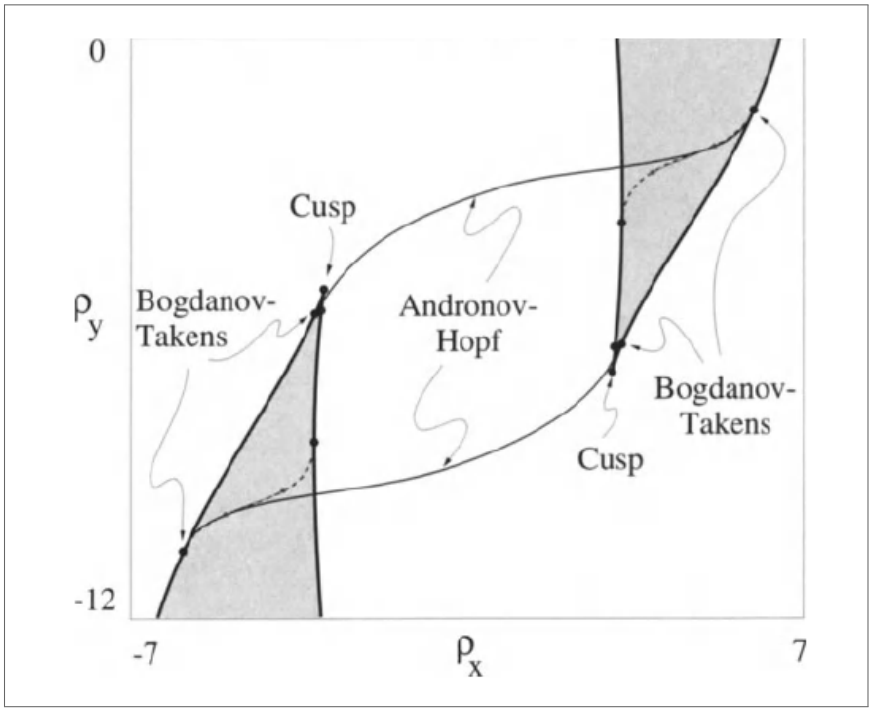

Source: (IZHIKEVICH, 2007)

negative and unstable when it is positive. The supercritical Hopf bifurcation, where the stable focus loses its stability to a limit cycle, occurs at $Tr(J) = 0$ and $Det(J) > 0$ (see indicated lines in Fig. 13).

Figure 14 – Detailed visualization of the bifurcations in Fig. 13. The bifurcations are: Cusp (C), supercritical Hopf (AH), Bogdanov-Takens (BT), fold limit cycle (double limit cycle), Homoclinic bifurcation (SSL), subcritical Hopf (SAH), saddle-node (SN), saddle-node on a limit cycle (SNLC), and saddle-node separatrix loop (SNSL). Observe that the homoclinic and fold limit cycle bifurcations are distorted for clarity.

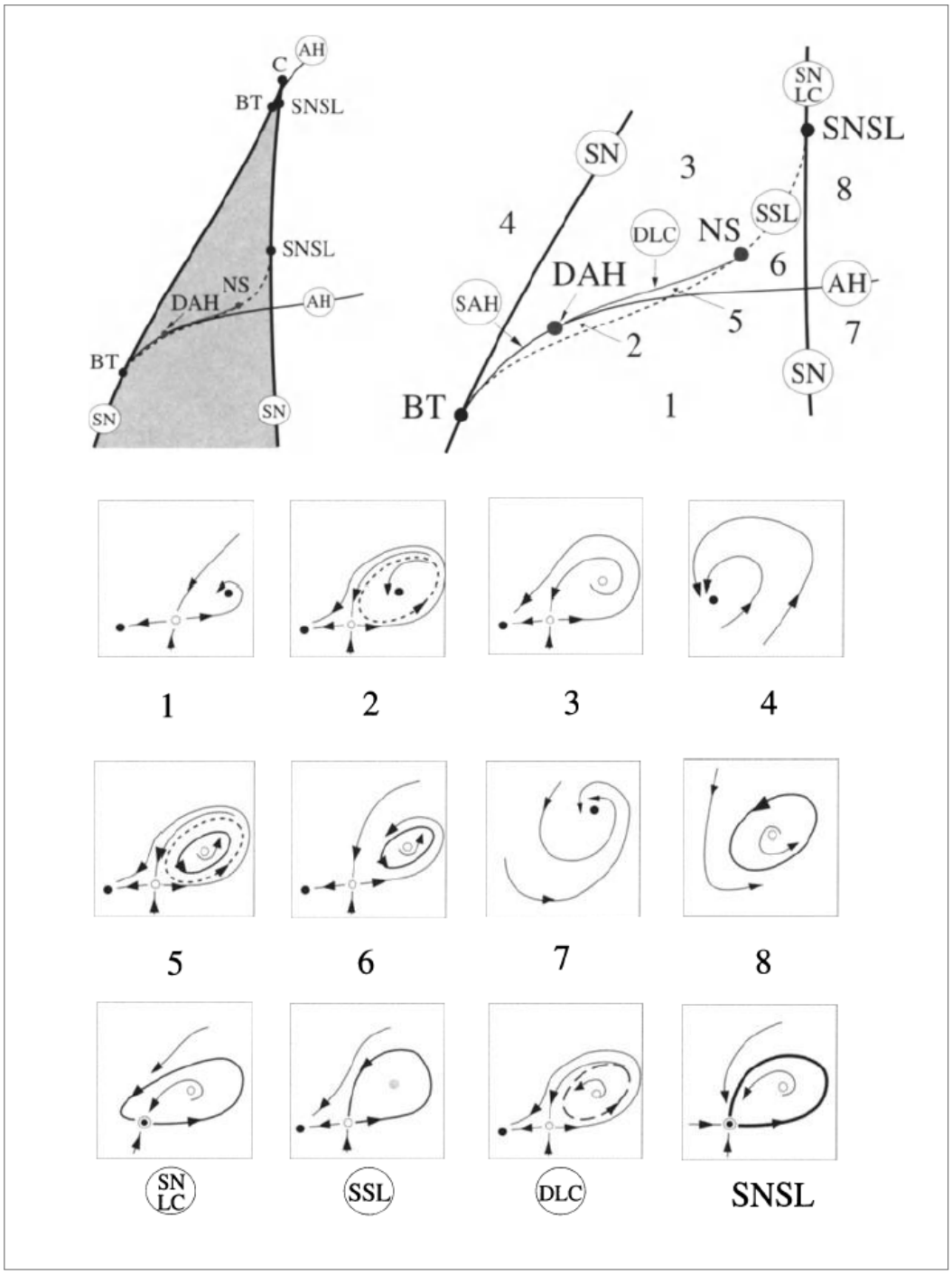

Source: (IZHIKEVICH, 2007)

The other codimension-1 local bifurcation is the saddle-node (see thicker lines in Fig. 13). The saddle-node, as the name suggests, is a bifurcation where a stable node becomes a saddle. The condition for this bifurcation is $Det(J) = 0$. The Hopf and saddle-node bifurcations collide in a Bogdanov-Takens (BT), which is a codimension-2 bifurcation. At the BT bifurcation, both eigenvalues are zero and the normal form of the Jacobian has only one non-zero off-diagonal entry. The second codimension-2 bifurcation is the Cusp (or Cusp-catastrophe) and it occurs in the vicinity of saddle-node bifurcations forming a singularity. Both types of codimension-2 bifurcations are indicated by name in Fig. 13.

Global behaviors fail to appear in the linear analysis. For these equations, the saddle separatrix loop (dashed line in Fig. 14) is also known as a homoclinic bifurcation, where a saddle collides with a homoclinic cycle. The indicated double-limit cycle bifurcation in Fig. 14 is also called a fold limit cycle bifurcation. It represents when two limit cycles, one stable and one unstable, coalesce. A detailed visualization of the set of bifurcations is shown in Fig. 14.

3.2 STOCHASTIC MODEL

Expanding upon the deterministic Wilson-Cowan equations, BENAYOUN et al. (2010) derived from the more general stochastic rate (microscopic) model (BUICE; COWAN, 2007) the so-called *Stochastic Wilson-Cowan* model (SWC). The SWC model was built to be a stochastic perturbation of the Wilson-Cowan equations and takes the form of a Markovian process for a population of coupled excitatory and inhibitory individual binary neurons.

Each neuron can be either active or quiescent and its state at a given instant t depends on the transition rates: (1) α, spontaneous decay– i.e., transitioning from active to quiescent; and

Figure 15 – a) A diagram of the transition of the $i-th$ neuron, where s_i is the total synaptic input. b) Response function: $\Phi(s) = \tanh(s)H(s)$, where $H(s)$ is the Heaviside, or step, function.

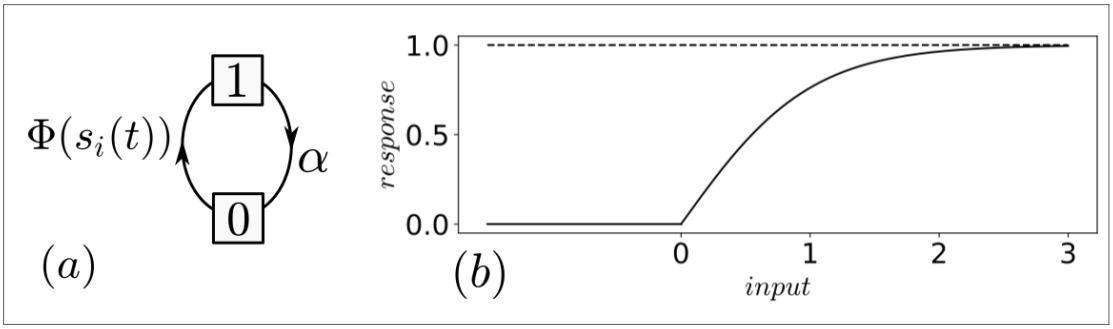

Source: Adapted from (BENAYOUN et al., 2010)

(2) $\Phi(s_i(t))$, driven activation – i.e., transition from quiescent to active. Note that, for this model, the refractory period is absent, the neuron is either not sensitive to the input (active) or sensitive to it (inactive), and the decay rate α serves as a time constant to regulate this built-in refractory period.

The response function takes a different shape from the one introduced in the original model (see Sec. 3.1). However, it remains bound by $[0, 1)$ because of the introduction of the Heaviside function, which ensures non-negativity. Furthermore, this response function does not allow any negative values of E and I, that were considered when developing the dynamical equations as being activity below the low-level background activity. Considering that the state of each neuron ℓ, regardless of type, is given by $\sigma_\ell^{E/I}(t) = 1$ when active and $\sigma_\ell^{E/I}(t) = 0$ when inactive, we write the response function as

$$\Phi(s^\ell) \;=\; \begin{cases} \tanh(s^\ell), & \text{if } s^\ell > 0 \\ 0, & \text{otherwise,} \end{cases} \tag{3.12}$$

where the *input* s^ℓ to neuron, ℓ is

$$s^\ell \;=\; \sum_m w^{\ell m}\sigma_m + h, \tag{3.13}$$

$w^{\ell m}$ is the synaptic weight from neuron m to neuron ℓ, and h is a constant external input.

The network has all-to-all homogeneous connectivity, whose synaptic weights depend only on the type (excitatory or inhibitory) of both the pre-synaptic and the post-synaptic neuron

Figure 16 – A) Schematic of connection strengths between excitatory, E, and inhibitory, I, populations. B) Schematic of functionally feedforward connectivity, observe that the connecting arrow is unidirectional from Δ to Σ.

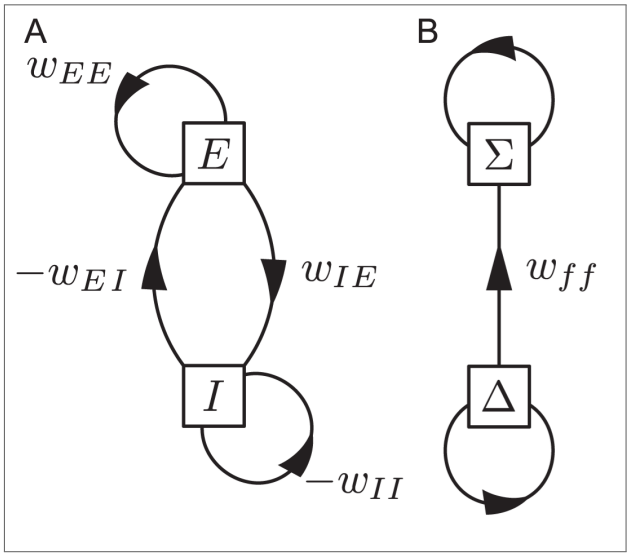

Source: Adapted from (BENAYOUN et al., 2010)

(see Fig. 16A). The evolution of a network of size N can be regarded as a random walk between the states with k excitatory and l inhibitory active neurons. Considering a Gaussian approximation, where the neurons are assumed to fire independently, the overall dynamics can be segmented into two terms: a deterministic and stochastic perturbation (OHIRA; COWAN, 1997; KAMPEN, 2007; BENAYOUN et al., 2010; CANDIA et al., 2021). The perturbation takes the form $\sqrt{N}\xi_{E/I}$ and the deterministic part is proportional to the size of the system; therefore, the stochastic variables are reduced to $k = NE + \sqrt{N}\xi_E$ and $l = NI + \sqrt{N}\xi_I$. The temporal evolution of these stochastic variables is depicted by the Langevin equations:

$$\begin{aligned} \dot{k} &= -\alpha k + (N-k)\,\Phi\left(w_{EE}E - w_{EI}I + h\right) + \\ &\quad + \sqrt{\alpha k + (N-k)\,\Phi\left(w_{EE}E - w_{EI}I + h\right)}\;\eta_E(t), \qquad (3.14) \\ \dot{l} &= -\alpha l + (N-l)\,\Phi\left(w_{EE}E - w_{EI}I + h\right) + \\ &\quad + \sqrt{\alpha l + (N-l)\,\Phi\left(w_{IE}E - w_{II}I + h\right)}\;\eta_I(t)\;, \qquad (3.15) \end{aligned}$$

where $E(t)$ and $I(t)$ are the densities of active excitatory and inhibitory neurons, respectively, and follow the Wilson-Cowan equations (Eq. (3.4) and Eq. (3.5)); and the noises are Gaussian, $\langle \eta_i(t) \rangle = 0$ and $\langle \eta_i(t)\eta_j(t') \rangle = \delta_{ij}\delta(t-t')$.

To reduce the dimensionality of the phase diagram, the model has the same external field, $h \equiv h_E = h_I$, and symmetric weights – i.e., common excitatory ($w_E \equiv w_{EE} = w_{IE}$) and inhibitory ($w_I \equiv w_{II} = w_{EI}$) inputs – a relative routine practice in the literature (BRUNEL, 2000a; BENAYOUN et al., 2010; CANDIA et al., 2021). This dimensionality reduction results in a symmetric input, which means the argument of $\Phi(s)$ is the same for both equations, $s = w_E E - w_I I + h$. Therefore, a new set of variables is introduced to describe this model: $\Sigma = (E+I)/2$ and $\Delta = (E-I)/2$, which leads to $s = w_0\Sigma + w_+\Delta + h$ — where $w_0 = w_E - w_I$ and $w_+ = w_E + w_I$. The feedforward dynamics also display deterministic and stochastic time evolution terms, the deterministic ones are

$$\begin{aligned} \dot{\Sigma} &= -\alpha\,\Sigma + (1-\Sigma)\,\Phi(s)\;, \qquad (3.16) \\ \dot{\Delta} &= -[\,\alpha + \Phi(s)\,]\,\Delta\;, \qquad (3.17) \end{aligned}$$

with static solution $(\Sigma_0, 0)$. The difference field (Δ) relaxes quickly to zero and the sum field (Σ) relaxes to $\alpha\Sigma_0 = (1-\Sigma_0)\,\Phi(w_0\Sigma_0 + h)$.

Now, analyzing the dynamics of the perturbation, the terms that are proportional to $\sqrt{N}$

follow linearized Langevin equations

$$\frac{d}{dt}\begin{pmatrix}\xi_\Sigma\\ \\ \xi_\Delta\end{pmatrix} = \begin{pmatrix}-\lambda_1 & w_{ff}\\ \\ 0 & -\lambda_2\end{pmatrix}\begin{pmatrix}\xi_\Sigma\\ \\ \xi_\Delta\end{pmatrix} + \sqrt{\alpha\Sigma_0}\begin{pmatrix}\eta_\Sigma(t)\\ \\ \eta_\Delta(t)\end{pmatrix}, \tag{3.18}$$

where η_ℓ are independent white-noise variables, the eigenvalues $\lambda_1 \equiv 1/\tau_1 = \alpha + \Phi(w_0\Sigma_0 + h) - (1-\Sigma_0)\ w_0\ \Phi'(w_0\Sigma_0 + h)$ and $\lambda_2 \equiv 1/\tau_2 = \alpha + \Phi(w_0\Sigma_0 + h)$ represent the inverse of the relaxation times (τ_1, τ_2), and the off-diagonal element w_{ff} is called a feedforward term (see Fig. 16B), because the dynamics of Δ affects the dynamics of Σ but not the other way around (BENAYOUN et al., 2010; CANDIA et al., 2021).

3.2.1 Directed Percolation

Considering Eq. (3.16) and Eq. (3.17) in the absence of an external field, $h = 0$, the quiescent state, $(0, 0)$, becomes the stable solution of the dynamic system. Expanding the solution $\alpha\Sigma_0 = (1-\Sigma_0)\ \Phi(w_0\Sigma_0 + h)$ around $\Sigma_0 = 0$, one obtains the critical value of the effective coupling, $w_{0c} = \alpha$. In the supercritical regime — i.e., at $w_0 > w_{0c}$ (where excitation dominates) – a positive stable fixed point $\Sigma_0 \propto (W_0 - W_{0c})/W_0$ arises continuously, classifying the transition as a second-order phase transition.

Instead of using the variable Σ_0 as the order parameter, CANDIA et al. (2021) chose to focus on the instantaneous firing rate,

$$R \ = \ \left(1 - \frac{k+l}{2N}\right)\Phi(s). \tag{3.19}$$

The firing rate at the stable state $(\Sigma_0, 0)$ has the value $R_0 = (1-\Sigma_0)\Phi(w_0\Sigma_0 + h)$, which grows linearly with the control parameter (w_0) close to the transition, i.e., for $w_0 \to w_{0c}$ (see Fig. 17A).

For a large network $(N \to \infty)$, the variance of the firing rate decays as $\langle (R - R_0)^2 \rangle = N^{-1}\langle \xi_R(0)^2 \rangle$ and, thus, the normalized variance $\sigma_{RR} = N\langle (R - R_0)^2 \rangle$ is independent of the size of the system. Due to the type of transition, the variance should diverge, which it does not, as seen in Fig. 17B. CANDIA et al. (2021) attribute such behavior to the choice of the activation function, where the stable state Σ_0 is zero leading to vanishing noise amplitude at the transition. However, both the Fano factor, σ_{RR}/R_0, and the squared coefficient of variation, σ_{RR}/R_0^2, diverge (see Fig. 17C,D). These phenomena separate the system from a Poissonian variable and confirm that the fluctuations are much larger than the average firing rate, at $w_0 = w_{0c}$ in the parameter space.

Figure 17 – Different observable quantities as a function of the control parameter w_0: A) order parameter R_0, for different values of the external field; B) normalized variance, $\sigma_{RR} = N\langle(R - R_0)^2\rangle$; C) Fano factor, σ_{RR}/R_0; and, D) square coefficient of variation σ_{RR}/R_0^2. The fixed parameters are $\alpha = 0.1$ and $w_E + w_I = 13.8$.

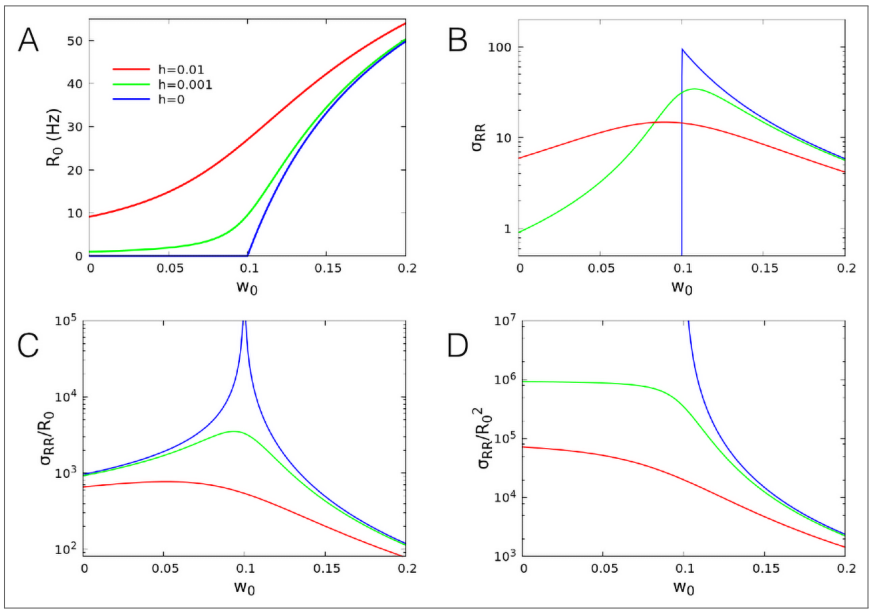

Source: (CANDIA et al., 2021)

The behavior of the system, thus far, provides some indication that the system has a bonafide critical point at $w_0 = w_{0c}$. For a second-order phase transition, the avalanche analysis of the system yields a power-law distribution of sizes and durations. To confirm this phenomenon in the present model, the temporal signal was divided into bins of width δ, the avalanche began at a time bin with at least one spike and was over at a subsequent empty bin. The exponents in the large avalanche regime are robust with bin width, independent of the value of δ. For sizes, they found $P(S) \sim S^{-3/2}$ (Fig. 18A) and, for durations, $P(T) \sim T^{-2}$ (Fig. 18B).

Figure 18 – A) Distribution of avalanche sizes at an area of robust power-law behavior. B) Distribution of avalanche durations in relation to time. Observe that the analysis shows different values of the time bins. The parameters for this analysis were $w_0 = 0.1$, $h = 10^{-6}$, and $N = 10^6$.

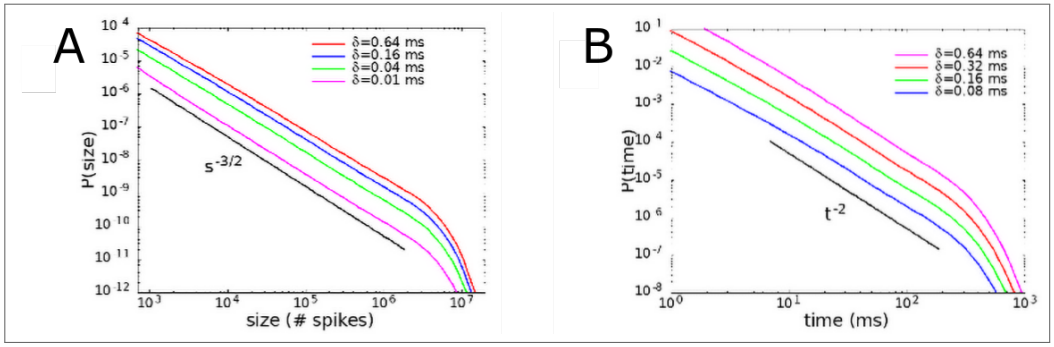

Source: Adapted from (CANDIA et al., 2021)

Another characteristic of critical systems is that the mean temporal profile of the avalanches (avalanche shapes) is universal across all scales and follows

$$s(t,T) \propto T^{\gamma-1}\mathcal{F}(t/T)\ , \tag{3.20}$$

where γ is the crackling noise exponent, which governs the mean avalanche size as a function of its duration. As calculated in Sec. 2.2, these exponent relates to the avalanche distribution as

$$\gamma = \frac{2-1}{3/2-1} = 2. \tag{3.21}$$

CANDIA et al. (2021) calculates $\gamma \sim 2.02 \pm 0.05$ over the interval $T \in [80, 200]$ and observes an asymmetrical shape collapse (see Fig. 19), contrary to what was expected from the work of FRIEDMAN et al. (2012) with a model belonging to the mean-field directed percolation universality class and experimental data. This odd behavior is not fully explored in this paper. Further clarification comes from our analysis in the following chapter, and some are provided in LÓPEZ; BUENDÍA; MUÑOZ (2022).

Figure 19 – A) Scaling of the mean size of avalanches S for a duration T. B) Collapse of the mean temporal profile for different durations. The network had 20% inhibitory neurons with the parameters $w_0 = 0.1$, $h = 10^{-6}$, and $N = 10^7$.

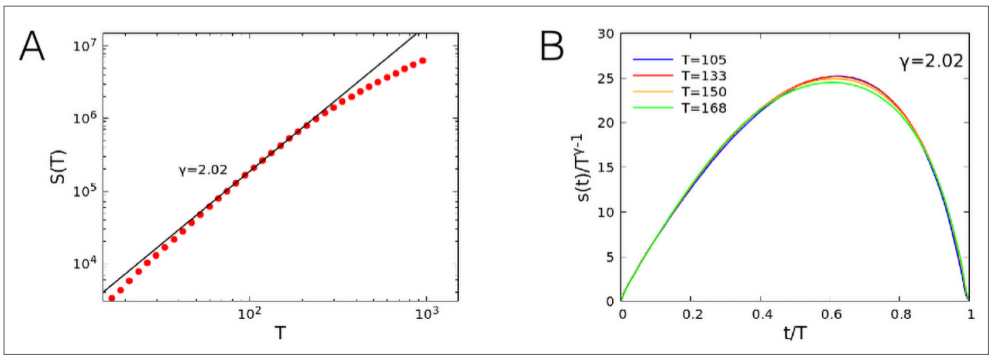

Source: Adapted from (CANDIA et al., 2021)

Therefore, the Wilson-Cowan model is able to reproduce not only oscillations and limit cycles seen in neuronal activity but also critical behavior at a tunable parameter for vanishing external fields belonging to the mean-field directed percolation universality class.

3.2.2 Noncritical Avalanches

As a counterpoint to the avalanche distribution due to a second-order phase transition, BENAYOUN et al. (2010) showed that in a smaller-sized system, the stochastic Wilson-Cowan

model produced avalanches as a consequence of a balanced network of excitatory and inhibitory neurons and small random fluctuations.

Starting at all-to-all connectivity, they show that the network transitions from having asynchronous firing to showing avalanche behavior. Not only does this transition from asynchrony yields to the emergence of avalanches but the sizes of these avalanches are distributed as a power-law with exponent $\beta = 1.62$ (see Fig. 20). These avalanches are a direct result of the feedforward dynamics coupled with the stochastic behavior of the network.

The avalanche behavior shown in BENAYOUN et al. (2010) disappears for larger systems, while the behavior at the bona fide critical point in CANDIA et al. (2021) holds, theoretically for infinite-sized networks as it is scale independent.

By looking at the phase plane in Fig. 20C, the nullclines start to approach one another close to the fixed point (represented as an empty circle). This behavior is common at, or close to, Bogdanov-Takens-like bifurcations. Considering the Jacobian shown in Eq. (3.18) with small and positive $\lambda_{1/2} \to 0^+$, which is the condition proposed in their analysis, showing the proximity to a Bogdanov-Takens bifurcation. In the next chapter, we analyze the system at a transition with a Jacobian that takes the normal form of the Bogdanov-Takens:

$$J_{BT} = \begin{pmatrix} 0 & 1 \\ 0 & 0 \end{pmatrix}. \tag{3.22}$$

At this transition, we find a second-order phase transition with all the hallmarks of criticality.

Figure 20 – Avalanche dynamics for parameter values $h = 10^{-3}$, $w_0 = 0.2$, $w_+ = 13.8$. A) Mean network firing rate over a raster plot of spikes. B) Burst distribution of spikes with a geometric distribution ($P(k) = (1-p)^{k-1}p$) fit in red and a power-law in blue. The quantities Δt is the inter-spike interval and β is the power-law fit. The inset shows the inter-spike interval distribution for a sample of 50 neurons with an exponential fit in green. C) Phase plane plot. The nullclines are in red and blue, the stochastic trajectory in bright green, the deterministic trajectory in a dashed black line, and the flow in black arrows.

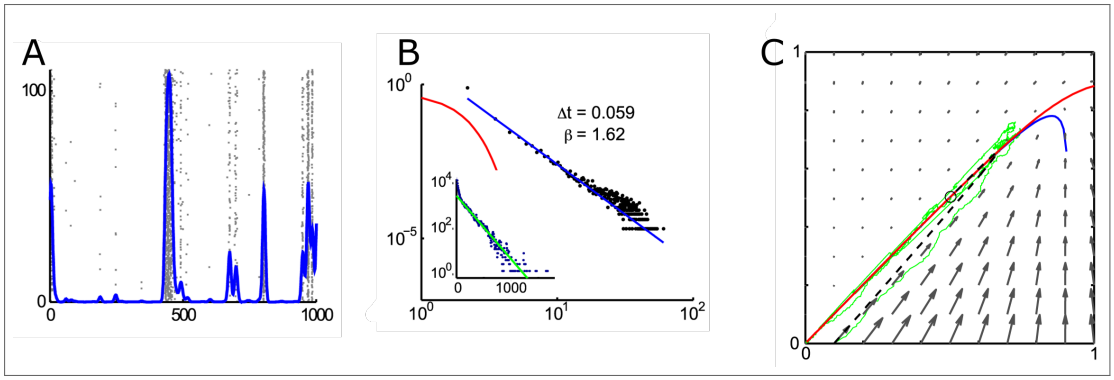

Source: Adapted from (BENAYOUN et al., 2010)

In order to systematically explore the full set of possible phase transitions, in the next chapter, we remove the constraints of symmetrical weights from the aforementioned works and the change of variables in Eq. (3.16) and Eq. (3.17) is no longer interesting, considering the arguments of the response functions (or the inputs) are different. The model could be implemented on different types of networks, as specified by the connectivity matrix $\omega_{\ell m}$ in Eq. (3.13). Thus, we will tackle the four synaptic weights represented in Fig. 16A, which, in a mean-field approach, follow:

$$\dot{E} = -\alpha E + (1 - E)\,\Phi\left(w_{EE}E - w_{EI}I + h\right), \tag{3.23}$$

$$\dot{I} = -\alpha I + (1 - I)\,\Phi\left(w_{IE}E - w_{II}\,I + h\right)\ . \tag{3.24}$$

We will also assume a large population of neurons, of size N, in a fully connected network, since the analytical solutions are exact for $N \to \infty$ (MARRO; DICKMAN, 1999a; KAMPEN, 2007; GARDINER, 2004).

4 RESULTS AND DISCUSSION

This chapter starts with a description of the five possible phases that arise when the model lacks the symmetric constraints: $w_{EE} = w_{IE}$ and $w_{II} = w_{EI}$; and follows with descriptions of the phase transitions between them. Observe that, for the purposes of this chapter, *phase transitions* are indistinct from *bifurcations* since our descriptions refer to fully-connected large-sized networks (i.e., mean-field systems). Illustratively, Fig. 23 shows the numerically simulated behavior of the dynamical system (Eq. 3.23 and Eq. 3.24), while Fig. 24 shows the stochastic counterpart.

The transitions that take the system from one phase to the other are either continuous (second-order), discontinuous (first-order), or a hybrid of both. The continuous transitions described in this chapter define bonafide critical points following the well-known universality classes: Mean-Field Directed Percolation (DP) and Mean-Field Tricritical Directed Percolation (TDP); and a new one, the Mean-field Hopf Tricritical Directed Percolation (HTDP). The discontinuous transition marked by a phase of coexistence corresponds to a curve of saddle-node bifurcations. And, finally, the transitions that display a mixture of both characteristics stem from the piecewise-smooth nature of the response function.

4.1 MEAN-FIELD PHASE DIAGRAMS

Let us take a second look at the Wilson-Cowan dynamic equations (Eq. 3.23 and Eq. 3.24), in the absence of any external driving force ($h = 0$),

$$\dot{E} = -\alpha\, E + (1 - E)\, \Phi\, (w_{EE}\, E - w_{EI}\, I)\,, \tag{4.1}$$

$$\dot{I} = -\alpha\, I + (1 - I)\, \Phi\, (w_{IE}\, E - w_{II}\ \ I)\,. \tag{4.2}$$

Since, $\Phi(0) = 0$, the trivial solution $(E^*, I^*) = (0, 0)$ is always a steady-state solution for Eq. (4.1) and Eq.(4.2), defining the *quiescent state*.

Considering the response function as a piecewise-smooth curve, the state-space of the system acquires three distinct regions that depend on the sign of the total input (s^E or s^I). Inside each region, the system displays a different dynamic profile. Limiting these regions are

the *switching manifolds*

$$s^E = w_{EE}\,E - w_{EI}\;I = 0\,, \tag{4.3}$$

$$s^I = w_{IE}\,E - w_{II}\;I = 0\,, \tag{4.4}$$

on which the trajectories may cross or slide (GLENDINNING; JEFFREY, 2019) depending on the flow around it, see Fig. 21 and Appendix C.

Figure 21 – Regions in the state space for two sets of parameters: a) $\alpha = 1$, $w_{EE} = 2.7$, $w_{EI} = 1.5$, $w_{IE} = 1.5$, and $w_{II} = 0.5$; and b) $\alpha = 1$, $w_{EE} = 2.7$, $w_{EI} = 1.0$, $w_{IE} = 1.5$, and $w_{II} = 0.64$. Observed in different shades of blue are the switching manifolds described in Eq. (4.3) and Eq. (4.4) and, as well as a few trajectories, in pink dashed arrow lines.

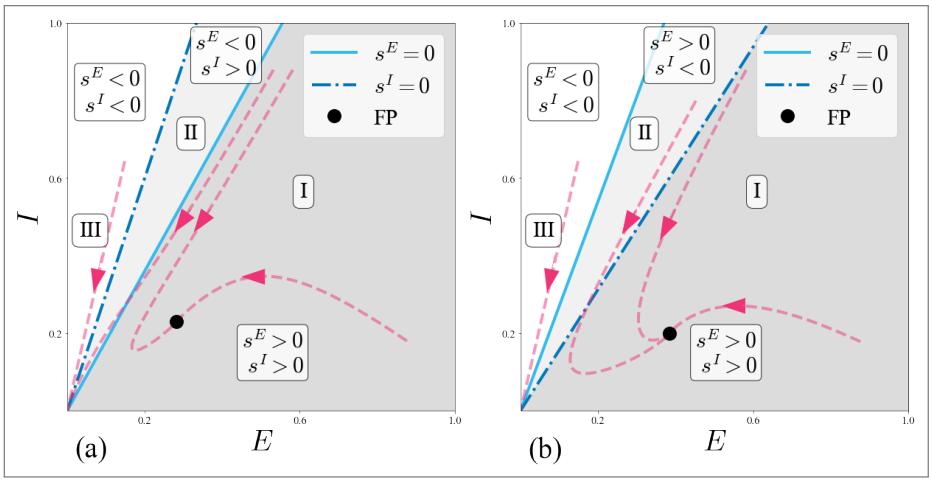

Source: Adapted from (PIUVEZAM et al., 2023)

Region III is defined by $s^E < 0$ and $s^I < 0$, which means that in both Eq (4.1) and Eq (4.2), $\Phi(s^\ell) = 0$. Inside said region, both populations are uncoupled and have an exponential decay. Along the switching manifold, whichever it may be, $s^E = 0$ or $s^I = 0$, there is sliding. Therefore, the trajectories are trapped inside the region, and, for initial conditions sufficiently close to the switching manifold, the trajectories slowly decay onto the switching manifold towards the quiescent state (See Appendix C).

Region II is located in between the two switching manifolds and the order of the switching manifolds counter-clockwise will specify which population decays exponentially inside of it. On one hand, when $w_{EE}/w_{EI} < w_{IE}/w_{II}$ (See Fig. 21a), the switching manifold between regions I and II is $s^E = 0$ and is the case most explored in the course of this study. For this condition, in region II, I displays nonlinear dynamics coupled with an exponential decay in E. On the switching manifolds and for initial conditions sufficiently close to $s^E = 0$, trajectories cross from region I to region II and are trapped. On the other hand, when $w_{EE}/w_{EI} > w_{IE}/w_{II}$ (Fig. 21b), $s^I = 0$ is between region I and II and the dynamics in region II is nonlinear for

E coupled with an exponential decay for I. For this particular case, though the trajectories also cross at the switching manifolds, the flow points from region II to region I. Therefore, trajectories that start at region I never cross to region II but the ones that start inside of region II and begin sufficiently close to $s^I = 0$ cross to region I and are trapped (See Fig. 21 and calculations in Appendix C).

Finally, region I is defined by two coupled nonlinear equations, i.e., $s^E > 0$ and $s^I > 0$. Observe that for this region, the response function has a well-defined inverse. Therefore, the non-trivial solutions ($E^* > 0$ and $I^* > 0$) are

$$E^* = \frac{1}{w_{IE}}\left[w_{II}I^* + \Phi^{-1}\left(\frac{\alpha I^*}{1-I^*}\right)\right], \tag{4.5}$$

$$I^* = \frac{1}{w_{EI}}\left[w_{EE}E^* - \Phi^{-1}\left(\frac{\alpha E^*}{1-E^*}\right)\right], \tag{4.6}$$

and characterize the *active state*. For the purposes of scaling calculations, region I is the most relevant region.

In what follows, we describe the phases and their stability as a function of the parameters. Observe that there are some constraints on the parameters: the weights are nonnegative, i.e., $w_{ij} \geq 0$, and the activity decay is positive, i.e., $\alpha > 0$. Furthermore, the phase diagrams may take one of three forms (see Fig. 22), which are unraveled at the end of the section.

Figure 22 – Phase diagrams for all cases with parameter values: $\alpha = 1$, $w_{II} = 0$, and $w_{IE} \in [3.0, 1.0, 0.8]$. The cases are labeled by letters A, B, and C, respectively.

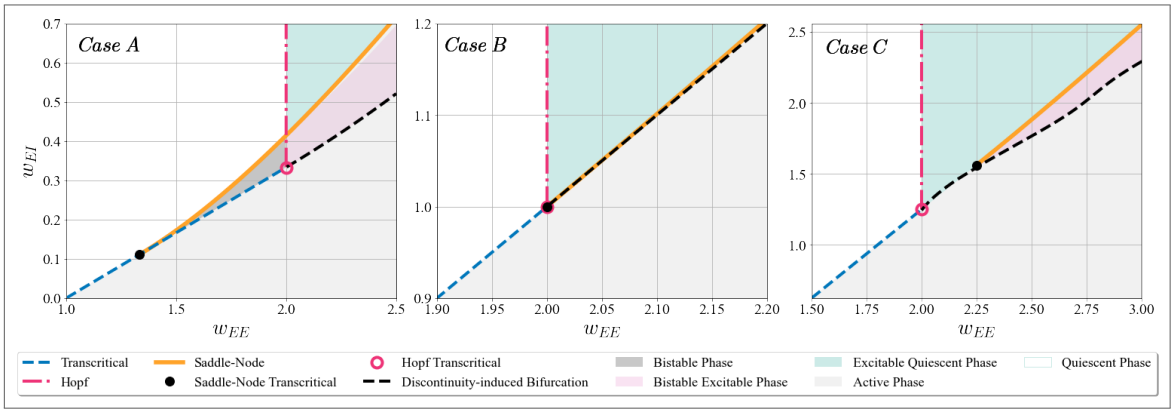

Source: Adapted from (PIUVEZAM et al., 2023)

4.1.1 Quiescent phase types and stability limits

The nature of the quiescent states depends on the regions, the quiescent state is always stable inside the regions that are trapping, i.e., the initial conditions inside the regions decay to

zero. If our system finds itself inside of region III, the only stable state is the quiescent one. The same logic applies to region II, which means that the trajectories that fall inside these two regions necessarily decay to quiescence. The introduction of *inhibition-dominated* perturbations – i.e., initial conditions where $E(0) < I(0)$ – may drive the system to a perpetually quiescent regime, depending on the choice of parameters. As an example, when $w_{EE}/w_{EI} < w_{IE}/w_{II}$ (Fig. 21a), inhibition-dominated perturbations drive the systems inside region II and III; however, when $w_{EE}/w_{EI} > w_{IE}/w_{II}$ (Fig. 21b), there is a possibility that the system evolves to be trapped inside region I. To avoid these situations, the calculations on linear stability consider only *excitation-dominated* perturbations and regard the dynamics in region I.

Considering the nonlinear differential equations for the excitatory and inhibitory populations, we can calculate the eigenvalues associated with the linear stability matrix at the quiescent state as:

$$\lambda_{\pm} = \frac{w_{EE} - 2\alpha - w_{II} \pm \sqrt{(w_{EE} + w_{II})^2 - 4w_{EI}w_{IE}}}{2} \,. \tag{4.7}$$

The state is linearly (or locally) stable when the eigenvalue has a negative real part. We emphasize the word locally because the trajectories that are repelled by the linearly unstable quiescent state have the possibility of falling into region II or III, where the dynamics follow an exponential decay in one or both fields and the quiescent phase is the only attractor, still defining a quiescent or a bistable phase.

When the eigenvalues have a positive real part and an imaginary component, one expects

Figure 23 – Comparative of quiescent and active phases. The fixed parameters: $\alpha = 1.0$, $w_{II} = 0.2$, and $w_{EI} = 2.0$. The standard quiescent simulated for parameters ($w_{EE} = 1.2$ and $w_{IE} = 0.2$). The excitable quiescent for ($w_{EE} = 2.2$ and $w_{IE} = 1.0$). And active for ($w_{EE} = 1.8$ and $w_{IE} = 0.2$). Observe that there are five different initial conditions marked as filled circles at the tip of the trajectories – i.e., the magenta dashed lines in the insets.

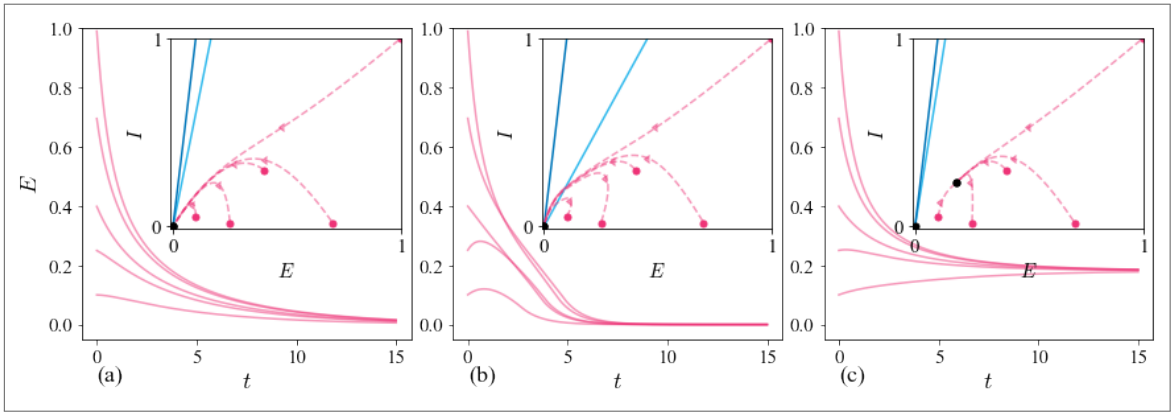

Source: Adapted from (PIUVEZAM et al., 2023)

the emergency of oscillations away from the quiescent state. However, these elicited oscillations are interrupted as the trajectories reach the switching manifolds, inside which the quiescent state is the only attractor. In this regime, small excitatory perturbations to the quiescent phase may give rise to larger trajectories in state space before falling into the exponential decay region (see Fig. 23b and Fig. 24b). The phase is then called *excitable quiescent* due to this so-called "excitability" or "reactivity" (ASSIS; COPELLI, 2009; BENAYOUN et al., 2010; ASSIS; COPELLI, 2012; SANTO et al., 2018; PINTO; COPELLI, 2019; LÓPEZ; BUENDÍA; MUÑOZ, 2022).

The *standard quiescent* phase is the regime where the quiescent state is locally stable for excitation-dominated perturbations (see Fig. 23a and Fig. 24a). The eigenvalue can be either real or complex, which changes the nature of the fixed point. So the quiescent state inside the phase can be a stable node or a stable focus. There is a curve separating the focus and the node nature of the quiescent state when the eigenvalue becomes real,

$$w_{EE}^{\dagger} = 2\sqrt{w_{EI}w_{IE}} - w_{II} \ . \tag{4.8}$$

Observe that this curve is not present in Fig 22, since this change in nature does not constitute a bifurcation or a transition because its stability remains the same.

The standard quiescent state loses its linear stability in two ways. On the interface between the two quiescent phases, the eigenvalue is complex, i.e., $(w_{EE} + w_{II})^2 - 4w_{EI}w_{IE} < 0$. Therefore, the standard quiescent state loses its stability on a curve of supercritical Hopf bifurcations, magenta dashed-line in Fig 22, conditioned by

$$w_{EE}^{H} = 2\alpha + w_{II} \ , \tag{4.9}$$

and the only globally stable state is the excitable quiescent one, defining the excitable quiescent phase.

Conversely, when the eigenvalue is real – i.e., $(w_{EE}+w_{II})^2-4w_{EI}w_{IE} > 0$ – the quiescent state is a stable node and the largest eigenvalue becomes positive at

$$w_{EE}^{T} = \alpha + \frac{w_{EI}w_{IE}}{\alpha + w_{II}} \ . \tag{4.10}$$

Observe that at this condition the quiescent state is still a solution, however, it becomes unstable. So dynamically, this condition marks a curve of transcritical bifurcations that in the phase portrait separates the standard quiescent and the active phases and is illustrated as a blue dashed line in Fig 22.

Figure 24 – Raster plot of the different Quiescent Phases and Active. The fixed parameters: $\alpha = 1.0$, $w_{II} = 0.2$, and $w_{EI} = 2.0$. The standard quiescent simulated for parameters ($w_{EE} = 1.2$ and $w_{IE} = 0.2$). The excitable quiescent for ($w_{EE} = 2.2$ and $w_{IE} = 1.0$). And active for ($w_{EE} = 1.8$ and $w_{IE} = 0.2$). The system was simulated for $N = 5000$ and initial condition $N_E(0) = N * 0.25$ and $N_I(0) = 0$.

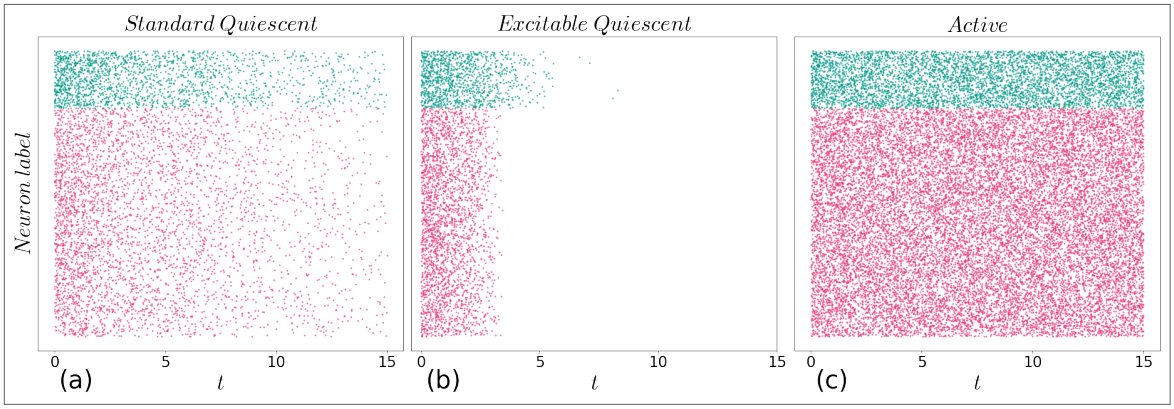

Source: The author (2023)

4.1.2 Active phase and its stability limits

After a transcritical bifurcation, a stable active state emerges continuously from the quiescent state, which, as we will show subsequently, corresponds to a directed percolation transition between the standard quiescent and active phases. However, the transition between these phases may also go through a coexistence (bistable) phase, when the active state becomes stable in a saddle-node bifurcation emerging discontinuously from the quiescent state. The condition for the curve of saddle-node bifurcations, orange continuous line in Fig 22, is

$$w_{EE}^{SN} = \min_{E^*} \left[\frac{w_{EI} I^*(E^*)}{E^*} + \frac{1}{E^*} \Phi^{-1} \left(\frac{\alpha E^*}{1 - E^*} \right) \right] , \tag{4.11}$$

where E^* and I^* are numerical solutions of Eq. (4.5) and Eq.(4.6).

Joining these two types of transitions, there is a tricritical point that corresponds to a "saddle-node-transcritical" (SNT) bifurcation, black-filled circle in Fig. 22. The mathematical condition for this point comes from a standard linear-stability analysis of the stationary solution around zero. A linear approximation of Eq. (4.5) around the quiescent solution yields a value of I^* proportional to the density of active excitatory neurons E^*

$$E^* = \frac{1}{w_{IE}} \left[w_{II} I^* + \Phi^{-1} \left(\frac{\alpha I^*}{1 - I^*} \right) \right] \tag{4.12}$$

$$= \frac{1}{w_{IE}} \left(w_{II} + \alpha \right) I^* + \mathcal{O}(I^{*2}) . \tag{4.13}$$

Therefore, either E^* or a weighed sum of both can be regarded indistinctively as an order parameter. From Eq. (4.5) and Eq. (4.6), w_{EE}^* may be expressed as a function of the fixed-

point solution (E^*, I^*):

$$w_{EE}^* = \frac{1}{E^*}\left[w_{EI}I^* + \Phi^{-1}\left(\frac{\alpha E^*}{1-E^*}\right)\right]. \tag{4.14}$$

Expanding it in a power series around the quiescent state, we observe the emergence of a stable active state solution at the transcritical bifurcation [w_{EE}^T, see Eq. (4.10)]. Furthermore, we define the distance to the transition – i.e., the distance to the critical value of the control parameter, $\Delta = w_{EE} - w_{EE}^T$, and observe that this non-trivial solution scales linearly with Δ as

$$E^* \sim I^* \sim [(\alpha + w_{II})^3 - w_{EI}w_{IE}^2]^{-1}\Delta\ , \tag{4.15}$$

as long as $(\alpha + w_{II})^3 - w_{EI}w_{IE}^2 \neq 0$. For $(\alpha + w_{II})^3 - w_{EI}w_{IE}^2 = 0$, Eq. (4.15) diverges and, therefore, marks a collision between the saddle-node and transcritical curves into a codimension-2 bifurcation called saddle-node transcritical (SNT) bifurcation (VEEN; HOTI, 2019; LAI; ZHU; CHEN, 2020), which occurs at

$$w_{EI}^{SNT} = \frac{(\alpha + w_{II})^3}{w_{IE}^2}, \tag{4.16}$$

$$w_{EE}^{SNT} = \alpha + \frac{(\alpha + w_{II})^2}{w_{IE}}\ . \tag{4.17}$$

The transition between the excitable quiescent and active phases is always mediated by a regime of coexistence – called the bistable excitable phase. Therefore, the saddle-node bifurcation extends into the excitable quiescent phase enclosing the new bistable regime. The transcritical bifurcation, however, loses its meaning considering that the excitable quiescent state is linearly unstable, and the *discontinuity-induced bifurcation* replaces it, although they may appear to be a continuation of the curve of transcritical bifurcations in Fig. 22, the mathematical condition for each is different.

The discontinuity-induced bifurcation is a direct consequence of the piecewise smooth dynamics of the system (HARRIS; ERMENTROUT, 2015) and its curve of bifurcations (numerically determined) delimits the excitable quiescent loss of global stability. In a piecewise smooth system, bifurcations inside the regions behave as they would in regular systems; however, the switching manifolds introduce new possibilities. If the dynamics in region I drive the system inside region II or/and III, the dynamics change and the nature of the switching manifold forces the stability of the quiescent state. The change in stability of a fixed point on top of the switching manifolds forced by this behavior is called a discontinuity-induced bifurcation. In summary, between the line of saddle-nodes and the line of discontinuity-induced bifurcations,

in a period of coexistence, the quiescent state is globally stable and there is an active locally stable fixed point. To the left of the discontinuity-induced bifurcations, the quiescent state loses global stability.

Observe that the discontinuity-induced bifurcations emerge from the transcritical bifurcations curve where the curve of Hopf bifurcations collides with the transcritical bifurcations at a point named Hopf-transcritical (HT), magenta unfilled circle in Fig 22. And from Eq. (4.10) and Eq. (4.9), we derive the conditions for the HT point:

$$w_{EI}^{HT} = \frac{(\alpha + w_{II})^2}{w_{IE}}, \tag{4.18}$$

$$w_{EE}^{HT} = 2\alpha + w_{II}. \tag{4.19}$$

Thus far, these conditions are fairly general, however, if one considers an extra fine-tuning of the parameters: $w_{IE} = \alpha + w_{II}$, the codimension-2 bifurcations HT and SNT merge into a codimension-3 bifurcation, black filled magenta circle in Fig. 22, defined by the choice of parameters:

$$w_{EI}^{H+SNT} = w_{IE}^{H+SNT} = \alpha + w_{II} \tag{4.20}$$

$$w_{EE}^{H+SNT} = 2\alpha + w_{II}. \tag{4.21}$$

This bifurcation also related to a tricritical point and is called a Hopf saddle-node-transcritical (H+SNT) bifurcation.

4.1.3 Qualitative Different Phase Diagrams: Cases A, B, and C

The relative position of the HT in relation to the SNT qualitatively changes the landscape of the phase diagram. Hence, in what follows, we analyze the possible phase diagrams fixing the activity-decay rate $\alpha \neq 0$ and the self-inhibition weight $w_{II} \geq 0$ and choosing w_{EE} and w_{EI} as control parameters. The system displays three different types of phase diagrams in the (w_{EE}, w_{EI}) plane depending on the value of the remaining free parameter, w_{IE}, without any loss of generality. Choosing another set of order parameters also describes these three topologies of phase diagrams, since the equations that shape them depend on all the parameters.

In case A, the HT point (unfilled magenta circle) lies to the right of the tricritical point (filled black circle) in Fig. 25. This case comprises all possible phase diagrams where $w_{EE}^{SNT} < w_{EE}^{HT}$. From Eq. (4.17) and Eq. (4.19), we use the free parameter w_{IE} as a function of the two fixed ones to parameterize the cases: $w_{EI} > w_{II} + \alpha$.

Figure 25 – Phase diagram for case A with parameter values: $\alpha = 1$, $w_{II} = 0$, and $w_{IE} = 3$. For this case, the phase diagram shows four types of transitions $T_1, \ldots, T_4$ in horizontal black segments.

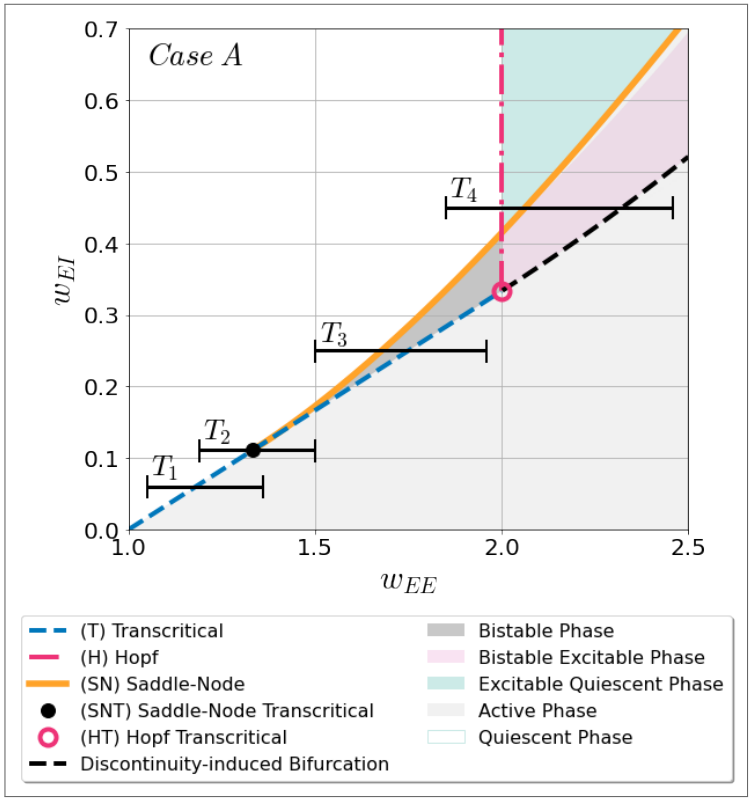

Source: (PIUVEZAM et al., 2023)

The four possible transitions from a quiescent to the active phase are marked by black horizontal segments in Fig. 25. The first transition from the bottom in Fig. 25, T_1, is a continuous transition from the standard quiescent to active phases, going through a transcritical bifurcation (dashed blue curve); as we will see bellow, this transition corresponds to the well-known mean-field directed percolation universality class. The second transition, T_2, is also continuous; however, this transition goes through a tricritical point, which represents an SNT bifurcation (filled black circle). The third transition, T_3, is discontinuous and it crosses curves twice: first, the saddle-node curve (continuous orange curve) into a standard bistable regime where there is a coexistence of quiescent and active stable states; and, second, the transcritical curve, into the active phase. The uppermost transition, T_4, is also discontinuous with bistability; although, in this case, the system crosses curves three times: first, the curve of Hopf bifurcations (dot-dashed magenta straight line) from the standard quiescent to the excitable phase; second, the saddle-node curve into the bistable excitable phase; and, third, the curve of discontinuity-induced bifurcations (dashed black curve) delimiting the active phase.

In case B, the HT point lies exactly on top of the SNT one, which reduces the amount of

Figure 26 – Phase diagram for case B with parameter values: $\alpha = 1$, $w_{II} = 0$, and $w_{IE} = 1$. For case B, T_1 and T_4 remain the same from case A in two black straight segments. However, where the HT and SNT bifurcations collide into the H+SNT bifurcation, the transition is T_5, also in a labeled black straight segment.

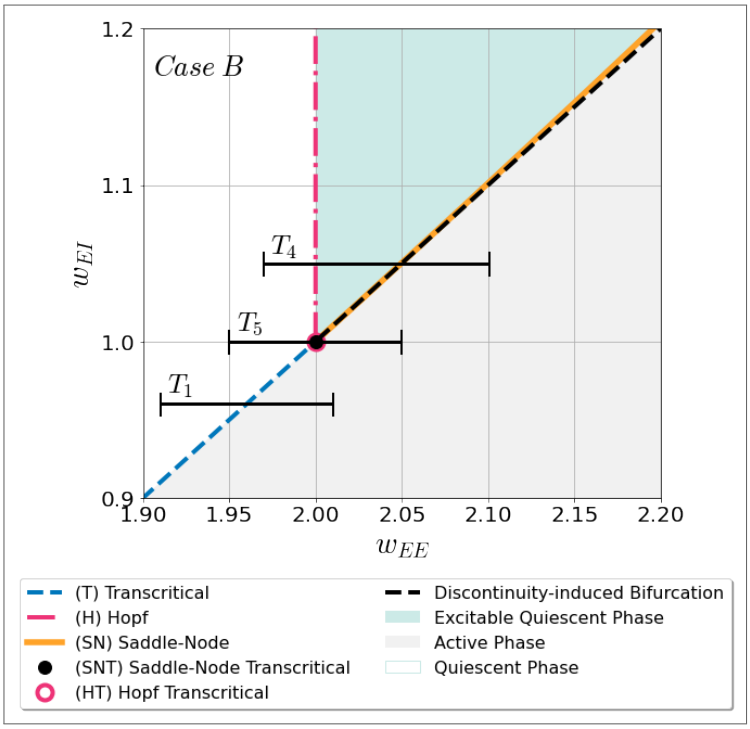

Source: (PIUVEZAM et al., 2023)

transitions to three (see Fig. 26). It requires a higher level of fine-tuning than the other two cases. Since $w_{EE}^{SNT} = w_{EE}^{HT}$ and from Eq. (4.17) and Eq. (4.19), we need to also fix the value of w_{IE} to $w_{II} + \alpha$. The first, T_1, and last, T_4, transitions remain unchanged. The new transition, T_5, is continuous and a tricritical point, going through a codimension-3 bifurcation, the Hopf saddle-node transcritical (H+SNT). Observe that the discontinuity-induced bifurcations curve seems to coincide with the saddle-node curve, however, there is a bistable excitable phase between them that gets progressively larger when the system moves away from the tricritical point in Fig. 26.

In this last case, case C, the HT point lies to the left of the SNT point. This cases comprises all possible phase diagrams where $w_{EE}^{SNT} > w_{EE}^{HT}$. Similarly to what we did for case A, we calculate the condition for the free parameter w_{IE} to $w_{IE} < w_{II} + \alpha$.

For this case, there are five types of transitions, including the first, T_1, and last, T_4, transitions marked as black straight segments in Fig. 27, which remain the same. The new transitions are all a mixture of continuous and discontinuous transitions, which we are going to better characterize further in this chapter. The second transition from the bottom in Fig. 27,

Figure 27 – Phase diagram for case C with parameter values: $\alpha = 1$, $w_{II} = 0$, and $w_{IE} = 0.8$. For case C, we observe T_1 and T_4 once again, alongside the emergence of three new transitions labeled T_6, T_7, and T_8, represented by black continuous segments.

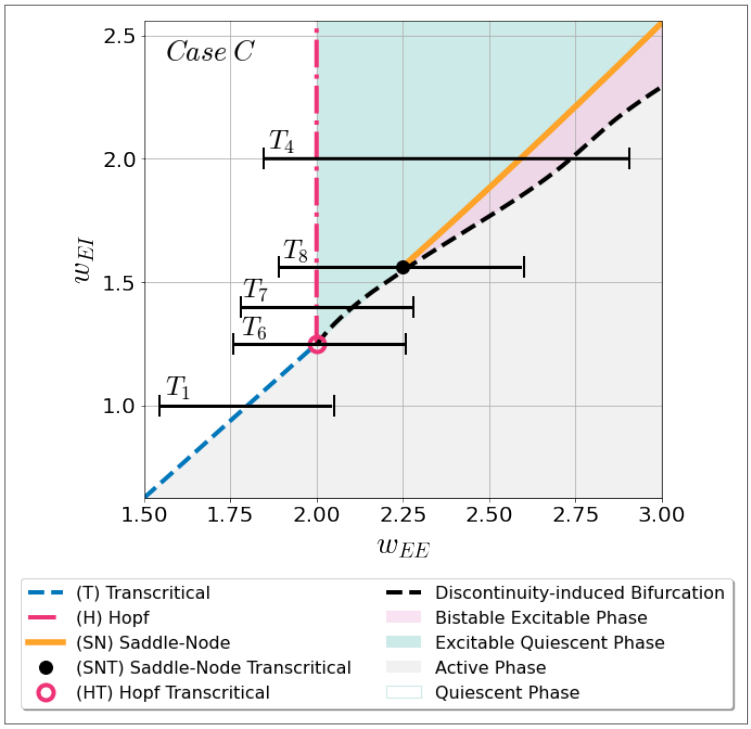

Source: (PIUVEZAM et al., 2023)

T_6, is a transition from standard quiescent to active that goes through the codimension-2 HT point (unfilled magenta circle). The third transition, T_7, goes through a discontinuity-induced bifurcation from the excitable quiescent to the active phase. And, finally, the fourth labeled transition, T_8, is a tricritical point, which goes through the codimension-2 collision of the saddle-node and discontinuity-induced bifurcations.

In the next sections, we analyze the generalized conditions for criticality and scrutinize each of the eight types of phase transitions (or bifurcations) —from T_1 to T_8.

4.2 GENERAL SCALING PROPERTIES

The linear stability and linear behavior analysis of the dynamical equations close to the quiescent states, Eq. (3.23) and Eq. (3.24), allows analytical predictions of the scaling behavior of the stochastic counterpart (MARRO; DICKMAN, 1999a; HENKEL; HINRICHSEN; LÜBECK, 2008).

Equipped with the conditions calculated in the previous section and the relationships calculated in Sec. 2.2, we compute the well-defined, if any, scaling exponents for all types of transitions. It is noteworthy that quantities related to transitions that are discontinuous or hy-

brid are not expected to exhibit universal behavior. The hybrid transitions may be associated with some exponents and have power law behavior but not across all expected aspects of its dynamics if they were bona fide critical points.

The quantities commonly measured for quiescent-active phase transitions may be divided into five categories: *static exponents*, *correlation exponents*, *dynamic exponents*, *spreading exponents*, and *avalanche exponents*. Generally, computing three independent exponents suffice to fully determine a universality class (MARRO; DICKMAN, 1999b); however, for the sake of completeness and to check consistency, when possible, we calculate more than three. In particular, we put a spotlight on the avalanche analysis, which helps with the comparison with experimental data.

The static exponents concern the behavior of the fixed point undergoing perturbations away from the critical point. The first exponent, β, pertains to the relationship between the zero-field ($h = 0$) fixed point and the control parameter

$$E^* \propto \Delta^{\beta} \, , \tag{4.22}$$

where $\Delta = w_{EE} - w^*_{EE}$ is the distance to the critical value and w^*_{EE} stands for the value of the control parameter w_{EE} at the transition. The second one, δ_h, represents the response to an external field h at the transition ($\Delta = 0$), i.e.,

$$E^* \propto h^{1/\delta_h} \, . \tag{4.23}$$

As explained in Sec. 2.2, the correlation exponents (ν) concern the correlation length, $\xi_{\perp}$, and the time correlation through the relaxation time, $\xi_{\parallel}$, which follow

$$\xi_{\perp} \propto \Delta^{\nu_{\perp}} \, , \tag{4.24}$$

$$\xi_{\parallel} \propto \Delta^{\nu_{\parallel}} \, , \tag{4.25}$$

respectively. The dynamic exponent, θ, governs the time decay of the order parameter

$$E(t) \propto t^{-\theta} \, . \tag{4.26}$$

The spreading exponents govern the basic evolution features of a system with self-similar dynamics: the number of active sites, the mean-squared radius in surviving runs, and the survival probability (MARRO; DICKMAN, 1999a), respectively:

$$N(t) \propto t^{\eta} \, , \tag{4.27}$$

$$R^2(t) \propto t^{z} \, , \tag{4.28}$$

$$P_s(t) \propto t^{-\delta} \, . \tag{4.29}$$

The avalanche exponents concern the distribution of avalanche sizes, S; durations, T; and, linking durations and averaged sizes, $S(T)$:

$$P(S) \sim S^{-\tau} , \tag{4.30}$$

$$P(T) \sim T^{-\tau_t} , \tag{4.31}$$

$$\langle S \rangle \sim T^{\gamma} . \tag{4.32}$$

The relationships calculated in Sec. 2.2 show that these exponents are related through scaling relations. In particular, the avalanche and spreading exponents follow

$$\tau = \frac{1+\eta+2\delta}{1+\eta+\delta} , \tag{4.33}$$

$$\tau_t = 1+\delta , \tag{4.34}$$

$$\gamma = \frac{\tau_t - 1}{\tau - 1} = 1+\delta+\eta , \tag{4.35}$$

where the relationship between the avalanche distribution exponents, Eq. (4.35), describes the so-called *crackling noise* scaling relation (SETHNA; DAHMEN; MYERS, 2001). Furthermore, the static, dynamic, and correlation exponents (β, θ, and $\nu_{\parallel}$, respectively) should obey the scaling relation

$$\theta = \beta/\nu_{\parallel} . \tag{4.36}$$

However, as discussed in Sec. 2.5, there are exceptions to this rule in the literature (NOH; PARK, 2005b).

Considering that we are studying the system in the mean-field approximation, the transitions are expected to share a set of exponents (MARRO; DICKMAN, 1999a; MARSHALL et al., 2016). For the T_1, T_2, T_5 (the continuous transitions), and T_6 (a hybrid transition), the diffusive nature of the stochastic system elicits divergent correlations at the critical point with shared exponents: the correlation length diverges with $\nu_{\perp} = 1/2$, and the relaxation time diverges with $\nu_{\parallel} = 1$.

Moreover, from Eq. (2.6) and the relation Eq. (2.17), we also observe that $z = 1$ remains constant across said transitions. The behavior of the survival probability, as discussed lengthly in Sec. 2.2 following the approach in (MUÑOZ; GRINSTEIN; TU, 1997), is a power law with exponent $\delta = 1$ at all quiescent to active continuous transitions, which implies, from Eq. 4.34, that $\tau_t = 2$. Lastly, the spreading exponent that governs the number of instantaneous active sites, η, is expected to vanish for mean-field continuous transitions (GRINSTEIN; MUÑOZ, 1996). However, we found an exception to that rule in the novel transition, T_5, where this spreading exponent is found to be $\eta = 2$, as discussed in the next sections.

4.3 DIRECTED PERCOLATION (TRANSCRITICAL BIFURCATION)

We start our analysis with T_1, which is a continuous transition from the standard quiescent to active phase and corresponds to a transcritical bifurcation in the dynamical system (Eqs.(3.23) and (3.24)). Considering the absence of additional symmetries or conservation laws in this quiescent-active continuous transition, we should expect it to belong to the mean-field directed percolation universality class (JANSSEN, 1981; GRASSBERGER, 1981; MARRO; DICKMAN, 1999a; HENKEL; HINRICHSEN; LÜBECK, 2008; GRINSTEIN; LAI; BROWNE, 1989b).

Figure 28 – Mean-Field Directed Percolation phase transition (T_1). (a) Steady-state solution of the dynamic equation as a function of the distance to transition value $\Delta = w_{EE} - w_{EE}^T$ for three values of constant external field h, in black $h = 0$, in an orange dashed curve $h = 0.01$, and in a magenta dotted curve $h = 0.001$. The blue dashed straight line represents the static exponent $\beta = 1$. (b) Numerically integrated steady-state solution as a function of the external field h at the transition $\Delta = 0$ in black and green dashed line to represent the static exponent $1/\delta_h = 1/2$. (c) Numerically integrated time decay solution with a green straight line representing the dynamic exponent $\theta = 1$. (d) Survival probability of simulation with Gillespie's algorithm and, as a guide to the eye, a green straight line that represents the spreading exponent $\delta = 1$. The system is plot at parameters: $\alpha = 1$, $w_{II} = 0$, $w_{EI} = 3$, $w_{IE} = 0.05$, and $w_{EE} = 1.15$.

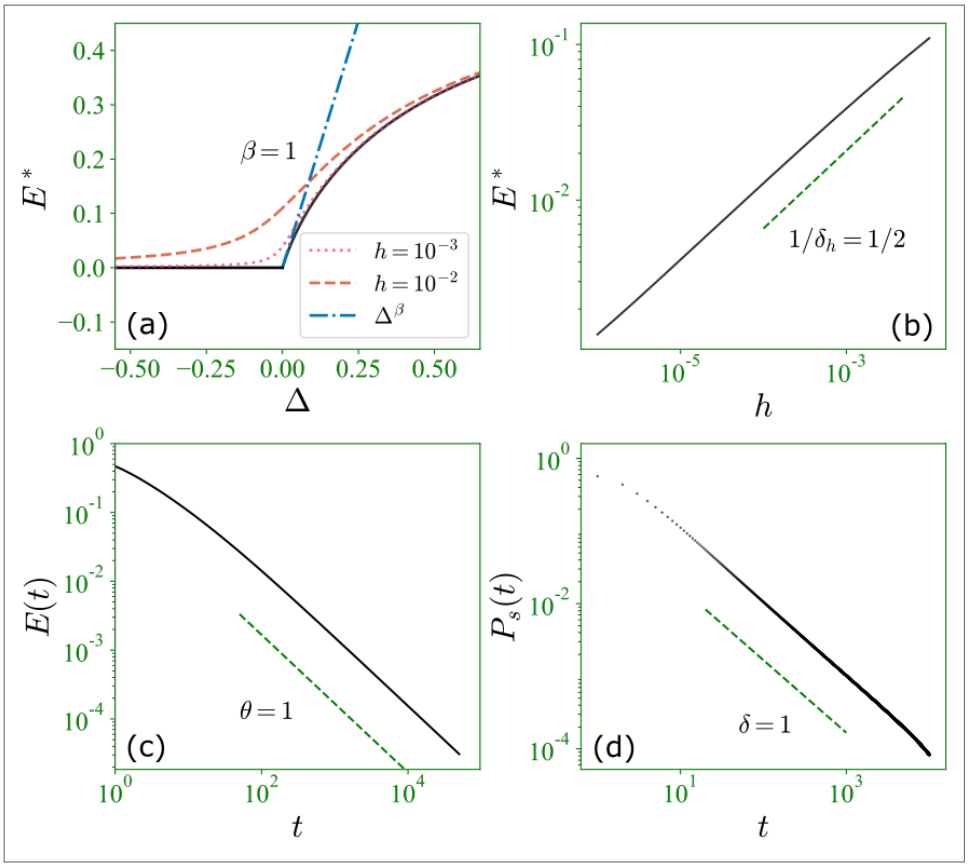

Source: The author (2023)

The condition for this bifurcation is $w_{EE}^T = \alpha + w_{EI}w_{IE}/(\alpha + w_{II})$ independently of the

case (see Eq. (4.10)). Expanding the stationary solutions of Eq. (3.23) and Eq. (3.24)

$$-\alpha E^* + (1 - E^*)\Phi\left(w_{EE}E^* - w_{EI}I^*\right) = 0, \tag{4.37}$$

$$-\alpha I^* + (1 - I^*)\Phi\left(w_{IE}E^* - w_{II}I^*\right) = 0, \tag{4.38}$$

in power series of E^* and I^* around the quiescent state yields, as mentioned before, I^* proportional E^*, $I^* \sim w_{IE}/(\alpha + w_{II})\ E^*$. The order parameter follows

$$E^*(\Delta; h = 0) = \frac{(\alpha + w_{II})^3}{(\alpha + w_{II})^3 - w_{EI}w_{IE}^2}\Delta + \mathcal{O}(\Delta^2)\ , \tag{4.39}$$

from which we find $\beta = 1$ (see Fig. 28a). Observe that introducing an external field h smooths out the transition (see dashed lines in Fig. 28a), one of the key aspects of bona fide critical points. To compute the second static exponent, we insert a small external field perturbation ($h \to 0$) and expand the stationary solutions, at $\Delta = 0$:

$$E^*(h; \Delta = 0) = \sqrt{\frac{(\alpha + w_{II})^2(w_{EI} - \alpha)h}{\alpha\left[w_{IE}w_{EI}^2 - (w_{II} + \alpha)^3\right]}} + \mathcal{O}(h)\ , \tag{4.40}$$

providing $\delta_h = 2$ (see Fig. 28b).

Since the solutions are proportional, we generalize a solution close to the quiescent state to $I(t) \approx [w_{IE}/(w_{II} + \alpha)]E(t)$ and it is convenient to define two new variables: Σ and Λ, as the weighted linear combination of the two The author (2023) variables:

$$2\Sigma = w_{IE}\ E + (w_{II} + \alpha)I\ , \tag{4.41}$$

$$2\Lambda = w_{IE}\ E - (w_{II} + \alpha)I\ . \tag{4.42}$$

The mean-field dynamical equations [Eq.(3.23) and Eq. (3.24)] become:

$$2\dot{\Sigma} \approx \Delta\Sigma + (2w_{EE} + 2w_{II} + \Delta)\Lambda + \mathcal{O}(\Sigma^2, \Lambda^2, \Sigma\Lambda, ...)\ , \tag{4.43}$$

$$2\dot{\Lambda} \approx \Delta\Sigma - \left[2(w_{EE} + w_{II} - 2\alpha) + \Delta\right]\Lambda + \mathcal{O}(\Sigma^2, \Lambda^2, \Sigma\Lambda, ...)\ , \tag{4.44}$$

where $\mathcal{O}(\Sigma^2, \Lambda^2, \Sigma\Lambda, ...)$ stands for higher-order terms. Right at the transition ($\Delta = 0$), the dynamics for Λ is homogeneous and linear, i.e., the trajectories decay exponentially. Therefore, Λ is an *irrelevant* field for scaling and the only *slow mode* or *relevant field* is Σ.

At the transition, $\Delta = 0$, the linear term of Eq. (4.43) vanishes and the quadratic term dominates. Thus, when integrated, $\Sigma(t) \propto t^{-1}$, which yields the dynamic exponent $\theta = 1$ (see Fig. 28c). Since β, δ_h, and θ are three independent exponents, it is already sufficient to conclude that the T_1 transition belongs in the directed percolation universality class (see

Table 2). Nevertheless, to round up this analysis, we simulate the system to verify the spreading quantities: survival probability, $\delta = 1$ (Fig. 28d); and the total number of particles, $\eta = 0$ (Fig. 33a). And summarize these exponents at Tab. 2.

In summary, the stochastic Wilson-Cowan model exhibits a genuine critical point in the directed percolation class related to a curve of transcritical bifurcations (T_1) between the standard quiescent and active phases. Our results are consistent with recent results from CANDIA et al. (2021) with the symmetric set of parameters shown in Sec. 3.2. When considering $w_E \equiv w_{EE} = w_{IE}$ and $w_I \equiv w_{II} = w_{EI}$, Eq. (4.10) becomes $w_E - w_I = \alpha$, which is their condition for the directed percolation.

4.4 STANDARD DISCONTINUOUS TRANSITION (SADDLE-NODE BIFURCATION)

The first discontinuous transition in case A, T_3, takes the system from the standard quiescent to the active phase through a coexistence phase. This phase of coexistence, or bistability, is limited by curves of saddle-node and transcritical bifurcations (see Figs. 25). After the saddle-node bifurcation, this transition displays a discontinuous jump in the order parameter and includes an intermediate regime of bistability, with stable active and standard quiescent states (see Fig. 29a). At the transcritical bifurcation, the quiescent phase loses its local stability, effectively ending the bistable regime.

Observe that, given the definition of the static exponents and the discontinuous nature of the transition, the exponents β and δ_h are not well-defined and are not expected to be so (Fig 29a,b). The same logic applies to the dynamic exponent, i.e., the average activity is not expected to decay to quiescence and, in fact, is dependent on the initial conditions (see Fig 29c). For completeness, we observe that, in the stochastic system, small perturbations drive the system into the active phase and lead to a positive survival probability (see Fig 29d). Thus, none of the exponents calculated previously are well-defined and the T_3 transition constitutes a standard first-order or discontinuous transition into a quiescent or absorbing phase (LÜBECK, 2006; ÓDOR, 2008).

Figure 29 – Standard discontinuous transition (T_3). (a) Steady-state solution as a function of the distance to the transcritical $\Delta = w_{EE} - w_{EE}^T$ for three values of constant external field h, in black $h = 0$, in an orange dashed curve $h = 0.01$, and in a magenta dotted curve $h = 0.001$. The plot displays an area of coexistence (shaded) for $h = 0$. Observe that for $h = 0.001$ the transition remains discontinuous. (b) Steady-state solution as a function of the external field h right before the transcritical bifurcation at $\Delta = -0.001$ in black with the shaded area describing coexistence. (c) Time decay solution with different initial conditions to show the stable steady states. (d) Survival probability of simulation with Gillespie's algorithm showing a positive survival probability, as the system may fall to an active state depending on the run. The system is plot at parameters: $\alpha = 1$, $w_{II} = 0$, $w_{EI} = 3$, $w_{IE} = 0.5$, and $w_{EE} = 1.9$.

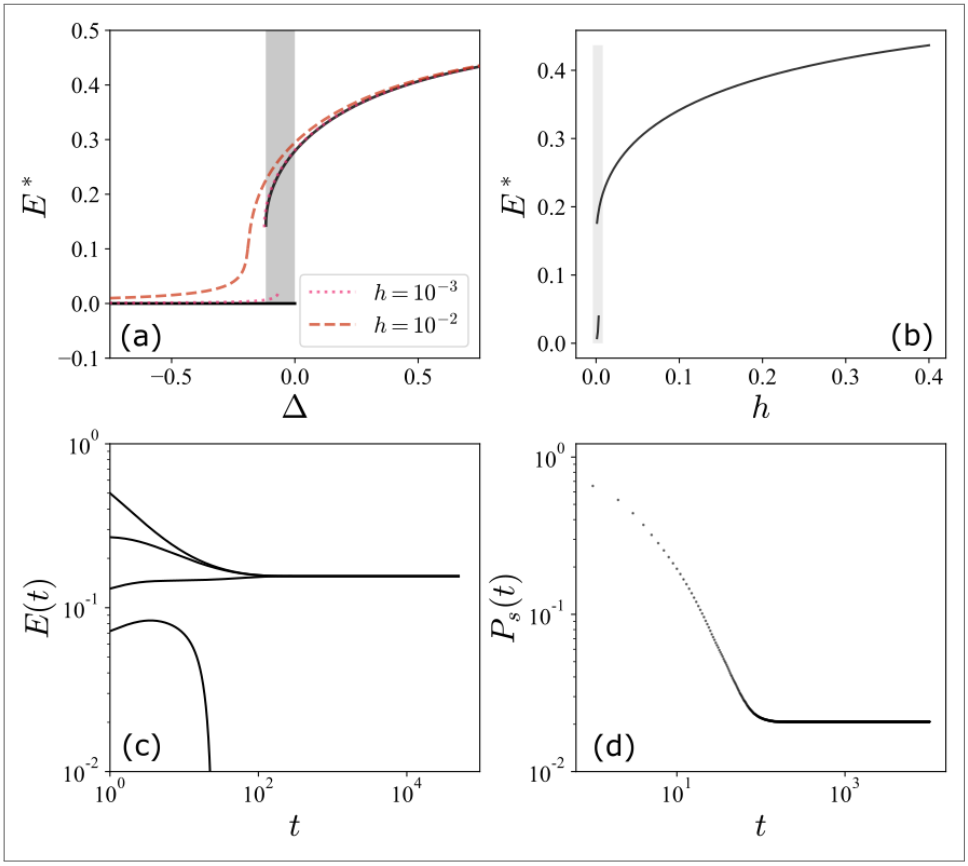

Source: The author (2023)

4.5 DISCONTINUOUS TRANSITION FROM AN EXCITABLE QUIESCENT STATE (SADDLE-NODE BIFURCATION)

The other transition common to all cases in the topologically different phase diagrams (see Fig. 25- 27), T_4, behaves very similarly to T_3. This transition is also discontinuous with bistability and it connects, in principle, the standard quiescent with the active phase. However, in this transition, the system visits four phases: the standard quiescent, the excitable quiescent, the bistable excitable, and the active one.

The coexistence phase, in T_4, comprises a globally stable quiescent state with a locally stable active state. On one side, the bistable phase is limited by the saddle-node bifurcation,

where the active phase emerges discontinuously. On the other side, the excitable quiescent state loses its global stability at a discontinuity-induced transition (black-dashed line in Fig. 22), from where the active state is the only stable attractor. For the same reasons as in T_3, i.e., discontinuous jump and phase of bistability, the critical exponents are ill-defined, as explicitly shown in Fig. 30a-d.

In summary, T_4 is also a discontinuous transition with bistability, with the caveat that instead of the coexistence between the standard quiescent and active phase, seen in T_3, here, the coexistence is between the excitable quiescent and active phases.

Figure 30 – Discontinuous transition (T_4). (a) Steady-state solution as a function of the distance to the discontinuity-induced $\Delta = w_{EE} - w^*_{EE}$ for three values of constant external field h, in black $h = 0$, in a darker orange dashed curve $h = 0.01$, and in a lighter orange dash-dotted curve $h = 0.1$. Observe that at the Hopf, $\Delta = 0.5$, a green shaded area emerges, representing the excitable quiescent state and at the saddle-node, around $\Delta \sim 0.4$, a pink shaded area represents the coexistence of the excitable quiescent and active states. (b) Steady-state solution as a function of the external field h right before the discontinuity-induced bifurcation at $\Delta = -0.001$ in black with the shaded area describing coexistence. (c) Time decay solution with different initial conditions to show the steady states, though the quiescent state is not locally stable it retains global stability. (d) Survival probability of simulation with Gillespie's algorithm showing a positive survival probability, as the system may fall to an active state depending on the run. The system is plot at parameters: $\alpha = 1$, $w_{II} = 0$, $w_{EI} = 3$, $w_{IE} = 0.5$, and $w_{EE} = 2.5$.

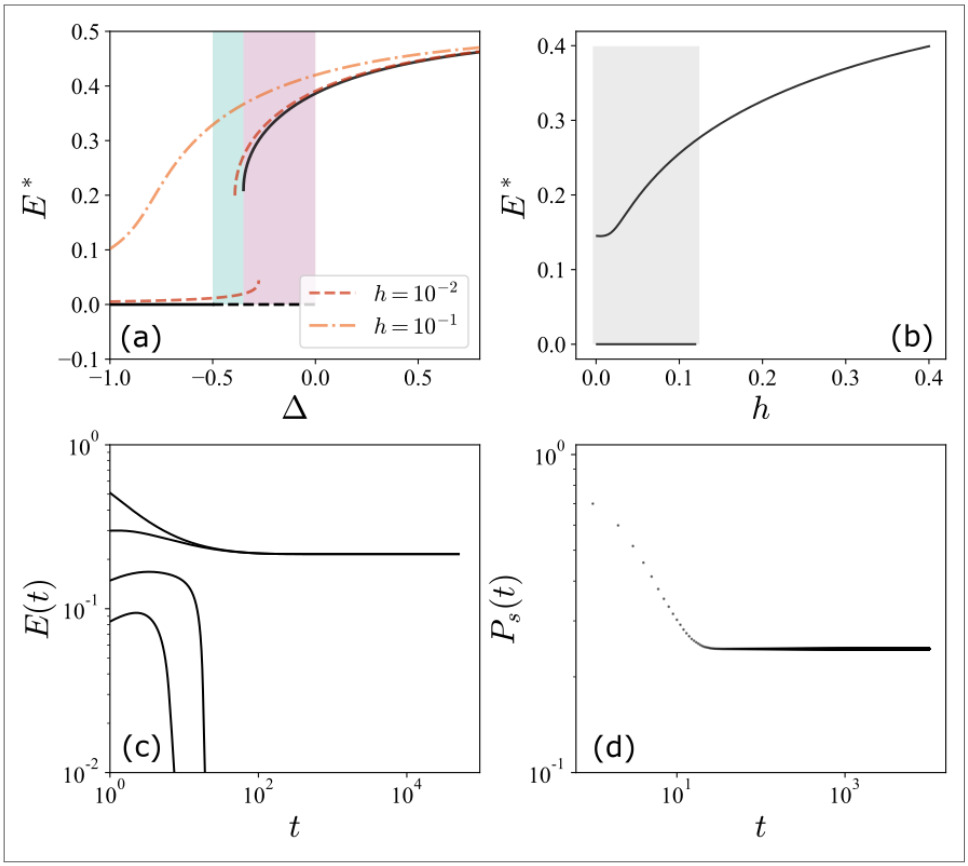

Source: The author (2023)

4.6 TRICRITICAL DIRECTED PERCOLATION (SADDLE-NODE-TRANSCRITICAL BIFURCATION)

In case A, T_2 goes through a tricritical point (see Fig. 25), which corresponds to a saddle-node transcritical bifurcation. This codimension-2 bifurcation marks where the curves of transcritical and saddle-node bifurcations intersect (VEEN; HOTI, 2019; LAI; ZHU; CHEN, 2020). Because of the higher co-dimension of this transition, we need to tune two parameters to find this point in the phase diagram (w_{EE}, w_{EI}). In Sec. 4.1, we computed the conditions for this tricritical point as w_{EE}^{SNT} and w_{EI}^{SNT} (see Eq. (4.17) and Eq. (4.16)). Considering that T_2 is a continuous transition through a tricritical point, we expect it to belong to the mean-field tricritical directed percolation universality class (LÜBECK, 2006).

Similarly to the previous section, we study the expansion in a power series of the static solutions (E^*, I^*). At the tricritical point, Eq. 4.39 diverges and we need to consider higher terms of the series. Considering the leading-order terms in a power expansion in both Δ and h, we obtain:

$$E^*(\Delta, h=0) \approx \sqrt{\frac{\Delta}{w_{IE}}} + \mathcal{O}(\Delta), \tag{4.45}$$

$$E^*(h, \Delta=0) \approx \left[\frac{3\left[w_{IE}^2 - (\alpha + w_{II})^2\right] h}{w_{IE}^2\left[(\alpha^2-3)w_{IE} - (\alpha^2+3)\alpha\right]}\right]^{\frac{1}{3}} + \mathcal{O}\left(h^{\frac{1}{2}}\right) \ ; \tag{4.46}$$

and the static exponents are $\beta = 1/2$ (Fig. 31a) and $\delta_h = 3$ (Fig. 31b).

Considering the changed variables Σ and Λ (Eq. (4.41) and Eq. (4.42)), at $\Delta = 0$, the lowest order correction of Eq. (4.43) in Σ is $\mathcal{O}(\Sigma^3)$. Therefore, we integrate it asymptotically, $\Sigma \propto t^{-1/2}$, which provides the dynamical exponent, $\theta = 1/2$ (see Fig. 31c). Once again, considering the linear relationship between $E(t)$ and $I(t)$, both densities share this scaling. The spreading exponents, δ and η, agree with the scaling of T_1, i.e., $\delta = 1$ (see Fig. 31d) and $\eta = 0$ (see Fig. 33a).

In conclusion, the stochastic Wilson-Cowan model also displays a transition, T_2, that belongs to the tricritical directed percolation universality class (LÜBECK, 2006).

Figure 31 – Mean-Field Tricritical Directed Percolation phase transition (T_2). (a) Numerically integrated steady-state solution as a function of the distance to transition value $\Delta = w_{EE} - w_{EE}^{SNT}$ for three values of constant external field h, in black $h = 0$, in an orange dashed curve $h = 0.01$, and in a magenta dotted curve $h = 0.001$. The blue dashed straight line represents the static exponent $\beta = 1/2$. (b) Numerically integrated steady-state solution as a function of the external field h at the transition $\Delta = 0$ and red dashed straight line represents static exponent $1/\delta_h = 1/3$. (c) Numerically integrated time decay solution with a red straight line representing the dynamic exponent $\theta = 1$. (d) Survival probability of simulation with Gillespie's algorithm and a red straight line representing the spreading exponent associated with the quantity $\delta = 1$. The system is plot at parameters: $\alpha = 1$, $w_{II} = 0$, $w_{EI} = 3$, $w_{IE} = 0.\bar{1}$, and $w_{EE} = 1.\bar{3}$.

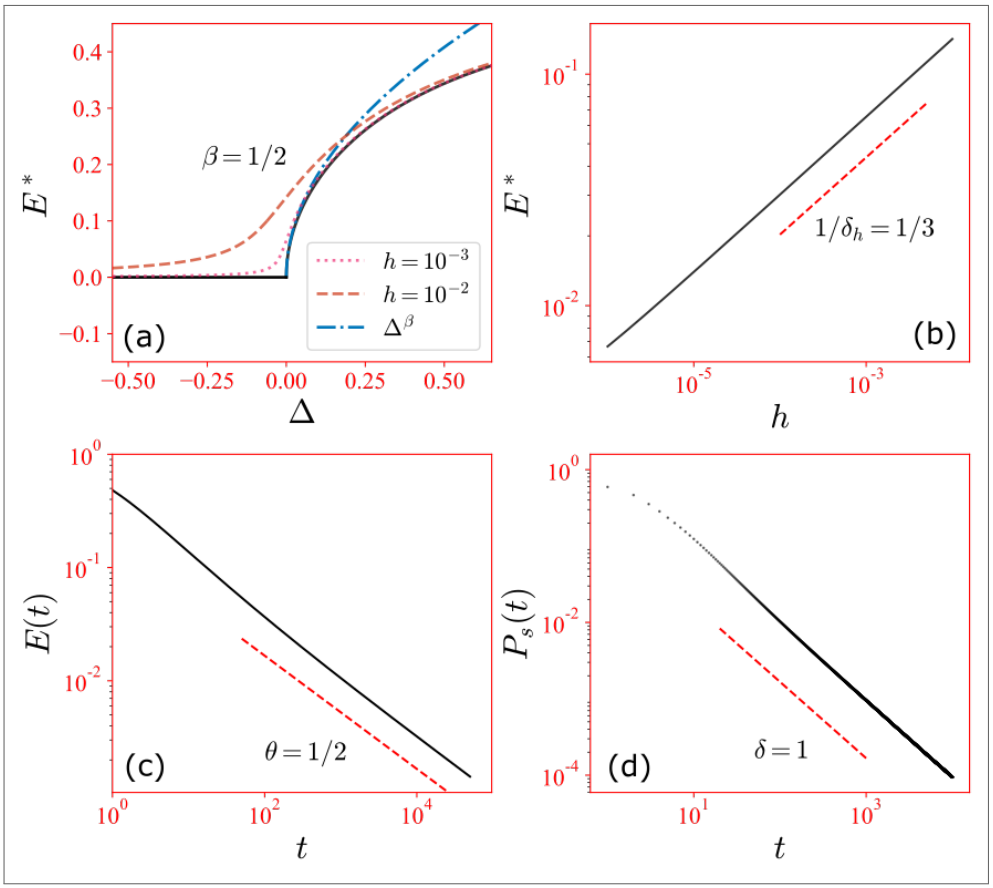

Source: The author (2023)

4.7 HOPF TRICRITICAL DIRECTED PERCOLATION (HOPF SADDLE-NODE-TRANSCRITICAL BIFURCATION)

In a co-dimension 3 bifurcation called Hopf saddle-node transcritical bifurcation, case B exhibits a novel type of transition. As the free parameter w_{EI} in Fig. 22 changes, the SNT (co-dimension 2) approaches the HT (co-dimension 2) point, colliding with it in a further fine-tuned tricritical point, which shows the collision of the curves of saddle-node, transcritical, and Hopf bifurcations (see Fig. 26). Since this case is an interface between two collections of phase diagrams (case A and case C), it requires the fixing of $w_{EI} = \alpha + w_{II}$. For this value

of w_{EI}, the conditions for the transition T_5, as calculated in Eq. (4.20) and Eq. (4.21), are $w_{EE}^{H+SNT} = 2\alpha + w_{II}$ and $w_{IE}^{H+SNT} = w_{EI}^{Case\,B} = \alpha + w_{II}$.

Following the procedure for continuous transitions in previous sections and expanding the stationary solutions in a power series of Δ and h (control parameter distance to its transition value and external field, respectively), we compute the static exponents. First, the stationary solution with $h = 0$ expanded around the quiescent state,

$$E^*(\Delta; h = 0) \approx \sqrt{\frac{\Delta}{\alpha + w_{II}}} + \mathcal{O}(\Delta) \ , \tag{4.47}$$

yields $\beta = 1/2$ (see Fig. 32a). And second, the stationary solution at the transtion ($\Delta = 0$) and with the introduction of h – which, similarly to T_1 and T_2, smooths out the curve $E^* \times w_{EE}$ (dashed curves in Fig. 32a),

$$E^*(h; \Delta = 0) \approx \sqrt{\frac{h}{3(\alpha + w_{II})^2}} + \mathcal{O}(h) \tag{4.48}$$

yields $\delta_h = 2$ (see Fig. 32b). Observe that, although $\beta = 1/2$ coincides with the corresponding value in the tricritical directed percolation universality class (Sec. 4.6), $\delta_h = 2$ fits into the exponents of the directed percolation universality class (Sec. 4.3), implying that T_5 does not belong to either well-known class.

The dynamic exponent requires us to change variables to the ones introduced in Sec. 4.6, Σ and Λ (Eq. (4.43) and Eq. (4.44)). Considering the new set of parameters, the dynamical equations [Eq.(3.23) and Eq. (3.24)] further simplify to

$$\begin{aligned} 2\dot{\Sigma}(t) &= \Delta(\Sigma + \Lambda) + 4(w_{II} + \alpha)\Lambda - \frac{2\alpha}{w_{II} + \alpha}\Sigma^2 - 4\Sigma\Lambda - \frac{2\alpha}{w_{II} + \alpha}\Lambda^2 \\ &\quad + \mathcal{O}(\Sigma^3, \Sigma^2\Lambda, \Sigma\Lambda^2, \Lambda^3, \Delta\Sigma^2 ...) \ , \end{aligned} \tag{4.49}$$

$$2\dot{\Lambda}(t) = \Delta(\Sigma + \Lambda) - 4\Lambda^2 - \frac{4\alpha}{w_{II} + \alpha}\Sigma\Lambda + \mathcal{O}(\Sigma^3, \Sigma^2\Lambda, \Sigma\Lambda^2, \Lambda^3, \Delta\Sigma^2 ...) \ , \tag{4.50}$$

where $\mathcal{O}(\Sigma^3, \Sigma^2\Lambda, \Sigma\Lambda^2, \Lambda^3, \Delta\Sigma^2 ...)$ stands-in for higher-order terms. At the transition, $\Delta = 0$, and the ODEs are

$$\dot{\Sigma}(t) = 2(w_{II} + \alpha)\Lambda - \frac{\alpha}{(w_{II} + \alpha)}\Sigma^2 + \mathcal{O}(\Sigma^3, \Sigma^2\Lambda, \Sigma\Lambda^2, \Lambda^3, \Delta\Sigma^2 ...) \ , \tag{4.51}$$

$$\dot{\Lambda}(t) = -2\Lambda^2 - \frac{2\alpha}{w_{II} + \alpha}\Lambda\Sigma + \mathcal{O}(\Sigma^3, \Sigma^2\Lambda, \Sigma\Lambda^2, \Lambda^3, \Delta\Sigma^2 ...) \ . \tag{4.52}$$

The Jacobian matrix of this expansion, at the transition, produces

$$A \propto \begin{pmatrix} 0 & w_{II} + \alpha \\ 0 & 0 \end{pmatrix} \ , \tag{4.53}$$

Figure 32 – Mean-Field Hopf Tricritical Directed Percolation transition (T_5). (a) Steady-state solution as a function of the distance to transition value $\Delta = w_{EE} - w_{EE}^{H+SNT}$ for three values of constant external field h, in black $h = 0$, in a darker orange dashed curve $h = 0.01$, and in a lighter orange dash-dotted curve $h = 0.1$. It is noteworthy that, for an observable difference in the plot, the system needs to be excited by a larger external field. The blue dashed straight line represents the static exponent $\beta = 1$. (b) Steady-state solution as a function of the external field h at the transition $\Delta = 0$ in black and green dashed line to represent the static exponent $1/\delta_h = 1/2$. (c) Time decay solution with a green straight line representing the dynamic exponent $\theta = 1$. (d) Survival probability of simulation with Gillespie's algorithm for two system sizes, $N = 10^8$ in black and $N = 10^{10}$ in gray, and a helping purple straight line that represents the spreading exponent $\delta = 1$. The system is plot at parameters: $\alpha = 1$, $w_{II} = 0$, $w_{EI} = 1$, $w_{IE} = 1$, and $w_{EE} = 2$.

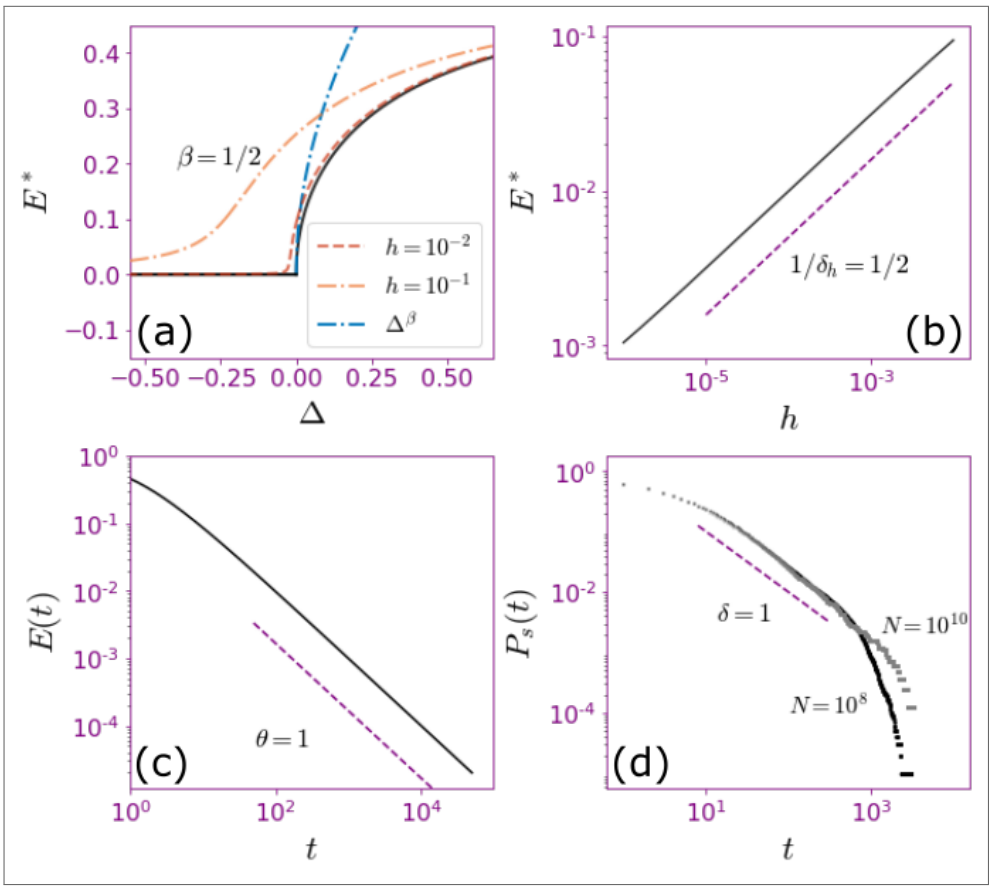

Source: The author (2023)

which is the normal form of a Bogdanov-Takens bifurcation (IZHIKEVICH, 2007). The Bogdanov-Takens bifurcation has been widely studied in the context of the Wilson-Cowan equations. In particular, we go through some of these analyses in Sec. 3.1.1.

The only non-zero element in the matrix (Eq. 4.53) is positive, which means that in, Eq. (4.51), Λ has a positive coefficient. In order to avoid any growth, $\Lambda(t)$ needs to decay faster than $\Sigma(t)$. Since $\Sigma(t)$ decays slower than Λ, the leading term of Eq. (4.51) is porportional to $-\Sigma^2$. Therefore, to find the time decay, we integrate

$$\dot{\Sigma} \propto -\frac{\alpha}{w_{II} + \alpha}\Sigma^2, \tag{4.54}$$

finding $\Sigma(t) \sim t^{-1}$ and the dynamic exponent $\theta = 1$ (see Fig. 32c). The faster decay of $\Lambda(t)$ is found by using this solution in Eq. (4.52) and comparing constants and exponents. Observe that, considering Eq. (4.51) and Eq. (4.52), there are two possible behaviors close to the the static solutions of variables Σ and Λ: Eq. (4.51) yields $\Lambda \propto \Sigma^2$ and Eq. (4.52) yields $\Lambda \propto -\Sigma$. The latter assumes that the inhibition activity is always larger than the excitation one, a regime which we are not interested in at this moment. Thus, combining $\Lambda \propto \Sigma^2$ and $\Sigma \sim t^{-2}$ results in $\Lambda \sim t^{-2}$. Observe that at the T_5 transition, the exponent associated with the time decay is consistent, once again, with the directed percolation universality class even if we are dealing with a tricritical point. If we go back to the tricritical point, in the tricritical directed percolation universality class, we would expect that the decay in Σ is dominated by a cubic term (see Sec. 4.6). However, in this choice of parameters, this tricritical point has a different behavior and its decay is dominated by the quadratic term, yielding $\Sigma \propto t^{-1}$.

In the supercritical regime, $\Delta > 0$, we turn our attention to Eq. (4.50) and analyze $\dot{\Lambda}$. For the stationary solution, the leading linear term, either $\Delta\Sigma$ or $\Delta\Lambda$ (depending on the dimensions of Λ and Σ), should be equal to the leading non-linear one $4\Lambda^2$ or $4\alpha/(w_{II}+\alpha)\Lambda\Sigma$, because in continuous transitions the solution for the emerging supercritical side should join with the quiescent state at the transition. If Λ has a lower dimension than Σ, the leading terms are

$$\Delta\Lambda = 4\Lambda^2 \,, \tag{4.55}$$

which yields $\Lambda \propto \Delta$. If the opposite is true, then, the leading terms become

$$\Delta\Sigma = 4\alpha/(w_{II}+\alpha)\Lambda\Sigma \,, \tag{4.56}$$

also yielding $\Lambda \propto \Delta$. Observe that, contrary to the previous universality classes, where the difference field was neglectable, the field Λ belongs to a different class than Σ, $\beta_\Lambda = 1$, both are important for scaling. It is noteworthy that Σ shares scaling with E and I. Considering the equation for $\dot{\Sigma}$ (Eq. (4.49)), the leading linear term is $4(w_{II}+\alpha)\Lambda$, since the term $\Delta(\Sigma+\Lambda)$ provides a higher-order contribution. Once again, we need to compare the leading positive with the leading negative term, which is $-\alpha(w_{II}+\alpha)\Sigma^2$. Observe that the other quadratic term in Σ and Λ, $-4\Sigma\Lambda$, either share scaling with the one proportional to $-\Sigma^2$ or yields a fixed value of Σ, i.e., independent of Δ, which is not a valid solution in this case. We, then, worked out that $\Lambda \propto \Sigma^2$, consistently with the solution for the time decay. Finally, we derive $\Sigma \sim \Delta^{1/2}$ and $\beta = 1/2$, consistently with the tricritical directed percolation universality class.

A priori, the fact that the transition has different exponents consistent with different universality classes in no way implies a problem or a break in theory. However, considering

that, as discussed in Sec. 4.2, the correlation exponent is $\nu_{\parallel} = 1$ for all mean-field transitions, the exponents for the H+TDP transitions lead to $\theta = 1$ and $\beta/\nu_{\parallel} = 1/2$, hence

$$\theta \neq \beta/\nu_{\parallel} \,, \tag{4.57}$$

thus failing to satisfy Eq. (4.36), which is one of the basic scaling relations regarding quiescent states (MUÑOZ et al., 1999). As described in Sec. 2.5, a similar violation in scaling is observed in the asymmetrically coupled directed percolation universality class (NOH; PARK, 2005b). The similarity in the models lies in the non-trivial interplay between these two fields with opposing effects, possibly yielding this break in scaling.

Regarding the spreading exponents, the survival probability decays similarly to the previous transitions, i.e., with an exponent $\delta = 1$ (see Fig. 32d), albeit with a need for a bigger system size to see the full effects of criticality. Conversely, the instantaneous number of active sites in spreading experiments at the transition, $N(t; \Delta = 0)$ diverges for T_5. In fact, we observe that $N(t) \sim t^2$, which gives us $\eta = 2$ (see Fig. 33b). This result is surprising since for most mean-field universality classes, where there are no *anomalous dimensions* (BINNEY et al., 1993; GRINSTEIN; MUÑOZ, 1996), hence $\eta = 0$, which was the value found for T_1 and T_2 (Fig. 33a).

Figure 33 – Mean number of particles $N(t)$ in spreading experiments in bona fide continuous phase transitions (i.e., T_1, T_2, and T_5), at which one expects $N(t) \sim t^{\eta}$. Simulations with the same parameters as Fig. 22 with $N = 10^8$ [panel (a)] and $N = 10^8$ and $N = 10^{10}$ [panel (b)]. (a) For T_1 and T_2, we obtain results compatible with $\eta = 0$, as expected for DP and TDP, as well as, in general, for mean-field theories. (b) On the other hand, for T_5 we obtain the unusual result $\eta = 2$, with strong finite-size effects.

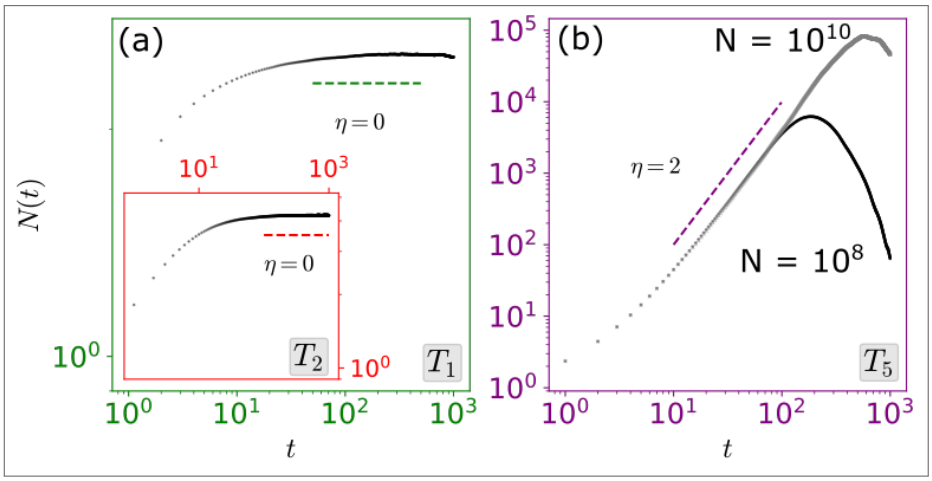

Source: (PIUVEZAM et al., 2023)

To understand this behavior, let us revisit the linearized dynamics at the transition, Eq. (4.53). Considering that the behavior at this transition follows the normal form of a Bogdanov-Takens, we expect that a small initial condition provokes a large trajectory in the state space before

heading back to the quiescent state, which gives the quiescent state the label of excitable. In order to find the spreading exponents, the system in spreading experiments is initiated with a single seed, from which the system grows deterministically until it reaches a maximum size and, then, decays with exponent θ. The perturbative term should follow

$$\frac{d}{dt}\begin{pmatrix}\xi_\Sigma\\ \\ \xi_\Lambda\end{pmatrix} = (w_{II}+\alpha)\begin{pmatrix}0 & 1\\ \\ 0 & 0\end{pmatrix}\begin{pmatrix}\xi_\Sigma\\ \\ \xi_\Lambda\end{pmatrix}, \tag{4.58}$$

which means that a perturbation in the Λ causes Σ to grow linearly, i.e., a perturbation in lambda behaves as an external field ($\bar{h}$). Thus, an initial burst, such as the beginning of the spreading experiments, yields $\dot{\Sigma} = \bar{h}$ and $\Sigma(\bar{t}) = h\bar{t}$ ($\bar{t}$ indicates the beginning of the experiment, not to be mistaken by the time t). This initial deterministic growth results in the anomalous value of η. The number of active sites is capped by the "volume" of the system ($L^{d_c} \sim T^{d_c/2}$) and proportional to the density of active sites, which means that $N(t) = \Sigma(t)\sqsubseteq\!\wr\!\updownarrow(t)$. Considering $d_c = 4$, $\sqsubseteq\!\wr\!\updownarrow(t) \sim t$; therefore, we conclude that $N(t) \sim \Sigma(t)t \sim t^2$ and $\eta = 2$.

In summary, the T_5 transition poses as an unknown universality class that we named Hopf Tricritical Directed Percolation (H+TDP). In its mean-field form, this transition has different exponents from the other quiescent-active continuous transitions we explored in this chapter (Table 2), violates at least one scaling relation, has an uncommon spreading exponent, and produces asymmetrical avalanche shapes, as we will show in Sec. 4.10.

4.8 HOPF-TRANSCRITICAL BIFURCATION.

In case C, as we increase w_{EE}, the first tricritical point is the Hopf transcritical bifurcation, a codimension 2 bifurcation that comprises the collision between the curve of Hopf and trascritical bifurcations (see Fig. 27). There lies the continuous transition T_6. A key characteristic of this transition is that, independently of the initial condition, the trajectories decay to the quiescent state through region II. In this transition, the Hopf bifurcation overrides the transcritical bifurcation eliciting frustrated oscillations. These frustrated oscillations drive the system toward the switching manifold and, thus, into region II. Once in region II, the excitatory density decays exponentially and drags the system to quiescence without power law behavior, i.e., the dynamic exponent θ is ill-defined for T_6 (see Fig. 34c).

Although the dynamic exponent is not well-defined, the dynamic equations should allow

Figure 34 – Hybrid transition (T_6): Hopf-transcritical bifurcation. (a) Steady-state solution as a function of the distance to transition value $\Delta = w_{EE} - w_{EE}^{HT}$ for three values of constant external field h, in black $h = 0$, in a darker orange dashed curve $h = 0.01$, and in a lighter orange dash-dotted curve $h = 0.1$. Observe that in this transition the introduction of an external field turns the transition into a discontinuous one rather than smoothing it out. The blue dashed straight line represents the static exponent $\beta = 1$. (b) Steady-state solution as a function of the external field h at the Hopf-transcritical bifurcation at $\Delta = 0$ in black with the shaded area describing coexistence. (c) Exponential time decay. (d) Survival probability of simulation with Gillespie's algorithm for two system sizes, $N = 10^8$ in black and $N = 10^{10}$ in gray, and, as a guide to the eye, a dashed straight line that represents the spreading exponent $\delta = 1$. The system is plot at parameters: $\alpha = 1$, $w_{II} = 0$, $w_{EI} = 0.8$, $w_{IE} = 1.25$, and $w_{EE} = 2$.

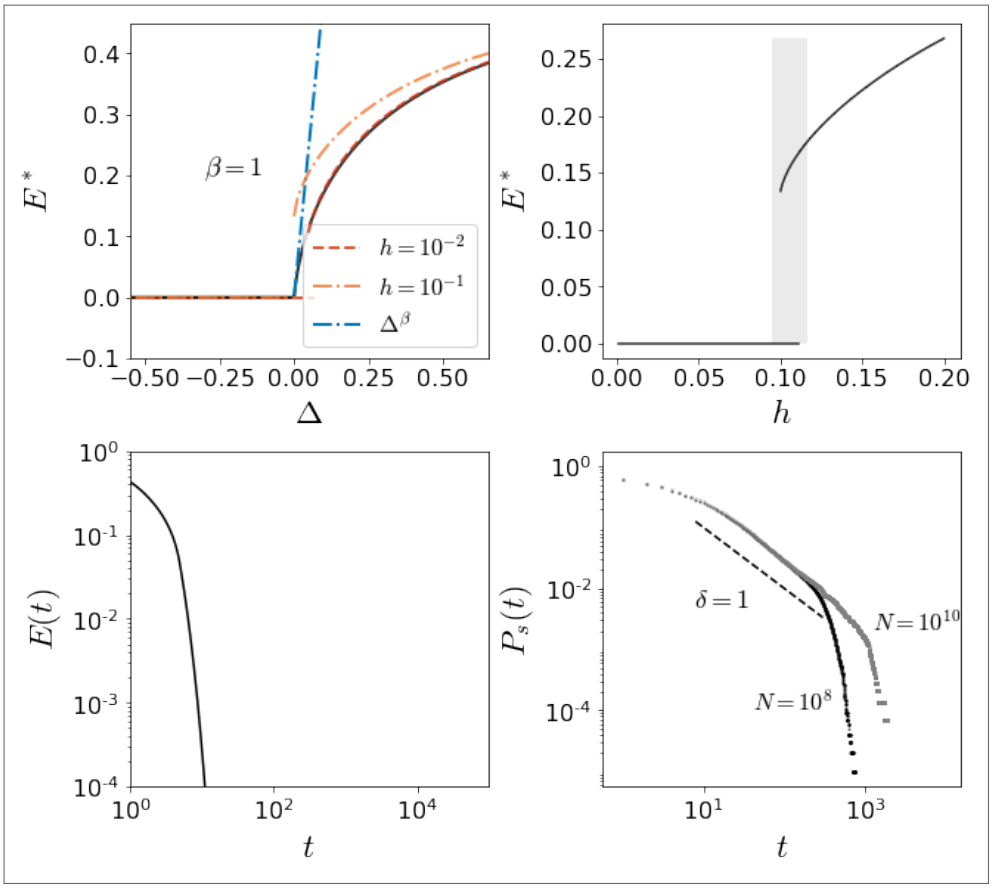

Source: The author (2023)

us to predict the static exponents. At the possible critical point, considering the parameters at the transition given by Eq. (4.18) and Eq. (4.19) and $\Delta = w_{EE} - w_{EE}^{HT} = 0$, we rewrite Eq. (4.39),

$$E^*(\Delta; h = 0) \approx \frac{\alpha + w_{II}}{(\alpha + w_{II} - w_{IE})}\Delta + \mathcal{O}(\Delta^2) \ , \tag{4.59}$$

which yields $\beta = 1$ (see Fig. 34a). This result is true for $h = 0$, i.e., in the absence of an external field, because as the system evolves into the supercritical regime the emergence of an active state attracts all trajectories pulling them away from region II. However, one of the key characteristics of a bona fide critical point is that the introduction of an external field smooths out the transition, which is not what we observe in Fig. 34a. The transition becomes

discontinuous, instead, for $h \neq 0$.

If we followed the procedure for the other transitions, the static exponent related to the external field should come from

$$E^*(h; \Delta = 0) \approx \sqrt{\frac{[(w_{II} + \alpha)^2 - \alpha w_{IE}]h}{\alpha w_{IE}[w_{IE} - w_{II} - \alpha]}} + \mathcal{O}(h) \ , \tag{4.60}$$

which would yield $\delta_h = 2$. However, the condition for phase diagrams like that of case C is $w_{IE} < w_{II} + \alpha$ (see Sec. 4.1). Therefore, Eq. (4.60) is misleading because the denominator is negative inside the square root, making the solution imaginary and not a real solution to our system. This solution is misleading due to the *naive* linearization of the dynamical equations, where we only consider the non-vanishing part of the response function Φ. Thus far, this naive linearization has not failed; however, the Hopf bifurcation drives the system away from region I. In a nutshell, for Eq. (4.60) and $\Delta = 0$, the asymptotical dynamics fall into region II, which means that the quiescent state is a global attractor as h increases up to a discontinuous transition in a saddle-node bifurcation (see Fig. 34b). In this hybrid transition, the static exponent δ_h is not well-defined.

Figure 35 – Mean number of particles $N(t)$ in spreading experiments for the transitions T_1, T_5, and T_6. Simulations with the same parameters as Fig. 22 with $N = 10^8$. As seen in Fig. 33, T_1 shows regular mean-field scaling as $\eta = 0$. However, for T_5 and T_6, the Bogdanov-Takens-like linear dynamics yields the unusual result $\eta = 2$.

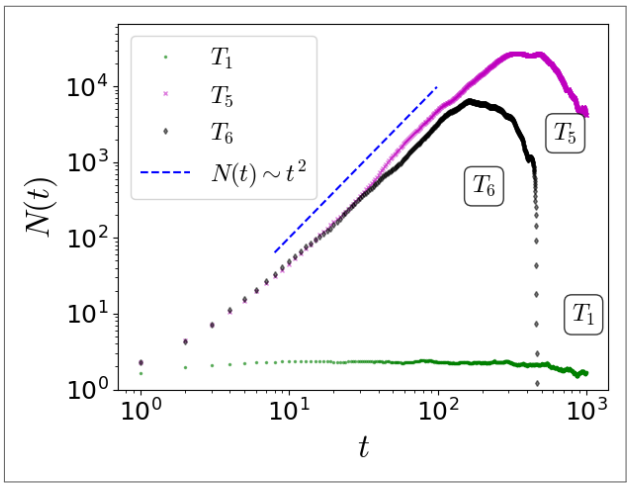

Source: The author (2023)

Similarly to what we observed in the Hopf tricritical directed percolation universality class, the T_6 transition has a higher sensitivity to system size. The survival probability decays in time with $\delta = 1$, as seen in Fig. 34d, as in all other continuous transitions. Regarding the instantaneous number of active sites, this transition displays the same Jacobian matrix, i.e.,

the normal form of a Bogdanov-Takens, which yields the same spreading exponent $\eta = 2$ (see Fig. 35).

Briefly, T_6 exhibits a mixture of signatures of continuous and discontinuous transitions and, thus, it is, surprisingly, a hybrid transition, does not belong to any standard type of quiescent-active universality class, and cannot be classified as a bona fide critical point.

4.9 CONTINUOUS TRANSITIONS FROM QUIESCENT-EXCITABLE TO ACTIVE STATES

The other types of hybrid transitions in case C between the quiescent excitable and active state T_7 and T_8 (see Fig. 27). Observe that for these cases, similarly to T_6, the trajectories

Figure 36 – Hybrid transition (T_7): discontinuity-induced bifurcation. (a) Steady-state solution as a function of the distance to transition value $\Delta = w_{EE} - w^*_{EE}$ for three values of constant external field h, in black $h = 0$, in a darker orange dashed curve $h = 0.01$, and in a lighter orange dash-dotted curve $h = 0.1$. In this transition, similar to T_6 the introduction of an external field turns the transition into discontinuous. The blue dashed straight line represents the static exponent $\beta = 1$. (b) Steady-state solution as a function of the external field h at the discontinuity-induced bifurcation, $\Delta = 0$, in black with the shaded area describing coexistence. (d) Survival probability of simulation with Gillespie's algorithm, where we observe, surprisingly, plateaus followed by decays. The system is plot at parameters: $\alpha = 1$, $w_{II} = 0$, $w_{EI} = 0.8$, $w_{IE} = 1.35$, and $w_{EE} = 2.08$.

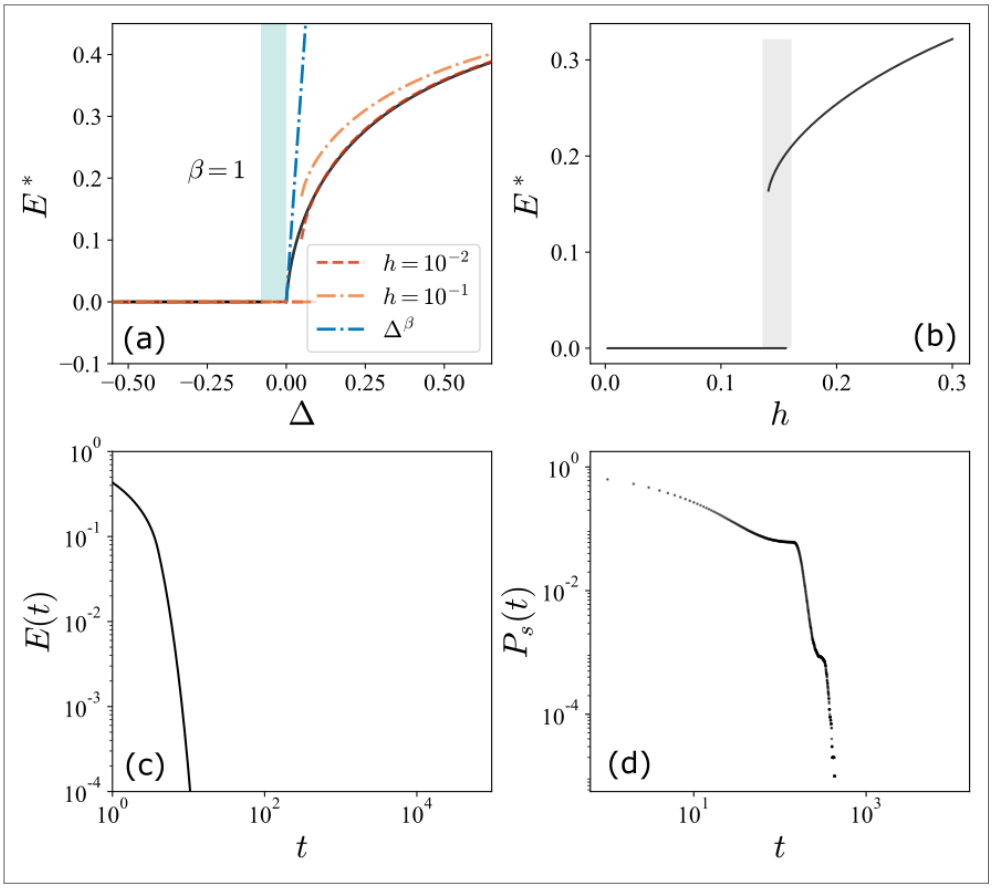

Source: The author (2023)

asymptotically decay through region II independent of the initial condition because the system is transitioning from or to the excitable quiescent phase.

The naive linearization of the quiescent excitable state (assuming $\Phi > 0$) produces a complex eigenvalue with $\mathrm{Im}(\lambda) \neq 0$, eliciting frustrated oscillations, driving the trajectories into regions II and III, and ensuring the global stability of the quiescent state (Fig. 21a). Both transitions go through a discontinuity-induced transition (black dashed lines in Fig. 27), i.e., they depend on the relative sizes of the basin of attraction of the region inside the switching manifolds and the active state. Increasing the strength of the parameter w_{EE} causes the active state to move away from the switching manifolds and pull more trajectories to it. T_7 goes from excitable quiescent to active phase normally and T_8 goes through a tricritical point,

Figure 37 – Hybrid transition (T_8): tricritical discontinuity-induced bifurcation. (a) Steady-state solution as a function of the distance to transition value $\Delta = w_{EE} - w^*_{EE}$ for three values of constant external field h, in black $h = 0$, in a darker orange dashed curve $h = 0.01$, and in a lighter orange dash-dotted curve $h = 0.1$. In this transition, similar to T_6 and T_7, the introduction of an external field turns the transition into discontinuous. The blue dashed straight line represents the static exponent $\beta = 1/2$. (b) Steady-state solution as a function of the external field h at the collision between the discontinuity-induced bifurcation and the saddle-node, $\Delta = 0$, in black with the shaded area describing coexistence. (d) Survival probability of simulation with Gillespie's algorithm, where we observe, like T_7 (Fig. 36), plateaus followed by a fast decay. The system is plot at parameters: $\alpha = 1$, $w_{II} = 0$, $w_{EI} = 0.8$, $w_{IE} = 1.5625$, and $w_{EE} = 2.25$.

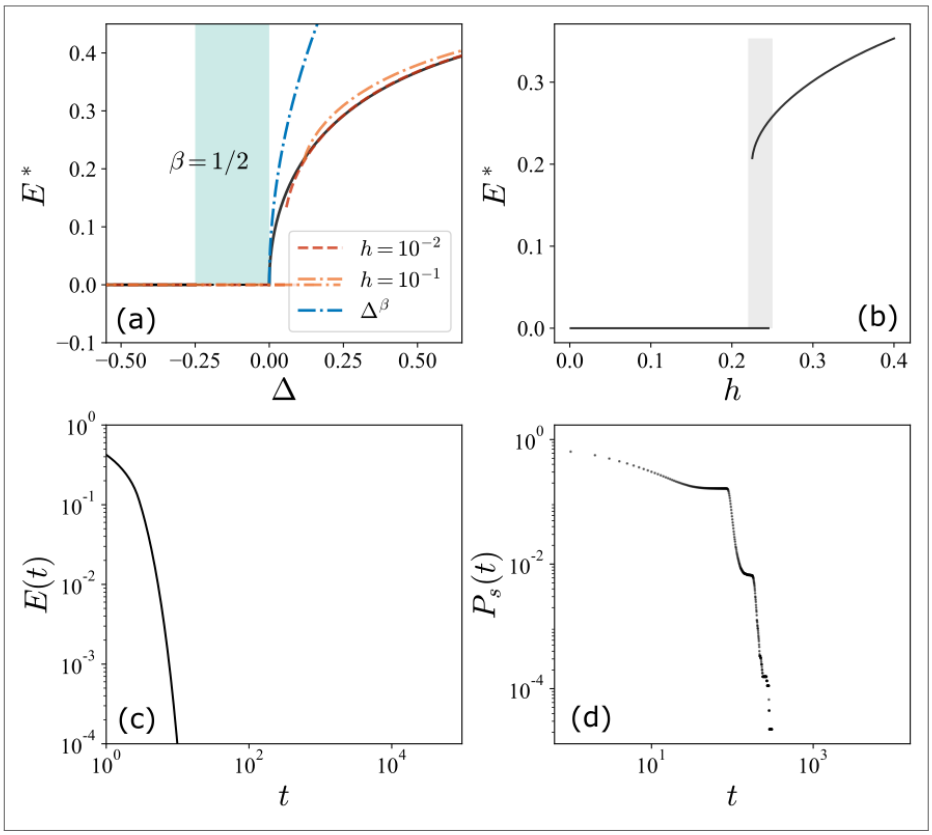

Source: The author (2023)

which means they are the counterparts of T_1 and T_2, respectively, for the excitable quiescent phase. The discontinuity-induced bifurcation nearly coincides with the *continuation* of the transcritical bifurcation, since the emergent active state attracts the trajectories away from region II.

Since these transitions have a counterpart in the continuous transitions of case A, we observe that Eq.(4.39) and Eq. (4.45) hold for T_7 and T_8, respectively. These solutions yield a continuous curve with the control parameter and define with $\beta = 1$ for T_7 and $\beta = 1/2$ for T_8 (see Fig. 36a and 37a). The introduction of the external field, however, turns the seemingly continuous transitions into discontinuous. And, using the logic that we used for T_6 and looking at Eq. (4.40) and Eq. (4.46), the denominators at the transition in case C are negative, the solution is complex, the system asymptotically reaches region II, and exponentially decays to quiescence. Therefore, the static exponent δ_h is ill-defined for both transitions and there is a discontinuous jump in the stationary solution (or order parameter) as a function of the external field h caused by the forcibly global stability of the quiescent state (Figs. 36b and 37b).

Figure 38 – Mean number of particles $N(t)$ in spreading experiments for the transitions T_7 and T_8. Simulations with the same parameters as Fig. 22. The behavior of this observable in these transitions is surprisingly oscillatory, it starts with a sharp growth that fades into an oscillation.

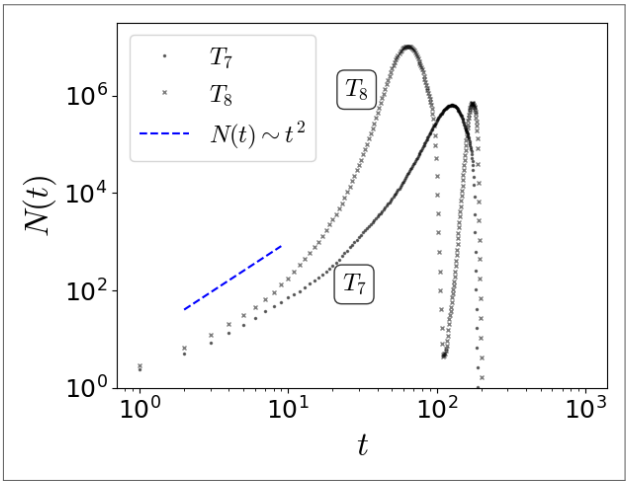

Source: The author (2023)

Regarding the dynamic exponent on both transitions, the asymptotic dynamics of the time decay is exponential for both hybrid transitions, as illustrated in Fig. 36c, for T_7, and in Fig. 37c, for T_8. On spreading exponents, the overall behavior of the survival probability displays intermediate plateaus along the decay (Fig. 36d and Fig. 37d). These plateaus possibly stem from the phantom of the emerging active state that starts to pull on the trajectories before they fall into region II, where the quiescent state is the only attractor. Observe that for these

transitions, the Jacobian matrix is not the normal form of a Bogdanov-Takens and, although in many ways similar to T_6, the spreading exponent η is expected to behave as normal, i.e., $\eta = 0$. However, for these hybrid transitions, the spreading exponent η is also ill-defined (see Fig. 38), similarly to T_5 and T_6, they have an initial growth but it is not deterministic and as time progresses the behavior assumes an oscillatory quality that we leave the explanation for further research.

In conclusion, the T_7 and T_8 transitions exhibit a mixture of features of continuous and discontinuous phase transitions, albeit not as strongly as T_6.

4.10 AVALANCHE DYNAMICS

4.10.1 Avalanche size and duration distributions

A signature of criticality, which is well-known and widely used in neuroscience, is the power law nature of avalanche statistics. This quantity is helpful when comparing model data with experimental data, and when trying to classify experimental data into a universality class. Aided by the computed exponents and the scaling relations, Eq. 4.33, Eq. 4.34, as well as the crackling noise relation (Eq. 4.35), we find and confirm the avalanche exponents for the three bona fide critical points: T_1, T_2, and T_5.

The consistency of the transition T_1 with the directed percolation universality class comes two-fold. At the transition, explored in Sec. 4.3, we observe that: (i) $\delta = 1$ and Eq. 4.34 yields $\tau_t = 2$; (ii) $\eta = 0$ and Eq. 4.33 yields $\tau = 3/2$; and (iii) Eq. 4.35 yields $\gamma = 2$. These exponents are consistent with mean-field directed percolation; however, to further confirm them we compute them by simulating the stochastic system with Gillespie's algorithm and computing these quantities as seen in the distributions of sizes S, durations T, and average sizes as a function of durations in Fig. 39a, Fig. 39d, and Fig. 39g, respectively.

The avalanche statistics for the tricritical directed percolation have not yet been confirmed through simulation. However, in a general analysis and with the scaling relations, we are able to compute the same exponents. Since $\delta = 1$ and $\eta = 0$, the avalanche exponents of the tricritical case should be the same as for the regular one: (i) $\tau = 3/2$, (ii) $\tau_t = 2$, and (iii) $\gamma = 2$; These values are further confirmed by numerical simulations, analogous to the analysis for T_1, in Fig. 39b, Fig. 39e, and Fig. 39h. It is noteworthy that these exponents are the same as directed percolation; therefore, from this analysis alone, these two universality classes

Figure 39 – Avalanche analysis. Simulations using Gillespie's algorithm for the same parameters as in Fig. 22 and network size $N = 10^8$. In this case, we report results only for true (or bonafide) continuous phase transitions, for which scale-free avalanches emerge, i.e., T_1, T_2, and T_5. For the T_1 transition, one obtains results as expected for DP: (a) $\tau \approx 3/2$, (d) $\tau_t \approx 2$, and (g) $\gamma \approx 2$. For T_2, the system behaves consistently with TDP: (b) $\tau \approx 3/2$, (e) $\tau_t \approx 2$, and (h) $\gamma \approx 2$, i.e., TDP and DP share the same avalanche exponents. Finally, for the T_5 transition, (c) $\tau \approx 5/4$, (f) $\tau_t \approx 2$, and (i) $\gamma \approx 4$. The exponents τ and τ_t were obtained with the Maximum Likelihood Estimator (MLE) method (DELUCA; CORRAL, 2013).

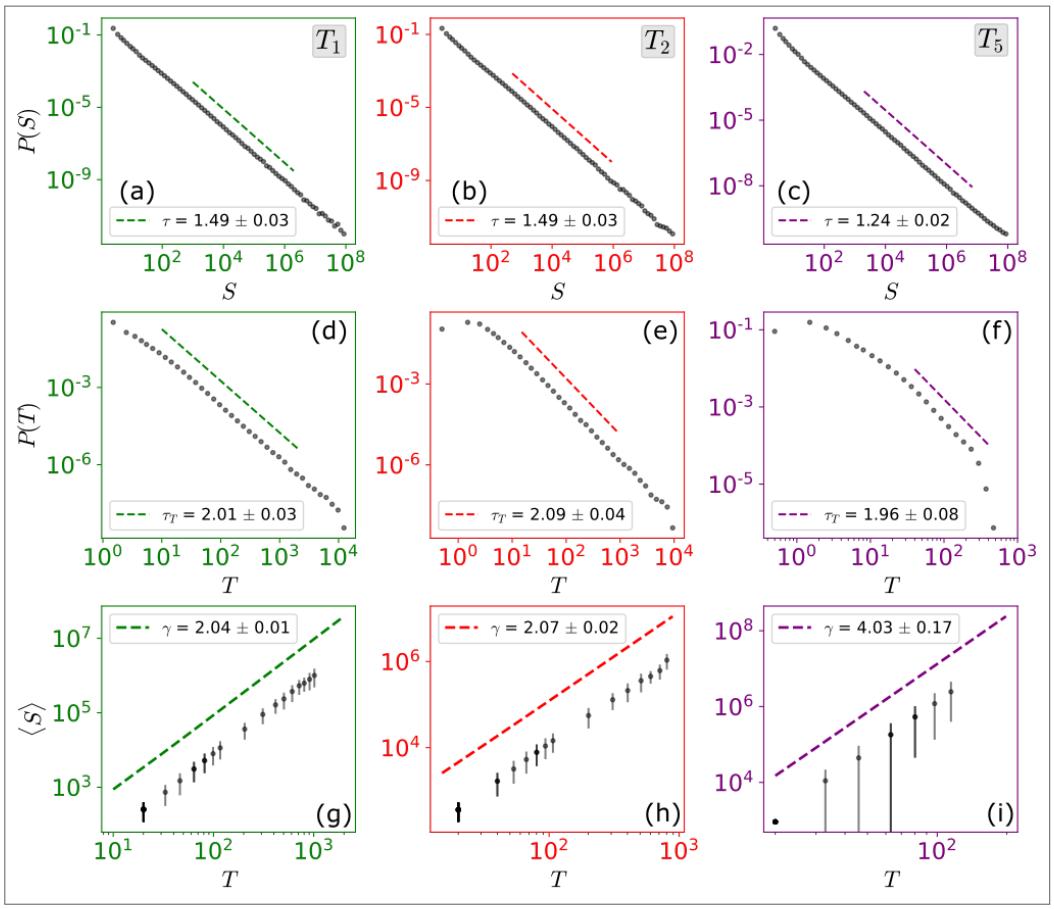

Source: (PIUVEZAM et al., 2023)

are indistinguishable. One could argue that the probability is in favor of the standard directed percolation as it is more widespread and less restrictive in parameters (e.g., in this study, it has a lower co-dimension). That said, the exponents are the same and the distribution themselves cannot distinguish them.

The Hopf tricritical directed percolation universality class differs from the aforementioned classes because its number of active sites scales with $\eta = 2$, even if the other spreading exponent δ behaves as usual (see Sec. 4.7). Given this anomalous value, the scaling relations predict different values for τ and γ: (i) Eq. (4.33) predicts $\tau = 5/4$, (ii) Eq. 4.34 predicts $\tau_t = 2$, and (iii) Eq. 4.35 predicts $\gamma = 4$. Besides verifying these results numerically in Fig. 39c, Fig. 39f, and Fig. 39i, the crackling noise and the scaling cutoff of S for different

Figure 40 – Conditional Probability. (a) The conditional probability, $P(S|T)$, collapses into one curve when we set $\gamma = 4.0$ for the Hopf Tricritical Directed Percolation (T_5). (b) In contrast, for $\gamma = 2.0$ there is no collapse. Furthermore, on the inset, one observes that the peaks of $P(S|T)$, S^*, scale with $S^* \sim T^\gamma$, for $\gamma = 4.0$. (c) The cutoff for size and duration distributions scaling with γ (CHESSA et al., 1999; DICKMAN; CAMPELO, 2003). Simulations with Gillespie's algorithm for the same parameters as Fig. 22; for (a) and (b), $N = 10^8$; and, for (c), $N = [10^4, 10^5, 10^6, 10^7, 10^8]$.

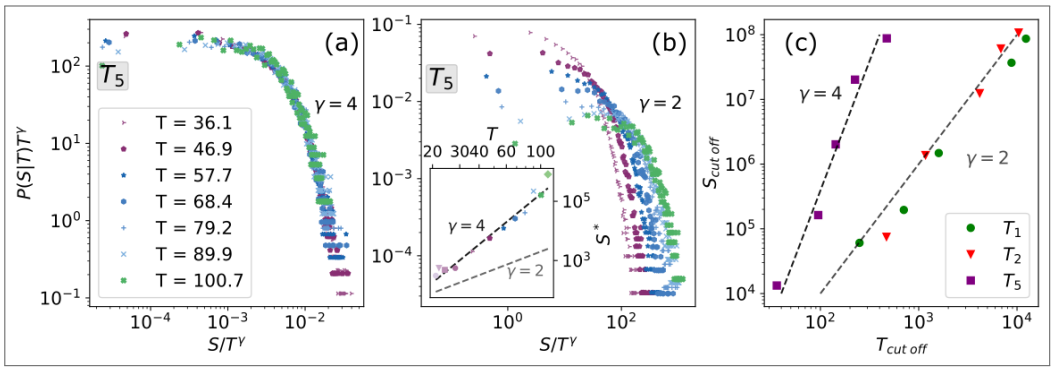

Source: (PIUVEZAM et al., 2023)

system sizes also give us further tests of consistency (CHRISTENSEN; FOGEDBY; JENSEN, 1991; CHESSA et al., 1999; DICKMAN; CAMPELO, 2003). When analyzing $P(S|T)$, we would expect that $P(S|T)T^{\gamma-1}$ scales with S/T^γ and, at Fig. 40a and Fig. 40b, we observe an excellent data collapse. On the cutoffs, we observe a clear difference between the cases of, on the one hand, T_1 and T_2, where $\gamma = 2$ and T_5, on the other hand, where $\gamma = 4$ (see Fig. 40c). Also, consistently with the scaling relation $\tau_t = \delta + 1$, the avalanche distribution of durations scales with the same exponent as in DP and TDP, $\tau_t = 2$ (Fig. 39f). An overview of the set of exponents for the three bona fide critical transitions is in Table 2.

Table 2 – Summary of exponents in the Wilson-Cowan Model

	DP	TDP	H+TDP
Codim.	1	2	3
$\boldsymbol{\beta}$	1	1/2	1/2
$\boldsymbol{\delta}_h$	2	3	2
$\boldsymbol{\theta}$	1	1/2	1
$\boldsymbol{\delta}$	1	1	1
$\boldsymbol{\eta}$	0	0	2
$\nu_\parallel$	1	1	1
$\boldsymbol{\tau}$	3/2	3/2	5/4
$\boldsymbol{\tau}_t$	2	2	2
$\boldsymbol{\gamma}$	2	2	4

Source: (PIUVEZAM et al., 2023)

4.10.2 Mean temporal profile of avalanches

The scaling of the mean avalanche shape (also called *mean temporal profile of avalanches*) is also a widely used signature of criticality in non-equilibrium systems with absorbing states (PAPANIKOLAOU et al., 2011). The mean temporal profile of avalanches observes that when averaged and normalized using critical exponents, the shape of avalanches of different sizes and durations collapses onto a single curve,

$$\rho(t;T) \sim T^{\gamma-1}\mathcal{F}(t/T). \tag{4.61}$$

For standard processes with absorbing states, the averaged shape of avalanches with different durations and sizes collapses onto a universal curve that typically has a symmetric inverted parabolic form (FRIEDMAN et al., 2012).

Figure 41 – Skewness and mean temporal profile of avalanches. (a,d) Schematic representations of where the system is sitting for the avalanche shape analysis. (b) Shape-collapse of the mean temporal profile for several critical values in Case A as the system approaches the tricritical point. (c) The skewness of these curves slightly decreases with the eigenvalue λ_-. (d) Considering a change in w_{IE}, the phase diagram goes from case A to case B. (e) On the tricritical point, the shape-collapse deforms approaching the H+TDP transition. (f) The skewness as a function of λ_-. Simulations with Gillespie's algorithm for the same parameters as Fig. 22 and $N = 10^8$.

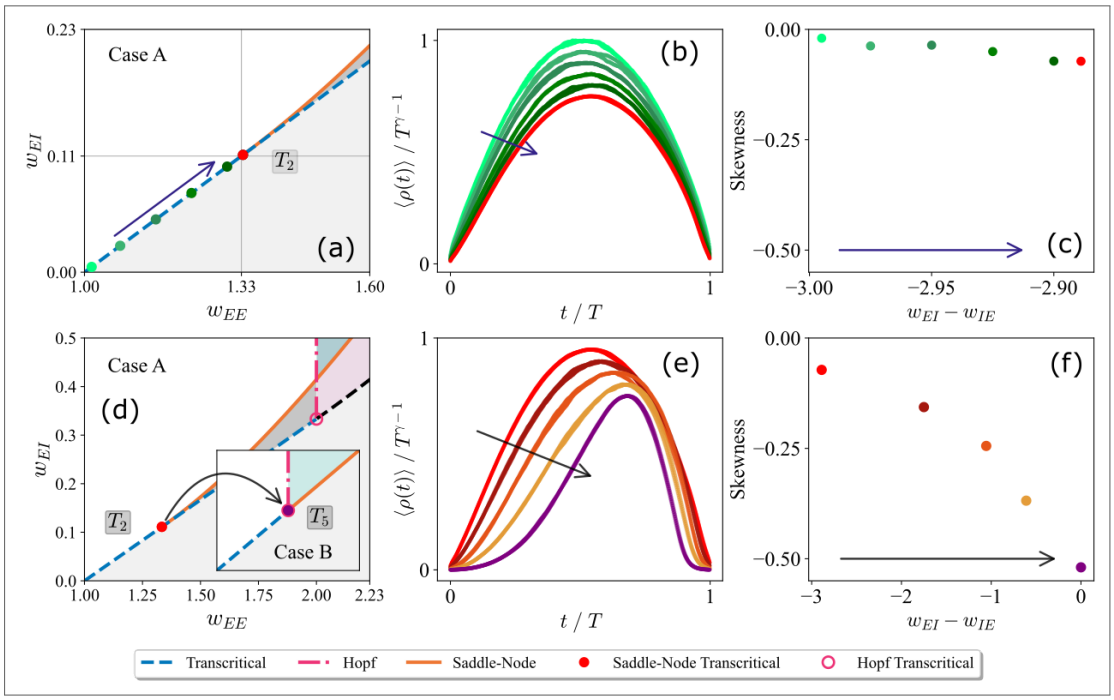

Source: (PIUVEZAM et al., 2023)

Indeed, the averaged avalanche shape throughout the T_1 curve is approximately an inverted parabola (see Fig. 41a and Fig. 41b). The shapes collapse for different durations with $\gamma = 2$,

and as they approach the tricritical point the inverted parabola starts showing a slight skew (or asymmetry). The symmetric inverted parabolas shown in these mean-temporal profiles of avalanches is a consequence of time-reversal symmetry (MILLER; YU; PLENZ, 2019); therefore, it follows that the asymmetry, when found, reflects a break in that symmetry (LAURSON et al., 2013; LÓPEZ; BUENDÍA; MUÑOZ, 2022). Interestingly, when the system follows the T_1 curve towards T_2 in case A, the mean temporal profile gets increasingly more asymmetric, though only slightly when quantified by the increase in the absolute value of skewness (Fig. 41c). This behavior has been observed and confirmed in other studies (CANDIA et al., 2021; LÓPEZ; BUENDÍA; MUÑOZ, 2022; NANDI et al., 2022), which shows that the introduction of an inhibitory population causes a small tilt on the mean temporal profile in systems belonging to the directed percolation universality class.

Conversely, while studying the systems at T_2 and evolving the parameters from case A to case B (Fig. 41d), the avalanche mean temporal profile skews progressively. This progression in its skewness reaches a maximal absolute value (or asymmetry) at the Hopf tricritical directed percolation transition (Fig. 41e). Observe that, in Fig. 41c, the decay is slower and the value remains somewhat fixed; however, in Fig. 41e, the drop is steeper. These results should provide further aid in comparing theoretical with experimental results.

5 CONCLUSIONS AND PERSPECTIVES

Throughout this thesis, we have rigorously examined all potential phase transitions between active and quiescent phases within the stochastic Wilson-Cowan model. This meticulous investigation entailed detailed scaling analyses by studying the dynamic mean-field equations and numerical simulations of the microscopic model.

In the absence of an external field, the model exhibits the standard quiescent and active phases separated by phase transitions. A novel feature of the model uncovered in this thesis is the addition of a new quiescent phase, the *excitable quiescent* phase. This phase appears because of the piecewise smooth nature of the response function. The dynamical model notably features Hopf bifurcations. On one side of this bifurcation, the state (or fixed point) is a stable focus, i.e., independently of the piecewise nature of the response function the system relaxes to it, which falls under the category of standard quiescent. On the other side of this bifurcation, the state is a locally unstable focus and the trajectories are, at first, repelled by the quiescent state; and, as they reach the switching manifolds, relax towards it because of the shift in dynamics, falling under the new category called excitable quiescent. The presence of foci means the eigenvalues are complex, eliciting oscillations. However, these pseudo-oscillations are "frustrated" when the system crosses over to inhibition-dominated regions of the state space (region II or region III), where the trajectories relax to zero exponentially. In this regime, small perturbations close to quiescence are transiently amplified before the exponential decay, hence the name "excitable quiescent" phase (or also "reactive" phase, see (ASSIS; COPELLI, 2009; BENAYOUN et al., 2010; HIDALGO et al., 2012; SANTO et al., 2018; PINTO; COPELLI, 2019; GUDOWSKA-NOWAK et al., 2020)).

In between the quiescent and excitable quiescent is a curve of Hopf bifurcations; in between the active and standard quiescent phases is a curve of transcritical bifurcations; and, in between the active and excitable quiescent state is a curve of discontinuity-induced bifurcations. The curve of saddle-node bifurcations delineates the bistable regions. And from any of the quiescent phases to the active phase, we observe *eight* different transitions. The types of these phase transitions are: second-order (or continuous) — which, when between standard quiescent and active, we proved to belong to the mean-field directed percolation class; first-order (or discontinuous) displaying hysteresis; a tricritical point — which, when between standard quiescent and active, belongs to the tricritical directed percolation universality class (LÜBECK,

2006; HENKEL; HINRICHSEN; LÜBECK, 2008; ÓDOR, 2008); and, surprisingly, hybrid, where some transitions close to or involving the excitable quiescent phase display characteristics of both second- and first-order transitions. The presence of an excitable quiescent phase stems from the existence of an inhibitory field. The other more common features, such as directed percolation and tricritical directed percolation, appear in simpler models containing only excitatory populations. Therefore, without the inhibitory activity, a model fails to display this unique set of possible phase transitions.

Analyzing the dynamics of the Wilson-Cowan model and its stochastic counterpart, we observed that there are three distinct cross-sections of a three-dimensional phase diagram. These cross sections are themselves two-dimensional phase diagrams with the parameters $[w_{EE}, w_{EI}]$ as variables (seen in Fig. 22). The third parameter, w_{IE}, controls the position of the Hopf bifurcation curve with respect to the tricritical point, characterizing the cases A, B, and C. Across the three cases in the phase diagrams, we found 8 types of transitions, labeled T_1, T_2, ..., and T_8, in Fig. 25, Fig. 26, and Fig. 27.

The first three transitions are commonly found in many models, which present active and quiescent phases. Their mean-field version has a counterpart in low-dimensional dynamical analysis: (i) mean-field directed percolation (MF-DP) – second-order phase transition (T_1) – corresponds to a transcritical bifurcation; (2) mean-field tricritical directed percolation (MF-TDP) – also second-order (T_2) – corresponds to a saddle-node transcritical bifurcation; and (iii) a discontinuous transition with hysteresis (or bistability) – first-order (T_3) – corresponds to a saddle-node bifurcation.

Our findings in the well-known and widely explored directed percolation transition (T_1) in the stochastic Wilson-Cowan are congruent to the results of CANDIA et al. (2021). When choosing the parameter reduction $w_E \equiv w_{EE} = w_{IE}$ and $w_I \equiv w_{EI} = w_{II}$, the system is poised at the transcritical bifurcation for $w_E - w_I = \alpha$ (for full parameters: $w_{EE} = \alpha + w_{EI}w_{IE}/(\alpha + w_{II})$), which is the condition they reported necessary for criticality. Similarly, our results reproduce the tricritical directed percolation class (T_2), as first described in LÜBECK (2006). Other recent works have found a tricritical point in neuronal models with a population of inhibitory units (LÓPEZ; BUENDÍA; MUÑOZ, 2022; ALMEIRA et al., 2022). In this cluster of well-known and studied transitions, on the other side of the tricritical point is a discontinuous transition featuring hysteresis (LÜBECK, 2006; ASSIS; COPELLI, 2009). It is noteworthy that in this work we have shown that the avalanche exponents at both T_1 and T_2 continuous transitions follow the well-known values: $\tau = 3/2$, $\tau_t = 2$, and $\gamma = 2$ so that they alone cannot be used

to distinguish between the two transitions. One can rightfully point out that the directed percolation class is probabilistically easier to find due to its lower codimension. However, this observation gives margin for further investigation, since the avalanches themselves behave the same.

The transitions between the excitable quiescent and active phases have a similar distribution of types. For all cases, the discontinuous transition is T_4 displaying an excitable bistability (coexistence of the excitable quiescent and the active phases). In case C, the transcritical bifurcation between quiescent and active (T_1) has a counterpart in the discontinuity-induced bifurcation, labeled T_7; and the tricritical point is T_8, in this case, where the T_4 curve of transitions change into T_7. The transitions T_7 and T_8, for being counterparts of two continuous transitions and exhibiting a continuous growth from zero in the absence of an external field, seem to be continuous at first glance. However, their response to an external field is anomalous because, when we introduce an external field the transition becomes discontinuous. The excitability of the quiescent state distorts the trajectories, i.e., a small excitable external input drives slightly active states to quiescence. These hybrid transitions have the static critical exponent β but the other static exponent δ_h, the dynamic exponent θ, and the spreading exponents δ and η are all ill-defined.

The Hopf bifurcation is directly involved in two transitions, which corresponds to higher-codimension bifurcations. When the Hopf meets the transcritical bifurcation, we observe a hybrid transition labeled T_6; and, when this Hopf-transcritical bifurcation finds a saddle-node in a tricritical point (only possible in case B), we find a novel continuous transition, which we call the Hopf tricritical directed percolation (T_5).

Similarly to the other aforementioned hybrid transitions, the T_6 transition also involves the excitable quiescent phase, and the introduction of an external field also results in a discontinuous transition. Therefore, the static exponent δ_h is ill-defined along with the dynamic exponent θ. The other static exponent, β (calculated at $h = 0$), is well-defined and so are the spreading exponents, characterizing this transition as a hybrid.

The Hopf tricritical directed percolation transition (T_5) is the main novelty of the present work. It corresponds to a codimension-3 bifurcation, where the Hopf curve collides with the saddle-node transcritical bifurcation at a tricritical point. Both eigenvalues vanish at this transition so that the Jacobian matrix of the transition takes the normal form of a Bogdanov-Takens bifurcation. In analyzing the system's scaling, we observe its behavior at the critical point and slightly in the supercritical regime the strictly upper triangular matrix strongly

influences these behaviors resulting in the violation of scaling relations. In particular, it violates the relation $\theta = \beta/\nu_{\parallel}$, since its static exponents are $\beta = 1/2$ and $\delta_h = 1/2$ and its dynamic exponent is $\theta = 1$. A similar break in scaling relations was recently observed by NOH; PARK (2005b), also involving a second inhibitory field.

A common feature of mean-field scaling is the vanishing of the spreading exponent driving the growth of the total number of particles (η) because it regards the perturbative corrections to mean-field behavior (MUÑOZ; GRINSTEIN; TU, 1997). However, this exponent does not vanish for the T_5 transition ($\eta = 2$), even when considering the mean-field approximation. This anomaly in scaling, coupled with the broken scaling relation, yields different avalanche exponents. The duration exponent holds as $\tau_t = 2$, since it depends solely on the survival exponent, and is consistent with MF-DP and MF-TDP. Conversely, the size exponent, $\tau = 5/4$, and the crackling noise exponent, $\gamma = 4$, diverge from the known ones.

Standard models within the directed percolation universality class exhibit symmetry in the average temporal profile of avalanches, resembling inverted parabolas. This symmetry, demonstrated by the convergence of average avalanche shapes, reveals time-reversal invariance (LAURSON et al., 2013; MILLER; YU; PLENZ, 2019). Conversely, the mean temporal profile in the Hopf tricritical directed percolation displays a notable asymmetry, which we quantified through its negative skewness. Recent work has shown that this tilt in the symmetric mean temporal profiles results from introducing an inhibitory field into models in directed percolation universality class (CANDIA et al., 2021; LÓPEZ; BUENDÍA; MUÑOZ, 2022; NANDI et al., 2022). Our results further suggest that not only does the strength of the inhibitory coupling slightly skew the average temporal profiles, but the combination of the proximity to the excitable quiescent phase and the onset of frustrated oscillations further prompts more pronounced distortions. This asymmetry in the avalanche mean temporal profile provides a useful tool to assess the proximity to a transition belonging to the Hopf tricritical directed percolation, considering the inherent difficulties of evaluating the exponents from experimental data. This is especially beneficial when considering the inherent challenges involved in evaluating these exponents from experimental data.

Our research thoroughly delves into the Hopf tricritical directed percolation universality class within the context of the stochastic Wilson-Cowan model under a mean-field approximation. Studying the model in a different network should lead to the investigation of these transition behaviors across various dimensions. In particular, the nature of the transition might exhibit subtle variations when examining it on a sparser network (BRUNEL, 2000b; BUENDíA et

al., 2019); since the presence of enhanced stochastic effects from the finite connectivity causes substantial changes in dynamics and gives rise to new phenomena. Moreover, the introduction of heterogeneity to the network potentially leads to Griffiths phases (MUÑOZ et al., 2010; MORETTI; MUÑOZ, 2013; ODOR, 2016) Nevertheless, there remains a need for a more systematic field-theoretical analysis of the Hopf tricritical directed percolation universality class.

At last, the work studying subsampling effects on avalanche exponents shows that the brain could reasonably be operating just below and at the critical point, when comparing the experimental data in Fontenele et al. (FONTENELE et al., 2019) to the data of a model belonging to MF-DP and subsampling it (CARVALHO et al., 2021; LOTFI et al., 2021). Considering that the exponents of MF-DP are the same as MF-TDP, does the subsampling of the model at the MF-TDP transition also replicate experimental data? Furthermore, does the subsampling at the novel transition also replicate experimental data? These are some of the open questions prompted by the results herein for future investigation.

REFERENCES

ALMEIRA, J.; GRIGERA, T. S.; CHIALVO, D. R.; CANNAS, S. A. Tricritical behavior in a neural model with excitatory and inhibitory units. *Physical Review E*, v. 106, n. 5, p. 054140, 2022.

APICELLA, I.; SCARPETTA, S.; ARCANGELIS, L. de; SARRACINO, A.; CANDIA, A. de. Power spectrum and critical exponents in the 2d stochastic wilson–cowan model. *Scientific Reports*, v. 12, n. 1, p. 1–13, 2022.

ASSIS, V. R.; COPELLI, M. Collective behavior of coupled nonuniform stochastic oscillators. *Physica A: Statistical Mechanics and its Applications*, v. 391, n. 4, p. 1900–1906, 2012. ISSN 0378-4371. Disponível em: <https://www.sciencedirect.com/science/article/pii/S0378437111007916>.

ASSIS, V. R. V.; COPELLI, M. Discontinuous nonequilibrium phase transitions in a nonlinearly pulse-coupled excitable lattice model. *Phys. Rev. E*, v. 80, p. 061105, 2009. Disponível em: <https://link.aps.org/doi/10.1103/PhysRevE.80.061105>.

BAK, P. *How nature works: the science of self-organized criticality*. [S.l.]: Springer Science & Business Media, 2013.

BAK, P.; TANG, C.; WIESENFELD, K. Self-organized criticality: An explanation of the 1/f noise. *Phys. Rev. Lett.*, v. 59, p. 381–384, 1987. Disponível em: <https://link.aps.org/doi/10.1103/PhysRevLett.59.381>.

BEGGS, J. M. The criticality hypothesis: how local cortical networks might optimize information processing. *Philos. Trans. Royal Soc. A*, v. 366, n. 1864, p. 329–343, 2007.

BEGGS, J. M.; PLENZ, D. Neuronal avalanches in neocortical circuits. *J. Neurosci.*, v. 23, n. 35, p. 11167–11177, 2003.

BENAYOUN, M.; COWAN, J. D.; DRONGELEN, W. van; WALLACE, E. Avalanches in a stochastic model of spiking neurons. *PLOS Computational Biology*, v. 6, n. 7, p. e1000846, 2010. Disponível em: <https://doi.org/10.1371/journal.pcbi.1000846>.

BEURLE, R. L. Properties of a mass of cells capable of regenerating pulses. *Philosophical Transactions of the Royal Society of London. Series B, Biological Sciences*, p. 55–94, 1956.

BINNEY, J.; DOWRICK, N.; FISHER, A.; NEWMAN, M. *The Theory of Critical Phenomena*. Oxford: Oxford University Press, 1993.

BRUNEL, N. Dynamics of sparsely connected networks of excitatory and inhibitory spiking neurons. *J. Comput. Neurosci.*, v. 8, p. 183 – 208, 2000. Disponível em: <https://link.aps.org/doi/10.1103/PhysRevLett.94.145702>.

BRUNEL, N. Dynamics of sparsely connected networks of excitatory and inhibitory spiking neurons. *J. Comput. Neurosci.*, v. 8, n. 3, p. 183–208, 2000.

BUENDíA, V.; VILLEGAS, P.; SANTO, S. di; VEZZANI, A.; BURIONI, R.; MUÑOZ, M. A. Jensen's force and the statistical mechanics of cortical asynchronous states. *Sci. Rep.*, v. 9, n. 1, 2019.

BUICE, M. A.; COWAN, J. D. Field-theoretic approach to fluctuation effects in neural networks. *Phys. Rev. E*, v. 75, p. 051919, 2007. Disponível em: <https://link.aps.org/doi/10.1103/PhysRevE.75.051919>.

CANDIA, A. de; SARRACINO, A.; APICELLA, I.; ARCANGELIS, L. de. Critical behaviour of the stochastic Wilson-Cowan model. *PLoS Comput. Biol.*, v. 17, n. 8, p. 1–23, 2021. Disponível em: <https://doi.org/10.1371/journal.pcbi.1008884>.

CARELLI, F. The book of death: weighing your heart. *London journal of primary care*, v. 4, n. 1, p. 87–88, 2011.

CARVALHO, T. T. A.; FONTENELE, A. J.; GIRARDI-SCHAPPO, M.; FELICIANO, T.; AGUIAR, L. A. A.; SILVA, T. P. L.; VASCONCELOS, N. A. P. de; CARELLI, P. V.; COPELLI, M. Subsampled directed-percolation models explain scaling relations experimentally observed in the brain. *Front. Neural Circuits*, v. 14, 2021. Disponível em: <https://doi.org/10.3389/fncir.2020.576727>.

CASTELLANO, N. The Book of the Dead was Egyptians' inside guide to the underworld. *National Geographic*, 2019. Disponível em: <https://www.nationalgeographic.co.uk/history/2019/02/the-book-of-the-dead-was-egyptians-inside-guide-to-the-underworld>.

CHESSA, A.; STANLEY, H. E.; VESPIGNANI, A.; ZAPPERI, S. Universality in sandpiles. *Phys. Rev. E*, v. 59, n. 1, p. R12, 1999.

CHIALVO, D. R. Emergent complex neural dynamics. *Nat. Phys.*, v. 6, p. 744–750, 2010.

CHIALVO, D. R. Life at the edge: complexity and criticality in biological function. *arXiv preprint arXiv:1810.11737*, 2018.

CHRISTENSEN, K.; FOGEDBY, H. C.; JENSEN, H. J. Dynamical and spatial aspects of sandpile cellular automata. *J. Stat. Phys.*, Springer, v. 63, n. 3, p. 653–684, 1991.

CORTES, J. M.; DESROCHES, M.; RODRIGUES, S.; VELTZ, R.; MUÑOZ, M. A.; SEJNOWSKI, T. J. Short-term synaptic plasticity in the deterministic tsodyks–markram model leads to unpredictable network dynamics. *Proceedings of the National Academy of Sciences*, v. 110, n. 41, p. 16610–16615, 2013.

COTA, W.; FERREIRA, S. C.; ÓDOR, G. Griffiths effects of the susceptible-infected-susceptible epidemic model on random power-law networks. *Phys. Rev. E*, v. 93, p. 032322, 2016. Disponível em: <https://link.aps.org/doi/10.1103/PhysRevE.93.032322>.

COWAN, J. D. Statistical mechanics of nervous nets. In: _____. *Neural Networks: Proceedings of the -School on Neural Networks - June 1967 in Ravello*. Berlin, Heidelberg: Springer Berlin Heidelberg, 1968. p. 181–188. ISBN 978-3-642-87596-0. Disponível em: <https://doi.org/10.1007/978-3-642-87596-0_17>.

COWAN, J. D.; NEUMAN, J.; DRONGELEN, W. van. Wilson–Cowan equations for neocortical dynamics. *JMN*, v. 6, n. 1, p. 1–24, 2016.

DELUCA, A.; CORRAL, Á. Fitting and goodness-of-fit test of non-truncated and truncated power-law distributions. *Acta Geophysica*, v. 61, p. 1351–1394, 2013.

DICKMAN, R.; CAMPELO, J. M. M. Avalanche exponents and corrections to scaling for a stochastic sandpile. *Phys. Rev. E*, v. 67, p. 066111, 2003. Disponível em: <https://link.aps.org/doi/10.1103/PhysRevE.67.066111>.

EFRON, B.; TIBSHIRANI, R. The bootstrap method for assessing statistical accuracy. *Behaviormetrika*, v. 12, n. 17, p. 1–35, 1985.

FERREIRA, S. C.; FERREIRA, R. S.; PASTOR-SATORRAS, R. Quasistationary analysis of the contact process on annealed scale-free networks. *Phys. Rev. E*, American Physical Society, v. 83, p. 066113, Jun 2011. Disponível em: <https://link.aps.org/doi/10.1103/PhysRevE.83.066113>.

FONTENELE, A. J.; VASCONCELOS, N. A. P. de; FELICIANO, T.; AGUIAR, L. A. A.; SOARES-CUNHA, C.; COIMBRA, B.; PORTA, L. D.; RIBEIRO, S.; RODRIGUES, A. J.; SOUSA, N.; CARELLI, P. V.; COPELLI, M. Criticality between cortical states. *Phys. Rev. Lett.*, v. 122, n. 20, p. 208101, 2019.

FRIEDMAN, N.; ITO, S.; BRINKMAN, B. A. W.; SHIMONO, M.; Lee DeVille, R. E.; DAHMEN, K. A.; BEGGS, J. M.; BUTLER, T. C. Universal critical dynamics in high resolution neuronal avalanche data. *Phys. Rev. Lett.*, v. 108, p. 208102, 2012. Disponível em: <https://link.aps.org/doi/10.1103/PhysRevLett.108.208102>.

GARDINER, C. W. *Handbook of stochastic methods for physics, chemistry and the natural sciences*. Third. Berlin: Springer-Verlag, 2004. v. 13. (Springer Series in Synergetics, v. 13). ISBN 3-540-20882-8.

GILLESPIE, D. T. A general method for numerically simulating the stochastic time evolution of coupled chemical reactions. *J. Comput. Phys.*, v. 22, n. 4, p. 403 – 434, 1976. ISSN 0021-9991. Disponível em: <https://doi.org/10.1016/0021-9991(76)90041-3>.

GILLESPIE, D. T. Exact stochastic simulation of coupled chemical reactions. *J. Phys. Chem.*, v. 81, n. 25, p. 2340–2361, 1977. Disponível em: <https://doi.org/10.1021/j100540a008>.

GIRARDI-SCHAPPO, M.; BROCHINI, L.; COSTA, A. A.; CARVALHO, T. T. A.; KINOUCHI, O. Synaptic balance due to homeostatically self-organized quasicritical dynamics. *Physical Review Research*, v. 2, n. 1, p. 012042(R), 2020.

GIRARDI-SCHAPPO, M.; GALERA, E. F.; CARVALHO, T. T.; BROCHINI, L.; KAMIJI, N. L.; ROQUE, A. C.; KINOUCHI, O. A unified theory of E/I synaptic balance, quasicritical neuronal avalanches and asynchronous irregular spiking. *J. Phys. Complex.*, v. 2, n. 4, p. 045001, 2021.

GIREESH, E. D.; PLENZ, D. Neuronal avalanches organize as nested theta- and beta/gamma-oscillations during development of cortical layer 2/3. *Proceedings of the National Academy of Sciences*, v. 105, n. 21, p. 7576–7581, 2008. Disponível em: <https://www.pnas.org/doi/abs/10.1073/pnas.0800537105>.

GLENDINNING, P.; JEFFREY, M. R. *An Introduction to Piecewise Smooth Dynamics*. 1. ed. [S.l.]: Birkhüser, Cham, 2019. ISBN 978-3-030-23688-5.

GLICKSTEIN, M. *Neuroscience: A historical introduction*. [S.l.]: MIT Press, 2017.

GRASSBERGER, P. On phase transitions in Schlögl's second model. In: *Nonlinear Phenomena in Chemical Dynamics*. [S.l.]: Springer, 1981. p. 262–262.

GRINSTEIN, G.; LAI, Z.-W.; BROWNE, D. A. Critical phenomena in a nonequilibrium model of heterogeneous catalysis. *Phys. Rev. A*, v. 40, n. 8, p. 4820, 1989.

GRINSTEIN, G.; LAI, Z.-W.; BROWNE, D. A. Critical phenomena in a nonequilibrium model of heterogeneous catalysis. *Phys. Rev. A*, v. 40, p. 4820–4823, 1989. Disponível em: <https://link.aps.org/doi/10.1103/PhysRevA.40.4820>.

GRINSTEIN, G.; MUÑOZ, M. The statistical mechanics of systems with absorbing states, in "Fourth Granada Lectures in Computational Physics", ed. by P. Garrido and J. Marro. *Lecture Notes in Physics*, v. 493, p. 223, 1996.

GROSS, C. G. *Brain, vision, memory: Tales in the history of neuroscience*. [S.l.]: MIT Press, 1999.

GUDOWSKA-NOWAK, E.; NOWAK, M. A.; CHIALVO, D. R.; OCHAB, J. K.; TARNOWSKI, W. From synaptic interactions to collective dynamics in random neuronal networks models: critical role of eigenvectors and transient behavior. *Neural Computation*, v. 32, n. 2, p. 395–423, 2020.

HARRIS, J.; ERMENTROUT, B. Bifurcations in the Wilson–Cowan equations with nonsmooth firing rate. *SIAM J. Appl. Dyn. Syst.*, v. 14, n. 1, p. 43–72, 2015. Disponível em: <https://doi.org/10.1137/140977953>.

HARRIS, T. E. *The theory of branching processes*. [S.l.]: Courier Corporation, 2002.

HENKEL, M.; HINRICHSEN, H.; LÜBECK, S. *Non-equilibrium Phase Transitions: Absorbing phase transitions*. Berlin: Springer London, 2008. (Theor. and Math. Phys.).

HIDALGO, J.; SEOANE, L.; CORTÉS, J.; MUÑOZ, M. Stochastic amplification of fluctuations in cortical upstates. *PLoS One*, v. 7(8), p. e40710, 2012.

HINRICHSEN, H. Non-equilibrium critical phenomena and phase transitions into absorbing states. *Adv. Phys.*, v. 49, p. 815–958, 2000.

HOOPEN, M. T. Probabilistic firing of neurons considered as a first passage problem. *Biophysical Journal*, v. 6, n. 4, p. 435–451, 1966.

HOPPENSTEADT, F. C.; IZHIKEVICH, E. M. *Weakly connected neural networks*. [S.l.]: Springer, 1997. v. 126.

IZHIKEVICH, E. M. *Dynamical systems in neuroscience*. [S.l.]: MIT press, 2007.

JANSSEN, H.-K. On the nonequilibrium phase transition in reaction-diffusion systems with an absorbing stationary state. *Z. Phys. B Condensed Matter*, v. 42, n. 2, p. 151–154, 1981.

KAMPEN, N. V. *Stochastic processes in physics and chemistry*. [S.l.]: North Holland, 2007.

KINOUCHI, O.; COPELLI, M. Optimal dynamical range of excitable networks at criticality. *Nat. Phys.*, v. 2, n. 5, p. 348–351, 2006. ISSN 1745-2481.

KUNTZ, M. C.; SETHNA, J. P. Noise in disordered systems: The power spectrum and dynamic exponents in avalanche models. *Phys. Rev. B*, v. 62, p. 11699–11708, 2000. Disponível em: <https://link.aps.org/doi/10.1103/PhysRevB.62.11699>.

LAI, L.; ZHU, Z.; CHEN, F. Stability and bifurcation in a predator–prey model with the additive Allee effect and the fear effect. *Mathematics*, v. 8, n. 8, 2020. ISSN 2227-7390. Disponível em: <https://doi.org/10.3390/math8081280>.

LAURSON, L.; ILLA, X.; SANTUCCI, S.; TALLAKSTAD, K. T.; MÅLØY, K. J.; ALAVA, M. J. Evolution of the average avalanche shape with the universality class. *Nat. Commun*, v. 4, n. 1, p. 1–6, 2013.

LIGGETT, T. *Interacting Particle Systems*. Springer, 2004. (Classics in Mathematics). ISBN 9783540226178. Disponível em: <http://books.google.it/books?id=I3aNPR1FursC>.

LÓPEZ, R. C.; BUENDÍA, V.; MUÑOZ, M. A. Excitatory-inhibitory branching process: A parsimonious view of cortical asynchronous states, excitability, and criticality. *Phys. Rev. Research*, v. 4, p. L042027, 2022. Disponível em: <https://link.aps.org/doi/10.1103/PhysRevResearch.4.L042027>.

LOTFI, N.; FELICIANO, T.; AGUIAR, L. A. A.; SILVA, T. P. L.; CARVALHO, T. T. A.; ROSSO, O. A.; COPELLI, M.; MATIAS, F. S.; CARELLI, P. V. Statistical complexity is maximized close to criticality in cortical dynamics. *Phys. Rev. E*, v. 103, p. 012415, 2021. Disponível em: <https://link.aps.org/doi/10.1103/PhysRevE.103.012415>.

LÜBECK, S. Tricritical directed percolation. *J. Stat. Phys.*, v. 123, p. 193–221, 2006.

MARRO, J.; DICKMAN, R. *Nonequilibrium Phase Transition in Lattice Models*. [S.l.]: Cambridge University Press, 1999.

MARRO, J.; DICKMAN, R. *Nonequilibrium Phase Transitions in Lattice Models*. [S.l.]: Cambridge University Press, 1999. (Collection Alea-Saclay: Monographs and Texts in Statistical Physics).

MARSHALL, N.; TIMME, N. M.; BENNETT, N.; RIPP, M.; LAUTZENHISER, E.; BEGGS, J. M. Analysis of power laws, shape collapses, and neural complexity: New techniques and MATLAB support via the NCC toolbox. *Front. Physiol.*, v. 7, 2016. ISSN 1664-042X. Disponível em: <https://www.frontiersin.org/article/10.3389/fphys.2016.00250>.

MARTINELLO, M.; HIDALGO, J.; MARITAN, A.; SANTO, S. di; PLENZ, D.; MUÑOZ, M. A. Neutral theory and scale-free neural dynamics. *Phys. Rev. X*, v. 7, n. 4, p. 041071, 2017.

MARUYAMA, Y.; KAKIMOTO, Y.; ARAKI, O. Analysis of chaotic oscillations induced in two coupled Wilson–Cowan models. *Biol. Cybern.*, v. 108, p. 355–363, 2014. Disponível em: <https://doi.org/10.1007/s00422-014-0604-8>.

MCCULLOCH, W. S.; PITTS, W. A logical calculus of the ideas immanent in nervous activity. *The bulletin of mathematical biophysics*, v. 5, p. 115–133, 1943. Disponível em: <https://doi.org/10.1007/BF02478259>.

MILLER, S. R.; YU, S.; PLENZ, D. The scale-invariant, temporal profile of neuronal avalanches in relation to cortical γ–oscillations. *Sci. Rep.*, v. 9, n. 16403, p. 16403, 2019.

MILLMAN, D.; MIHALAS, S.; KIRKWOOD, A.; NIEBUR, E. Self-organized criticality occurs in non-conservative neuronal networks during 'up' states. *Nat. Phys.*, v. 6, n. 10, p. 801–805, 2010.

MORA, T.; BIALEK, W. Are biological systems poised at criticality? *J. Stat. Phys.*, v. 144, n. 2, p. 268–302, 2011.

MORETTI, P.; MUÑOZ, M. A. Griffiths phases and the stretching of criticality in brain networks. *Nature Comm.*, v. 4, n. 1, p. 1–10, 2013.

MUÑOZ, M. A. Colloquium: Criticality and dynamical scaling in living systems. *Rev. Mod. Phys.*, v. 90, n. 3, p. 031001, jul. 2018.

MUÑOZ, M. A.; DICKMAN, R.; VESPIGNANI, A.; ZAPPERI, S. Avalanche and spreading exponents in systems with absorbing states. *Phys. Rev. E*, v. 59, p. 6175–6179, 1999. Disponível em: <https://link.aps.org/doi/10.1103/PhysRevE.59.6175>.

MUÑOZ, M. A.; GRINSTEIN, G.; TU, Y. Survival probability and field theory in systems with absorbing states. *Phys. Rev. E*, v. 56, p. 5101–5105, 1997. Disponível em: <https://link.aps.org/doi/10.1103/PhysRevE.56.5101>.

MUÑOZ, M. A.; JUHÁSZ, R.; CASTELLANO, C.; ÓDOR, G. Griffiths phases on complex networks. *Physical Review Letters*, v. 105, n. 12, p. 128701, 2010.

NANDI, M. K.; SARRACINO, A.; HERRMANN, H. J.; ARCANGELIS, L. de. Scaling of avalanche shape and activity power spectrum in neuronal networks. *Physical Review E*, APS, v. 106, n. 2, p. 024304, 2022.

NOH, J. D.; PARK, H. Asymmetrically coupled directed percolation systems. *Phys. Rev. Lett.*, v. 94, n. 14, p. 145702, 2005.

NOH, J. D.; PARK, H. Asymmetrically coupled directed percolation systems. *Phys. Rev. Lett.*, v. 94, p. 145702, 2005. Disponível em: <https://link.aps.org/doi/10.1103/PhysRevLett.94.145702>.

ÓDOR, G. *Universality in Nonequilibrium Lattice Systems: Theoretical Foundations*. Singapore: [s.n.], 2008.

ODOR, G. Critical dynamics on a large human open connectome network. *Physical Review E*, v. 94, n. 6, p. 062411, 2016.

OHIRA, T.; COWAN, J. D. Stochastic neurodynamics and the system size expansion. In: *Mathematics of neural networks*. [S.l.]: Springer, 1997. p. 290–294.

OHTSUKI, T.; KEYES, T. Nonequilibrium critical phenomena in one-component reaction-diffusion systems. *Phys. Rev. A*, v. 35, n. 6, p. 2697, 1987.

OLAMI, Z.; FEDER, H. J. S.; CHRISTENSEN, K. Self-organized criticality in a continuous, nonconservative cellular automaton modeling earthquakes. *Phys. Rev. Lett.*, v. 68, p. 1244–1247, 1992. Disponível em: <https://link.aps.org/doi/10.1103/PhysRevLett.68.1244>.

O'BYRNE, J.; JERBI, K. How critical is brain criticality? *Trends in Neurosciences*, 2022.

PAPANIKOLAOU, S.; BOHN, F.; SOMMER, R. L.; DURIN, G.; ZAPPERI, S.; SETHNA, J. P. Universality beyond power laws and the average avalanche shape. *Nat Phys*, v. 7, n. 4, p. 316–320, 2011.

PETERMANN, T.; THIAGARAJAN, T. C.; LEBEDEV, M. A.; NICOLELIS, M. A. L.; CHIALVO, D. R.; PLENZ, D. Spontaneous cortical activity in awake monkeys composed of neuronal avalanches. *Proceedings of the National Academy of Sciences*, v. 106, n. 37, p. 15921–15926, 2009. Disponível em: <https://www.pnas.org/doi/abs/10.1073/pnas.0904089106>.

PINTO, I. L. D.; COPELLI, M. Oscillations and collective excitability in a model of stochastic neurons under excitatory and inhibitory coupling. *Phys. Rev. E*, v. 100, p. 062416, 2019. Disponível em: <https://link.aps.org/doi/10.1103/PhysRevE.100.062416>.

PIUVEZAM, H. C.; MARIN, B.; COPELLI, M.; MUÑOZ, M. A. Unconventional criticality, scaling breakdown, and diverse universality classes in the wilson-cowan model of neural dynamics. *Phys. Rev. E*, v. 108, p. 034110, 2023. Disponível em: <https://link.aps.org/doi/10.1103/PhysRevE.108.034110>.

PLENZ, D.; RIBEIRO, T. L.; MILLER, S. R.; KELLS, P. A.; VAKILI, A.; CAPEK, E. L. Self-organized criticality in the brain. *Frontiers in Physics*, v. 9, p. 639389, 2021.

PONCE-ALVAREZ, A.; JOUARY, A.; PRIVAT, M.; DECO, G.; SUMBRE, G. Whole-brain neuronal activity displays crackling noise dynamics. *Neuron*, v. 100, n. 6, p. 1446–1459, 2018.

PONCE-ALVAREZ, A.; JOUARY, A.; PRIVAT, M.; DECO, G.; SUMBRE, G. Whole-brain neuronal activity displays crackling noise dynamics. *Neuron*, v. 100, n. 6, p. 1446–1459, 2018.

RIBEIRO, T. L.; RIBEIRO, S.; COPELLI, M. Repertoires of spike avalanches are modulated by behavior and novelty. *Frontiers in Neural Circuits*, v. 10, 2016. ISSN 1662-5110. Disponível em: <https://www.frontiersin.org/articles/10.3389/fncir.2016.00016>.

SANTO, S. di; VILLEGAS, P.; BURIONI, R.; MUÑOZ, M. A. Non-normality, reactivity, and intrinsic stochasticity in neural dynamics: a non-equilibrium potential approach. *JSTAT*, v. 2018, n. 7, p. 073402, 2018.

SETHNA, J. P.; DAHMEN, K. A.; MYERS, C. R. Crackling noise. *Nature*, v. 410, p. 242–250, 2001. Disponível em: <https://doi.org/10.1038/35065675>.

TOUBOUL, J.; DESTEXHE, A. Power-law statistics and universal scaling in the absence of criticality. *Phys. Rev. E*, v. 95, p. 012413, 2017. Disponível em: <https://link.aps.org/doi/10.1103/PhysRevE.95.012413>.

VEEN, L. van; HOTI, M. Automatic detection of saddle-node–transcritical interactions. *IJBC*, v. 29, n. 08, p. 1950104, 2019. Disponível em: <https://doi.org/10.1142/S0218127419501049>.

WALLACE, E.; BENAYOUN, M.; DRONGELEN, W. van; COWAN, J. D. Emergent oscillations in networks of stochastic spiking neurons. *PLoS ONE*, v. 6, n. 5, p. 1–16, 2011. Disponível em: <https://doi.org/10.1371/journal.pone.0014804>.

WILSON, H. R.; COWAN, J. D. Excitatory and inhibitory interactions in localized populations of model neurons. *Biophys. J.*, v. 12, p. 1–23, 1972.

WILSON, H. R.; COWAN, J. D. A mathematical theory of the functional dynamics of cortical and thalamic nervous tissue. *Kybernetik*, v. 13, n. 2, p. 55–80, 1973.

APPENDIX A – NUMERICAL METHODS

A.1 MAXIMUM LIKELIHOOD ESTIMATOR

The distributions of size and duration undergo a power-law fit with the maximum likelihood estimator (MLE) algorithm yielding the exponents.

The discrete distribution follows

$$f(x) = A(\alpha; x_{min}, x_{max})x^{-\alpha}\,, \tag{A.1}$$

where $A(\alpha; x_{min}, x_{max})$ is the normalization constant.

$$A(\alpha; x_{min}, x_{max}) = \left(\sum_{x=x_{min}}^{x_{max}} x^{-\alpha}\right)^{-1} \tag{A.2}$$

The likelihood function is

$$L(\alpha) = \prod_{i=0}^{N-1} f(x_i). \tag{A.3}$$

The logarithm of Eq (A.3) is more easily treatable, so the log-likelihood is:

$$l(\alpha) = \frac{1}{N}\log\left(A(\alpha; x_{min}, x_{max})^N \prod_{i=0}^{N-1} x_i\right) \tag{A.4}$$

$$= -\log\left(\sum_{x=x_{min}}^{x_{max}} x^{-\alpha}\right) - \frac{\alpha}{N}\sum_{i=0}^{N-1}\log(x_i). \tag{A.5}$$

Considering that the left side of this equation grows and the right side decays continuously with α, there should be a value of α that maximizes this log-likelihood. Using the lattice search algorithm, the exponent value is $\hat{\alpha} = \arg\max_\alpha l(\alpha)$ (MARSHALL et al., 2016).

A.2 BOOTSTRAP

The error in the simulation analysis was calculated through bootstrapping. Bootstrap is a resampling method, where we sample with replacement from the original data; therefore, the new samples are made without assumptions about the underlying distribution of the data. The script follows:

Step 1 Create multiple resampling datasets of the same size by randomly selecting data points with replacements.

Step 2 Run the MLE algorithm for each new sample.

Step 3 and, take the standard deviation of these values.

The Bootstrap method is widely used in scientific research to assess the stability of statistical estimates (EFRON; TIBSHIRANI, 1985).

APPENDIX B – SIMULATION METHOD: GILLESPIE'S ALGORITHM

The majority of the results in this paper are analytical. However, the survival probability and avalanche analysis are purely stochastic phenomena. As such, the stochastic Markov version of the Wilson-Cowan model was simulated using Gillespie's algorithm (GILLESPIE, 1976; GILLESPIE, 1977). The algorithm follows the steps:

Step 0 Initialize the system. For the survival and for avalanche analysis, only an excitatory site is active at $t = 0$;

Step 1 at each time step, calculate the transition rates for each neuron – if active, $\Phi(s_i)$, and otherwise, α – and sum these rates, r;

Step 2 the time step is chosen from an exponential distribution with rate r and added to the total time;

Step 3 and, the site to be updated is chosen with probability r_i/r.

The size and duration of the avalanche are counted as the number of spikes and duration of a single instance of the simulation from one excitatory site activated to all sites being inactivated. The advantage of this method is that it is independent of bin size.

APPENDIX C – PIECEWISE SMOOTH DYNAMICAL SYSTEM CALCULATIONS

C.1 DISCONTINUITY-INDUCED BIFURCATION

A “discontinuity-induced bifurcation" is a direct consequence of the non-smooth dynamics of the system (HARRIS; ERMENTROUT, 2015). These bifurcations happen because of the presence of switching manifolds, observe that as we transition from one panel to the other from (a) to (d) in Fig. 42 shows us the area in the phase diagrams where the initial conditions are attracted to the regions inside the switching manifolds, i.e., the basin of attraction of said regions. For the purposes of the transitions mentioned throughout this thesis, we searched for the limits of the global stability of the quiescent state when the initial conditions are excitatory-dominated.

Figure 42 – Basin of attraction of the regions enclosed by the switching manifolds across the T_4 transition. Parameters: $\alpha = 1$, $w_{II} = 0$, $w_{EI} = 3$, $w_{IE} = 0.5$, and $w_{EE} = [1.5, 2.0, 2.5, 3.0]$

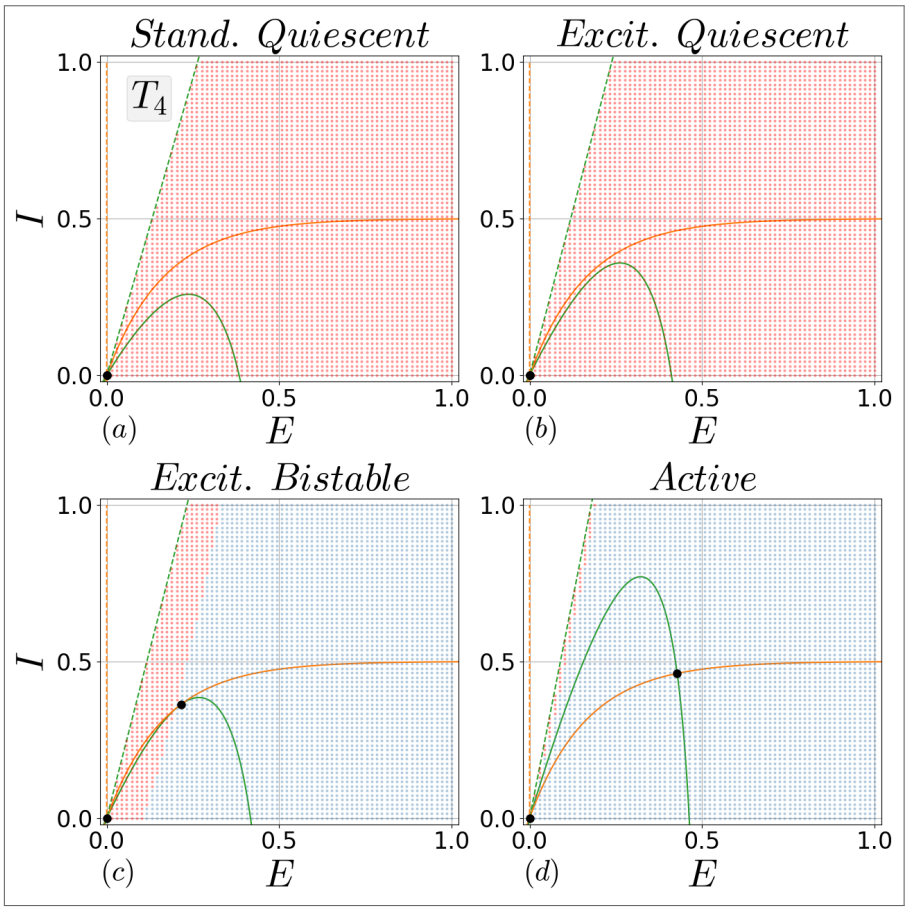

Source: The author (2023)

For T_4, the system has a period without a locally stable solution in region I; the quiescent state, however, attracts the trajectories through the other regions constituting a globally stable fixed point. As the control parameter increases, the basin of attraction of the regions diminishes up to the discontinuity-induced bifurcation, where the only available stable fixed point is the active one. For T_6, T_7, and T_8, the transition is continuous. Close to the point where the active stable fixed point appears, the basin reduces to nothing and the system relaxes to an active state.

C.2 BEHAVIOR ON THE SWITCHING MANIFOLDS

Piece-wise continuous dynamics have two possible behaviors at the switching manifolds: sliding or crossing (GLENDINNING; JEFFREY, 2019). This behavior depends on the system's flow on each side of the switching manifold. If we consider the Heaviside function, Eq. (3.12), in Eqs. (3.23) and (3.24):

$$\dot{x} = \begin{cases} f_x^+ \equiv -\alpha x + (1-x)\tanh(w_i x - w_j y) \ , \\ \qquad\qquad \text{if } s \equiv w_i x - w_j y > 0 \\ f_x^- \equiv -\alpha x \ , \ \text{if } s < 0 \end{cases} \tag{C.1}$$

where f_x^+ is the dynamics to the right and f_x^- is to the left of the switching manifold, $s = 0$.

Let's consider the switching manifold $s_E = 0$, where $E = (w_{EI}/w_{EE})I$. We can then write:

$$\vec{\nabla} s_E = \begin{pmatrix} \frac{\partial}{\partial E} s_E \\ \frac{\partial}{\partial I} s_E \end{pmatrix} = \begin{pmatrix} W_{EE} \\ -W_{EI} \end{pmatrix} \tag{C.2}$$

$$\vec{f}^{+} = \begin{pmatrix} -\alpha E + (1-E)\tanh\left(w_{EE}E - w_{EI}I\right) \\ -\alpha I + (1-I)\tanh\left(w_{IE}E - w_{II}I\right) \end{pmatrix}^T \tag{C.3}$$

$$\vec{f}^{-} = \begin{pmatrix} -\alpha E \\ -\alpha I + (1-I)\tanh\left(w_{IE}E - w_{II}I\right) \end{pmatrix}^T . \tag{C.4}$$

We want to evaluate the sign of $(\vec{f}^{+} \cdot \vec{\nabla} s_E)(\vec{f}^{-} \cdot \vec{\nabla} s_E)$ at the switching manifold, to know

if, as our system reaches the s_E, the trajectories will cross or slide on it.

$$\begin{aligned}\vec{f}^{+}\cdot\vec{\nabla}s_E &= -\alpha(w_{EE}E - w_{EI}I) + w_{EE}(1-E)\tanh\left(w_{EE}E - w_{EI}I\right) + \\ &\quad -w_{EI}(1-I)\tanh\left(w_{IE}E - w_{II}I\right), \qquad \text{(C.5)}\\ \vec{f}^{-}\cdot\vec{\nabla}s_E &= -\alpha(w_{EE}E - w_{EI}I) - w_{EI}(1-I)\tanh\left(w_{IE}E - w_{II}I\right) \qquad \text{(C.6)}\end{aligned}$$

At the switching manifold, $w_{EE}E = w_{EI}I$:

$$\begin{aligned}\vec{f}^{+}\cdot\vec{\nabla}s_E &= -w_{EI}(1-I)\tanh\left(\frac{w_{IE}(w_{EI}-w_{II})}{w_{EE}}I\right), \qquad \text{(C.7)}\\ \vec{f}^{-}\cdot\vec{\nabla}s_E &= -w_{EI}(1-I)\tanh\left(\frac{w_{IE}(w_{EI}-w_{II})}{W_{EE}}I\right), \qquad \text{(C.8)}\\ (\vec{f}^{+}\cdot\vec{\nabla}s_E)(\vec{f}^{-}\cdot\vec{\nabla}s_E) &= \left[w_{EI}(1-I)\tanh\left(\frac{w_{IE}(w_{EI}-w_{II})}{w_{EE}}I\right)\right]^2. \qquad \text{(C.9)}\end{aligned}$$

For $(\vec{f}^{+}\cdot\vec{\nabla}s_E)(\vec{f}^{-}\cdot\vec{\nabla}s_E) > 0$, the trajectories cross the switching manifold creating a trapping region.

Now we consider the second switching manifold, $s_I = 0$, where $E = (w_{II}/w_{IE})I$. Following

Figure 43 – Decelerating decay onto the switching manifolds. Close to the switching manifold, the trajectories reach the quiescent state along the switching manifold in a decelerating decay. The fixed parameters: $\alpha = 1.0$ and $w_{EI} = 1.5$. (a) $w_{EE} = 2.7$, $w_{IE} = 1.0$, and $w_{II} = 0.5$. (b) $w_{EE} = 2.0$, $w_{IE} = 2.0$, and $w_{II} = 1.0$. Observe that five different initial conditions are producing the magenta dashed lines.

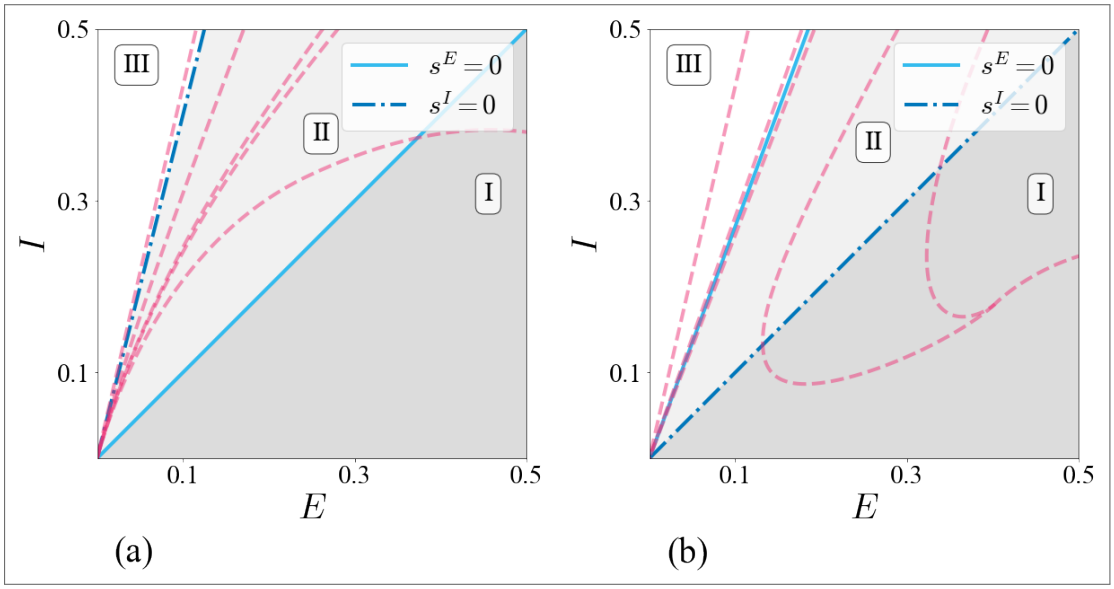

Source: The author (2023)

the script above:

$$\vec{\nabla} s_I = \begin{pmatrix} \frac{\partial}{\partial E} s_I \\ \frac{\partial}{\partial I} s_I \end{pmatrix} = \begin{pmatrix} W_{IE} \\ -W_{II} \end{pmatrix} \tag{C.10}$$

$$\vec{f^+} = \begin{pmatrix} -\alpha E \\ -\alpha I + (1-I)\tanh\left(w_{IE}E - w_{II}I\right) \end{pmatrix}^T \tag{C.11}$$

$$\vec{f^-} = \begin{pmatrix} -\alpha E \\ -\alpha I \end{pmatrix}^T . \tag{C.12}$$

Evaluating the sign of $(\vec{f^+} \cdot \vec{\nabla} s_I)(\vec{f^-} \cdot \vec{\nabla} s_I)$,

$$\vec{f^+} \cdot \vec{\nabla} s_I = -\alpha(w_{IE}E - w_{II}I) - w_{II}(1-I)\tanh\left(w_{IE}E - w_{II}I\right) \tag{C.13}$$

$$\vec{f^-} \cdot \vec{\nabla} s_I = -\alpha(w_{IE}E - w_{III}I), \tag{C.14}$$

at the switching manifold, $w_{IE}E = w_{II}I$, then

$$\vec{f^+} \cdot \vec{\nabla} s_I = 0, \tag{C.15}$$

$$\vec{f^-} \cdot \vec{\nabla} s_E = 0, \tag{C.16}$$

$$(\vec{f^+} \cdot \vec{\nabla} s_E)(\vec{f^-} \cdot \vec{\nabla} s_E) = 0. \tag{C.17}$$

The theory only accounts for either $(\vec{f^+} \cdot \vec{\nabla} s_E)(\vec{f^-} \cdot \vec{\nabla} s_E) \gtrless 0$. The null result yields more questions than answers. However, when simulated, we observe the trajectories slowly decelerate as they reach the switching manifolds (see Fig. 43).